論文 / 著書情報
Article / Book Information

題目(和文)	
Title(English)	Study of Bidirectional Chopper with Single Full-Bridge Auxiliary Converter for Onboard Battery Energy Storage Systems
著者(和文)	NASUTION GHIFFARI ABY MALIK
Author(English)	Ghiffari Aby Malik Nasution
出典(和文)	学位:博士(工学), 学位授与機関:東京科学大学, 報告番号:甲第349号, 授与年月日:2025年3月26日, 学位の種別:課程博士, 審査員:萩原 誠,藤田 英明,竹内 希,清田 恭平,佐野 憲一朗,小原 秀嶺
Citation(English)	Degree:Doctor (Engineering), Conferring organization: Institute of Science Tokyo, Report number:甲第349号, Conferred date:2025/3/26, Degree Type:Course doctor, Examiner:,,,,,
学位種別(和文)	博士論文
Type(English)	Doctoral Thesis

東京科学大学
Institute of Science Tokyo

工学院
School of Engineering

電気電子系
Department of Electrical and Electronic Engineering

Study of Bidirectional Chopper with Single Full-Bridge Auxiliary Converter for Onboard Battery Energy Storage Systems

Author
Ghiffari Aby Malik Nasution

Supervisor
Makoto Hagiwara

February 17, 2025

Dedication

This work is dedicated to my family and people who have supported me throughout my life. Special mention to my late-grandpa, who despite my continual refusal, kept insisting for me to take PhD. May this work stand as a testament to my effort in contributing to the well-being and sustainability of the society, and I hope that all of you are proud of it.

Examining Committee

This dissertation is submitted by Ghiffari Aby Malik Nasution in partial fulfillment of the requirements for the acquirement of the Doctor of Engineering degree in Energy Science and Engineering.

Chief Examiner:

Assoc. Prof. Makoto Hagiwara, Institute of Science Tokyo, Department of Electrical and Electronic Engineering.

Examiners:

Prof. Hideaki Fujita, Institute of Science Tokyo, Department of Electrical and Electronic Engineering.

Assoc. Prof. Nozomi Takeuchi, Institute of Science Tokyo, Department of Electrical and Electronic Engineering.

Assoc. Prof. Kyohei Kiyota, Institute of Science Tokyo, Department of Electrical and Electronic Engineering.

Assist. Prof. Kenichiro Sano, Institute of Science Tokyo, Department of Electrical and Electronic Engineering.

External Examiner:

Assoc. Prof. Hidemine Obara, Yokohama National University, Department of Mathematics, Physics, Electrical Engineering and Computer Science.

Abstract

This dissertation proposes a bidirectional chopper with a single full-bridge auxiliary converter (BCSAC) for the utilization of battery energy storage system (BESS) in electric vehicles (EVs). The BCSAC is a particular case of the bidirectional chopper with an auxiliary converter (BCAC), composing of a bidirectional chopper as the main converter, an auxiliary converter made of single-phase full-bridge cells connected in cascade, and an inductor. By functioning the auxiliary converter as an active power filter, the BCAC allows the reduction of the switching-ripple current of the inductor, which consequently reduces the inductance value of the inductor and its associated volume. Meanwhile, the application of a single auxiliary converter of the BCSAC aims to mitigate the significant power loss and cost issues that comes with the usage of an auxiliary converter with multiple cells in the BCAC. To evaluate the performance of the proposed BCSAC and its efficacy, theoretical analysis is conducted on the switching-ripple current, while theoretical comparison with other topologies is carried out on the inductor volume, chopper volume and mass, power loss, and efficiency. The theoretical analysis results, focusing on the switching-ripple current, are validated through experiments using a 2 kW down-scaled model, and the chopper operations under steady and transient states are verified. Additionally, the application of phase shift to the carrier waveforms of the main and auxiliary converters in the BCSAC is proposed to further reduce the produced switching-ripple current. The significance of the BCSAC with phase shift (BCSAC-PS) is evaluated through theoretical analysis and comparison with other topologies on the inductor volume, chopper volume and mass, power loss, and efficiency, while experiment using the down-scaled model confirms the theoretical results of the switching-ripple current. Finally, a supplementary application of AC component-based control is proposed in the BCSAC-PS to allow the achievement of the DC-capacitor voltage control when there is no power transfer between the voltage sources. Consequently, the stability of the chopper operation would be improved. The operations of

the proposed AC component-based control in the BCSAC-PS during steady and transient states, along with its coordinated operation with the conventional DC component-based control, are verified through experiments using the down-scaled model.

Acknowledgments

Getting a PhD is a journey without assurance of completion. I was lucky enough to receive a great deal of support and assistance throughout mine, of which without I would not have even seen the finish line.

First and foremost, I would like to praise the God Almighty, for without His blessings and gifts of faith, knowledge, and perseverance, I would not have been able to finish this journey.

Associate Professor Makoto Hagiwara (萩原　誠), my supervisor for this journey. Thank you for accepting me, and having faith in me, as a PhD student in your lab, even when I was not confident in myself. I did not come from electrical background, so I had to learn everything almost from the beginning. Your patience and support have made this journey feel easier than it should have been. I always think that I should have joined your lab earlier.

Professor Hideaki Fujita (藤田　英明) and Assistant Professor Kenichiro Sano (佐野　憲一朗), whose comments and feedbacks during the lab seminars help me to gain deeper understanding on my own research. Thank you for your insights and advice throughout this journey.

My labmates, who are all smart, active, critical, supportive, and hard-working people. Thanks to all of you being so productive, I have always felt driven and fired up, since I am a competitive person. I would like to give special mention to Mr. Hamdan Nour A. K., Dr. Nikola Krneta, Mr. Masaki Matsumoto, Mr. Luo Tian, Mr. Zhang Zheng, Dr. Yu-Chen Su, Mr. Wei Lijun, Mr. Kyogo Umano, Mr. Atsuya Suzuki, Mr. Tatsuya Yamada, Mr. Taiki Kanda, Mr. Mitsuyoshi Enomoto, Mr. Yamato Kamiyama, and Ms. Maira Izammel binti Zainoren, for the interactions we had throughout my journey. The jokes and warm conversations are much-needed breaks in between the research work.

My family, Mr. Asjrin Nasution (father), Mrs. Dien Novita (mother), and Mr.

Muhammad Hanif A. Nasution (brother), whose unending support, encouragement, advice, and assurance give me the strength and tenacity to finish this journey. I would like to give special appreciation to Ms. Luthfia Shofi Albi, my wife, for all of her support, including all of the tangible and intangible things. Thank you for being there, and letting me keep my sanity throughout this journey. Finally, I would like to thank Mr. Ahmad Zavian A. Nasution, my son, whose birth gave the extra motivation and energy to finish this journey on time.

The scholarship providers, JEES 三井不動産 and 綿貫国際奨学財団, whose financial support allow me to focus on my research and finish this journey on time.

Contents

List of Figures

List of Tables

List of Abbreviations

AC	alternating current vii, viii, xiii, xvii, 4, 8, 10, 15, 22, 23, 28, 31, 54, 55, 58, 61, 63, 65, 69, 85, 86, 88–94, 96–101, 104
BCAC	bidirectional chopper with an auxiliary converter vii, xv, xix, 11, 15–17, 19, 21, 23, 24, 42–44, 46–49, 58, 103, 116
BCSAC	bidirectional chopper with a single full-bridge auxiliary converter vii, xv–xvii, xix, 8–10, 19–24, 26–30, 35, 36, 41–44, 46–59, 61, 62, 71, 73, 74, 76–79, 81–83, 103–105, 107–110, 113, 116
BCSAC-PS	BCSAC with phase shift vii, viii, xvi, xvii, xix, 59–64, 67, 68, 71, 73, 74, 76–83, 85, 86, 92–101, 104, 113, 116
BESS	battery energy storage system vii, xv, 1, 5–7, 11, 12, 103
CBC	conventional bidirectional chopper xv–xvii, xix, 1, 11–17, 20, 41–44, 46–49, 51–54, 58, 71, 73, 74, 76–83, 85, 94, 103, 104, 108–110, 113, 116
CHBC	cascaded h-bridge chopper 11, 13
CSPI	cooling system performance index 44, 72, 76, 114
DC	direct current vii, viii, xiii, xvi, xvii, 4, 8, 10, 12, 14–16, 20–28, 30, 44, 46, 47, 50, 52, 54–58, 60–63, 65, 72, 77, 80, 81, 85–90, 92–97, 99–101, 103, 104, 107

DSP	digital signal processor 51, 81
ESS	energy storage system 11, 13
EV	electric vehicle vii, 1–7, 9, 11, 13
FCC	flying capacitor chopper 11, 13, 14, 16, 17
FESS	flywheel energy storage system xv, 5, 6
FPGA	field-programmable gate array 51, 81
FWD	free-wheeling diode 46, 73, 113–116
GHG	greenhouse gas 1, 2
ICE	internal combustion engine 2, 4
IEA	international energy agency 1
IGBT	insulated-gate bipolar transistor 46, 73, 113–116
KVL	kirchhoff's voltage law 32, 34, 39, 40, 66, 70
Li-ion	lithium-ion 6
LVDC	low-voltage direct current 4
MMC	modular multilevel chopper 11, 13
MVDC	medium-voltage direct current 4
NiMH	nickel-metal hydride 6
NPCC	neutral point clamped chopper 11
OESS	onboard energy storage system xi, 4, 5, 9
Pb-Acid	lead-acid 6
PI	proportional-integral 25, 26, 57, 87–90, 92, 96, 99
PWM	pulse-width modulation 12, 21, 27, 85, 88, 92
SESS	supercapacitor energy storage system xv, 5, 6
Si-IGBT	silicon-insulated gate bipolar transistors 7, 46, 73, 116
SiC-MOSFET	silicon carbide-metal oxide semiconductor field effect transistor 7
TLFC	three-level flying capacitor converter xv, xix, 13, 14, 42–44, 46–49, 58, 103, 104, 113, 116
TLFC-PS	TLFC with phase shift xvi, xix, 71, 74, 76–79, 83, 104, 113, 114, 116

TTW tank-to-wheel 2

WTT well-to-tank 3

WTW well-to-wheel xv, 3, 4

Chapter 1

Introduction

The purpose of this dissertation is to propose a non-isolated bidirectional chopper that supports the implementation of onboard battery energy storage system in electric vehicles. electric vehicles play a pivotal role in reducing global GHG (greenhouse gas) emissions, particularly in the transportation sector, and their operation requires the application of onboard battery energy storage system to store and release the regenerative-braking energy and allow independence from continuous external power sources. Considering the additional component, mass and volume reductions of the bidirectional chopper become necessary, considering its placement in a moving vehicle. The conventional bidirectional chopper achieves this by operating at high switching-frequencies. However, there are upper limits on the frequency when the power loss is considered, which means that there is a need for a more suitable bidirectional chopper.

1.1 Research Background

Over the last few decades, concern over climate change has risen steeply due to its potential ramifications on the environment, economy, and social life. This is driven primarily by the accumulation of GHG emitted from various activities. According to the IEA (international energy agency), the transportation sector is responsible for around 23 % of the global energy-related GHG emission in 2022, which translates to around 8 Gt CO_2-eq, making it the one of the major contributors [1]. Historically, road transportation is the biggest emission contributor in the transportation sector. For example, road vehicles contribute to around 73.5 % of the total transportation emission between 2013-2022, averaging around 5.7 Gt CO_2-eq, as shown in Fig. 1.1 [2]. It is followed by aviation and ship, where both

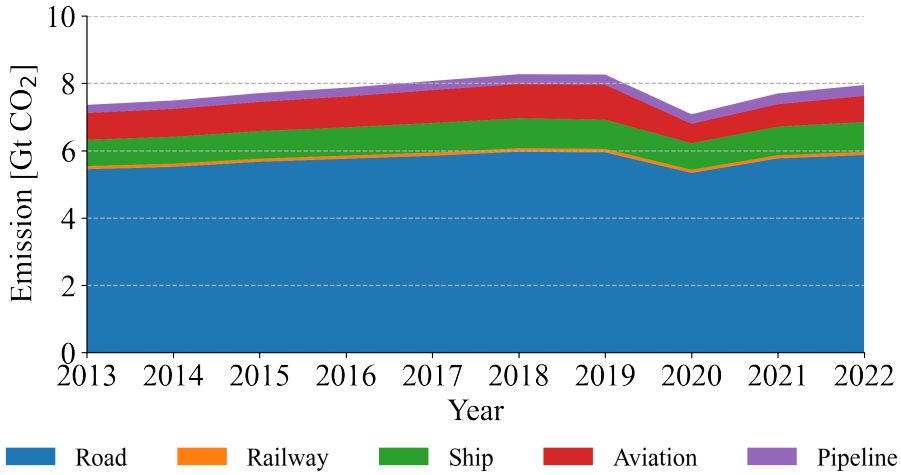

Figure 1.1: Emission produced by different transportation modes [2].

contribute around 10.8 % of the emission, which translates to 0.8 Gt CO_2-eq in average. Meanwhile, pipeline transportation is responsible for around 3.6 % in the same period, amounting to around 0.3 Gt CO_2-eq of emission, while railway only contributes around 1.1 %, averaging less than 0.1 Gt CO_2-eq. As such, there is a need to reduce the emission produced by the transportation sector, especially for the road transportation modes.

1.1.1 Electrification in the Transportation Sector

The widely accepted solution to decarbonize transportation sector is the electrification of various transportation modes (i.e., EVs (electric vehicles)), which requires a transformative shift from the conventional vehicles with ICE (internal combustion engine) that rely on fossil-fuel to those powered by electricity. Currently, researches on EVs have encompassed everything from land, air, to water transportation modes, including passenger vehicles, public transportation, and freight [3]–[6]. This is because EVs have several advantages over the conventional vehicles, including reduced GHG emission, possibility to use renewable energy, improved energy efficiency, and potentially lower operating and maintenance cost [7]–[10].

One of the main advantages of EV is the significant reduction in GHG emission. ICE produces various GHG during the fuel combustion, especially when the engine is starting and the operating temperature has not been reached, which is typically called the TTW (tank-to-wheel) emission. This includes carbon dioxide (CO_2) that is a major contributor to global warming, methane (CH_4) that is commonly produced by natural gas-powered vehicles, and nitrous oxide (N_2O) that is usually produced by diesel engines. On the other

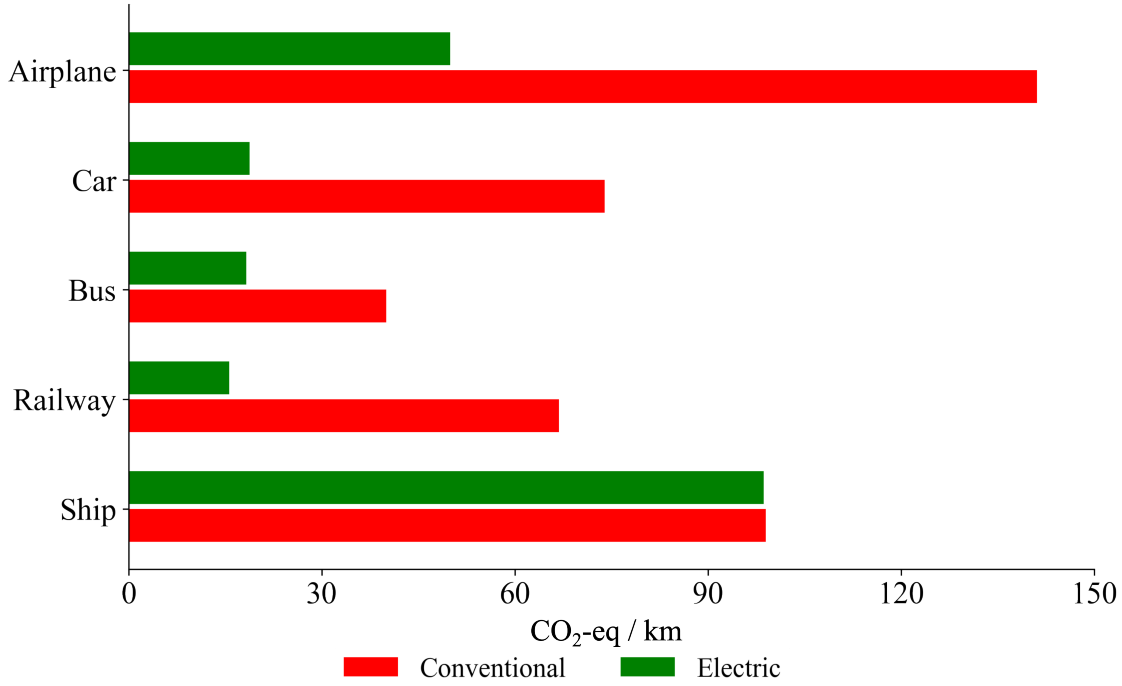

Figure 1.2: Comparison of WTW emission for different transportation modes [13].

hand, EV produces zero tailpipe emission, as it does not rely on combustion for power [11]. Although there are other types of emissions that have to be considered, such as the WTT (well-to-tank) emission that is defined as the emissions produced by the generation of electricity to produce the necessary power, the total WTW (well-to-wheel) emissions produced by the EV is lower than that of the conventional transportation [12]. WTW emission is defined as the total emissions produced when the vehicle is used, and the comparison of the WTW emission for different transportation modes is given in Fig. 1.2 [13]. Electric airplane emits around 50 g CO_2-eq per km, which is almost one-third than the conventional airplane at 141 g CO_2-eq per km. For land vehicles, the emission of electric car (18.9 g CO_2-eq per km) is less than one-forth of the conventional car (73.9 g CO_2-eq per km), the emission of electric bus (18.3 g CO_2-eq per km) is less than half of the conventional bus (40 g CO_2-eq per km), and the emission of electric railway (15.6 g CO_2-eq per km) is less than one-fourth of the conventional railway (66.9 g CO_2-eq per km). Finally, electric ship and conventional ship have similar emissions, with 98.6 g CO_2-eq per km and 99 g CO_2-eq per km, respectively.

Beside the emission reduction, the potential use of renewable sources to either directly power the vehicles or used in the electricity generation further adds to the environmental benefits of EV, where solar power is among the most extensively researched energy sources.

It can be installed on the vehicle, at charging stations, or used to generate power for the electricity grids. Direct usage on the vehicle gives an advantage in reducing the peak load in the transmission lines [14]. Meanwhile, other renewable sources (e.g., wind, hydropower, and geothermal) are more commonly used as indirect power sources by feeding electricity to the grid or the charging stations [15]–[17]. Further, using renewable sources will improve the energy independence, scalability, and sustainability of the EV systems.

Another compelling advantage of EV is the potential for improved energy efficiency. Electric motors are far more efficient than ICE, converting a higher percentage of energy from the battery directly into motion [18]. Depending on the power sources, EV maintains a higher WTW efficiency, in average, than the the conventional vehicles, where EVs with electricity supplied by renewable sources have greater WTW efficiency intervals. For example, the WTW efficiency of ICE vehicle using gasoline ranges between 11.1–26.2 % and ICE vehicle using diesel ranges between 23.7–35.5 %. Meanwhile, EV using hydroelectric has a WTW efficiency between 45.5–72.2 % and EV using solar and wind sources has a WTW efficiency between 53.5–71.4 % [19]–[21]. Moreover, land vehicles, such as electric cars and railways, can utilize regenerative braking system to further improve the efficiency [22]–[24]. Economically, EV has cost advantages in the long-term. Although the initial cost of EV can still be higher than that of conventional vehicles, lower operating and maintenance costs help balance this over time [25]. Further, the rising price of fossil-fuels and improvements on the economical aspects of its supporting technologies (i.e., battery and renewable power system) will narrow the initial cost gap between electric and conventional vehicles.

EVs are commonly DC systems, i.e., LVDC (low-voltage direct current) and MVDC (medium-voltage direct current), since DC motors are easier to control than AC motors and can efficiently provide high acceleration, simpler and stabler operation, and offer more flexibility to be integrated with renewable energy systems [26]–[28]. The voltage rating of DC EV varies widely depending on the application, size, and power requirements of the vehicle. For example, the typical operating voltage of electric railways ranges from 600 V to 3 kV, and electric cars is 300–800 V, while electric ships and aircrafts use voltage rating up to 3 kV and 5 kV, respectively [29]–[33]. Further, the operation of EVs require OESS (onboard energy storage system), which enables independence from the availability of continuous external power sources, the storing and releasing of regenerative-braking

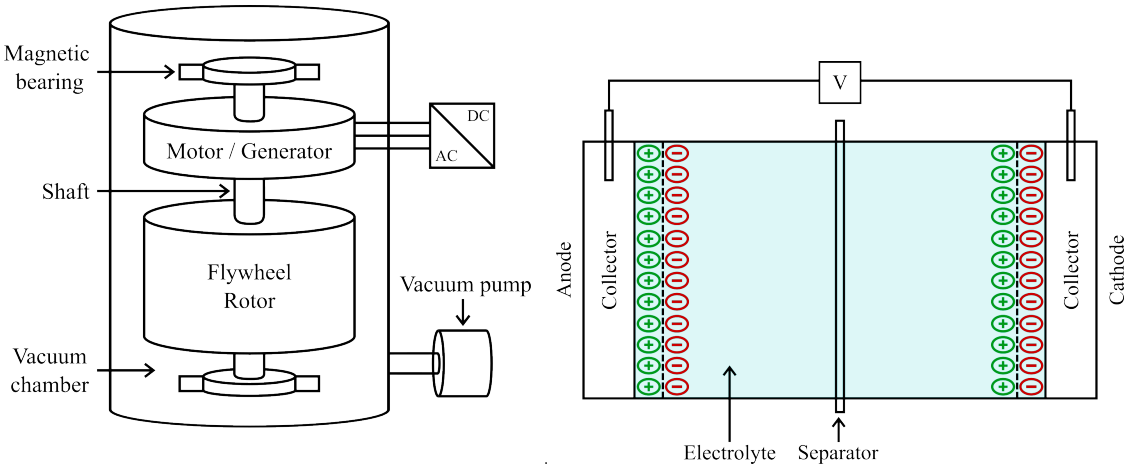

(a) (b)

Figure 1.3: Schematic diagram: (a) FESS, (b) SESS.

energy, longer travel distance, and improved efficiency [34]–[36]. There are three types of OESS commonly utilized in modern EVs: FESS (flywheel energy storage system), SESS (supercapacitor energy storage system), and BESS (battery energy storage system). Other types include hydrogen and hybrid storage systems, which will not be discussed in this dissertation.

1.1.2 Types of OESS in Electric Vehicles

A FESS generally has four main components, i.e., a rotor, a rotor bearing, an electric machine, and a power electronic interface, where the schematic diagram is shown in Fig. 1.3a. It converts electrical energy to kinetic energy and stores it by using the moment of inertia of a rotational mass located in a rotor, where the amount of stored energy depends on the form, mass, and rotational speed of the rotor. It should be noted that the rotors can be positioned either vertically or horizontally, and are designed to optimize the energy density while preserving the structural integrity of all components under the combination of rotational and thermal stresses. Depending on the rotor speed, it can be categorized as low-speed and high-speed FESS. Further, an electrical machine is connected to the rotor through a bearing to convert the kinetic energy back to electrical energy when needed. There are several advantages of the FESS, including high efficiency since it stores energy in the form of kinetic (i.e., mechanical) energy that has minimum losses, fast response time to discharge energy, high durability, and low environmental impact. However, its main disadvantages include its bulky and heavy nature compared to the other types of OESS,

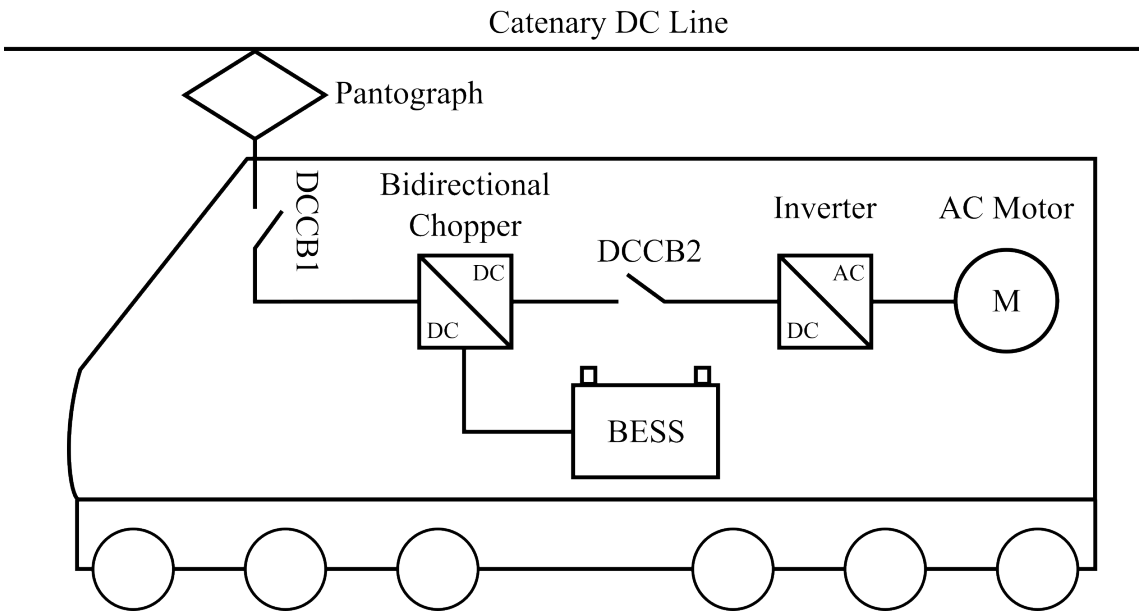

Figure 1.4: Simplified configuration of onboard BESS in electric railways.

high self-discharge rate, and high cost (especially for the high-speed types) [37]–[39].

A SESS stores energy in an electrochemical double layer, consisting of two electrodes insulated by an ion-permeable separator, as shown in Fig. 1.3b. When a voltage is applied, ions in the electrolyte gather on the surface of the electrodes, creating an electrostatic field that stores energy. This allows SESS to excel at delivering and absorbing rapid bursts of energy (i.e., high power density), making it suitable for situations where quick bursts of energy are needed, e.g., during acceleration and deceleration. Further, it has a faster charging rate than the FESS, and quite a long life-cycle, which could prove to be cost-effective in the long run. In terms of weight, the SESS is lighter than the BESS. On the other hand, SESS has low energy density, which limits its use in long-distance travel when a large capacity of storage is needed [40]–[42].

A BESS stores electricity in the form of chemical energy, and it has three main components: the anode, catode, and electrolyte. It has been widely used in EVs due to its advantages, such as high energy density, low maintenance, high efficiency, and fast response time [43]–[45]. Several differences can exist in the characteristics depending on the materials used in the battery, with the main ones being Li-ion (lithium-ion), Pb-Acid (lead-acid), and NiMH (nickel-metal hydride) [46]–[48]. Recently, the usage of supercapacitors as a support function to the BESS has been proposed, e.g., during power peaks, which could lead to a more stable operation and a higher battery lifetime [49]–[51].

When onboard BESS is used, an additional bidirectional chopper is required for volt-

age conversion between the voltage level of the power source and that of the battery. For example, Fig. 1.4 shows the simplified configuration of its application in electric railways. The utilization of BESS puts additional volume and mass on the vehicle. The typical volume of the BESS used in electric car is 50–200 dm^3 and weighs 80–600 kg, while that used in electric railway (i.e., light rail) is 450–3000 dm^3 and 900–2000 kg in volume and weight, respectively [52]–[55]. Since it is placed in a moving vehicle with limited capacity, reduction of the chopper volume and mass becomes imperative, where inductor and capacitor are the main contributors. Typically, inductor is the bulkiest and most expensive component, especially in high power applications such as EVs, while capacitor has less volume due to its higher energy density [56]–[58]. Additionally, there are more limitations to achieve volume and mass reduction of a capacitor than an inductor, e.g., the properties of dielectric materials [59]. Thus, researches focusing on reducing inductor volume and mass have been widely done. The simplest way to achieve this is by lowering the inductance value of the inductor by operating the power devices of the chopper at high switching frequencies [60]–[62]. However, when the power losses of the switching devices are considered, an upper limit exists for the operating switching frequencies. For example, the typical switching frequency for a 3.3 kV Si-IGBT (silicon-insulated gate bipolar transistors) at the catenary voltage of 1.5 kV is 600 Hz, while that of a 3.3 kV SiC-MOSFET (silicon carbide-metal oxide semiconductor field effect transistor) at the same voltage is 2 kHz [63], [64]. As such, other approaches to reduce the inductor volume and mass are needed.

1.2 Research Objectives

The purpose of this dissertation is to propose a suitable non-isolated bidirectional chopper topology for onboard BESS application in EVs that could achieve the following objectives:

1. **Reduction of the switching-ripple current** in the inductor, which consequently allows the usage of a lower inductance.

2. **Reduction of the inductor volume** used in the chopper, as a result of the application of a lower inductance value.

3. **Production of power losses that is low enough** to enable high-efficiency performances in the chopper.

4. **Improvement of the overall stability** of the chopper operation, including the situation when there is no power transfer in the chopper.

A bidirectional chopper with a single full-bridge auxiliary converter is proposed in this dissertation, where several operating conditions are introduced to achieve the previously mentioned objectives. A detailed theoretical analysis on the switching-ripple current is conducted over the wide operating voltage to evaluate the performance of the proposed chopper. Further, experiments are carried using a down-scaled model to verify the validity of the theoretical analysis results along with the associated controls in the chopper during steady- and transient-states. Finally, the efficacy of the proposed chopper is evaluated through a theoretical comparison with respect to the inductor volume, chopper volume and mass, power loss, and efficiency, with several conventional topologies.

The application of phase shift to the carrier of the auxiliary converter in the bidirectional chopper with a single full-bridge auxiliary converter is proposed to further reduce the switching-ripple current in the inductor and its associated volume. Consequently, the produced power loss in the chopper can be made lower, which raises its efficiency. To confirm this point, a detailed theoretical analysis is conducted on the switching-ripple current, and the results are confirmed through experiments using a down-scaled model. Similarly, a theoretical comparison with several topologies is done with respect to the inductor volume, power loss, and efficiency, to demonstrate the benefits of applying phase shift in the proposed chopper.

The supplementary implementation of AC-component based control is proposed to ensure smooth operations of the chopper, particularly in conditions when the DC inductor current is zero. In such condition, there is no power transfer between the voltage sources (i.e., the power source and the battery). The results of the theoretical analysis and the performances of the proposed supplementary AC-component based controls during steady- and transient-states are experimentally verified using a down-scaled model.

1.3 Dissertation Outline

The main body of this dissertation is consisted of six Chapters and two Appendices. The Chapters of the dissertation provide the main contents of the research topic. The Appendices give the details on supporting information, analysis, or calculation methods

that are used in some parts of the research. A list of publications and achievements is given after the Appendices.

- **Chapter 1** gives an introduction to the research topic that is discussed in this dissertation. It describes the benefits of EV adoption to replace conventional vehicle, where the usage of onboard energy storage system is required, compelling the necessity of this research. Research objectives are presented to provide sufficient context and the outline of this dissertation is listed to summarize the purpose of each section.

- **Chapter 2** introduces various existing topologies for non-isolated bidirectional chopper that can be used for OESS application in EV. The advantages and disadvantages of these topologies are discussed and presented as a baseline for comparison with the proposed chopper.

- **Chapter 3** presents the proposed bidirectional chopper with a single full-bridge auxiliary converter, focusing on its application in electric railways. Information on the circuit configuration, operating principle, and controls of the main and auxiliary converters are provided and discussed in details. Theoretical analysis on the switching-ripple current is conducted, where the results are further verified through experiments done using a downscaled model, along with the steady- and transient-states operations of the chopper. Finally, a comparison with other topologies, i.e., the conventional bidirectional chopper, three-level flying capacitor-based converter, and bidirectional chopper with auxiliary converter that has three cells, are given with respect to the inductor volume, chopper volume and mass, power loss, and efficiency.

- **Chapter 4** proposes the application of phase shift to the carrier of the auxiliary converter in the bidirectional chopper with a single full-bridge auxiliary converter, maintaining its focus in electric railways. Theoretical analysis on the switching-ripple current is given and the results are confirmed through experiments using a downscaled model. Comparison of the bidirectional chopper with a single full-bridge auxiliary converter with phase shift with other topologies, i.e., the conventional bidirectional chopper, three-level flying capacitor-based converter with phase shift, and bidirectional chopper with a single full-bridge auxiliary converter, is given with respect to the inductor volume, chopper volume and mass, power loss, and efficiency.

- **Chapter 5** proposes the supplementary implementation of AC component-based control in bidirectional chopper with a single full-bridge auxiliary converter to the conventional DC component-based control. Experiments under steady and transient states are performed, along with its coordinated operation with the conventional DC component-based control, to validate the operations of the AC-component based control.

- **Chapter 6** concludes the research work and all of the results presented in the previous Chapters of this dissertation. In addition, potential plans for future researches in the related topic are given for subsequent researchers and engineers.

- **Appendix A** describes the calculation methods for the theoretical analysis of the inductor and cooling system volumes to support the results shown in Chapter 3 and 4. Additionally, the thermal characteristics of the power modules based on their respective datasheets are shown.

- **Appendix B** provides the formulas to the losses considered in the power loss calculation of the chopper. The approximated loss characteristics of the power modules used in the calculations, based on their respective datasheets, are also shown to validate the results shown in Chapter 3 and 4.

Chapter 2

Literature Review

As has been mentioned in Chapter 1.2, the objectives of this research is to propose a suitable chopper topology for onboard BESS application in the electric railway systems that focuses on the inductor switching-ripple current and volume reduction, while taking the produced power losses into considerations. For the intended application, non-isolated bidirectional choppers are the most suitable, due to their characteristics that have been previously explained. This Chapter will review some of the most commonly used conventional topologies of the non-isolated bidirectional choppers and mention their advantages and disadvantages. The topologies that will be discussed are the conventional bidirectional chopper, flying capacitor chopper neutral point clamped chopper, cascaded h-bridge chopper, modular multilevel chopper, and bidirectional chopper with an auxiliary converter. Finally, a conclusion will be given based on the presented information.

Depending on the direction of the power flow, choppers can be classified into unidirectional and bidirectional. As the names entail, unidirectional choppers only allow power to flow in one direction, i.e., the power only flows from the source to the load in generation or it is absorbed by the source in regeneration, while bidirectional choppers allow power to flow in both directions [65]. Due to its characteristics, unidirectional choppers are suitable for on board loads such as safety equipments or utilities. Meanwhile, bidirectional choppers are suitable for implementations where power flow reversal is needed, such as ESS (energy storage system) applications in renewable energy systems and EVs, smart grids, EV charging stations, and others [66]–[70].

Bidirectional choppers can be classified into isolated and non-isolated choppers [71]. Isolated choppers have the advantage of galvanic isolation between the input and output

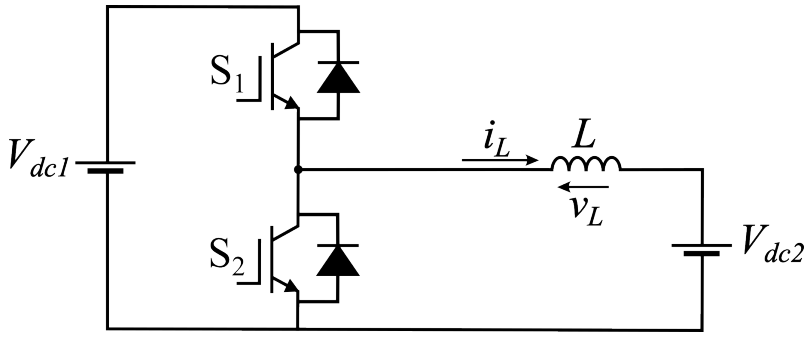

Figure 2.1: Circuit configuration of the CBC.

sides, which is typically achieved by using a transformer, so that the electrical faults in the input will not affect the output. Thus, it offers a good safety especially in high voltage applications. Further, a wide range of voltage step-up and step-down can be produced by adjusting the transformer's turn ratio, while interferences and noises can be reduced since isolation eliminates ground loops. On the other hand, in non-isolated choppers, the input and output sides share a common ground and the power is directly transferred from the former to the latter. Since no intermediate step is used (i.e., transformer), the reduction of weight, size, and cost is possible when non-isolated choppers are used. Additionally, higher efficiency can be achieved since there is no transformer loss, while the design and circuit control are comparatively simpler than the isolated choppers.

2.1 Two-Level Conventional Bidirectional Chopper

A commonly used bidirectional chopper in BESS applications is the half-bridge bidirectional chopper, which henceforth will be called the CBC (conventional bidirectional chopper) in this dissertation. The circuit configuration of the CBC is shown in Fig. 2.1, where V_{dc1} and V_{dc2} denote DC voltages of the input and output, respectively, such that $V_{dc1} > V_{dc2}$, and L is the inductor to smooth the current flow between the input and output. It uses bidirectional switches, where S_1 and S_2 are the upper and lower switches, respectively, and the duty ratios are generally controlled using a PWM (pulse-width modulation) technique. Depending on the power flow, this copper can operate either in buck or boost mode. For example, it operates in buck mode when the power flows from the high-voltage side to the low-voltage side (i.e., from V_{dc1} to V_{dc2}), while the boost mode occurs when when the power flows in the opposite direction. Due to its simple design that uses few components, it is cost-effective and can be operated at high efficiency. Thus, the

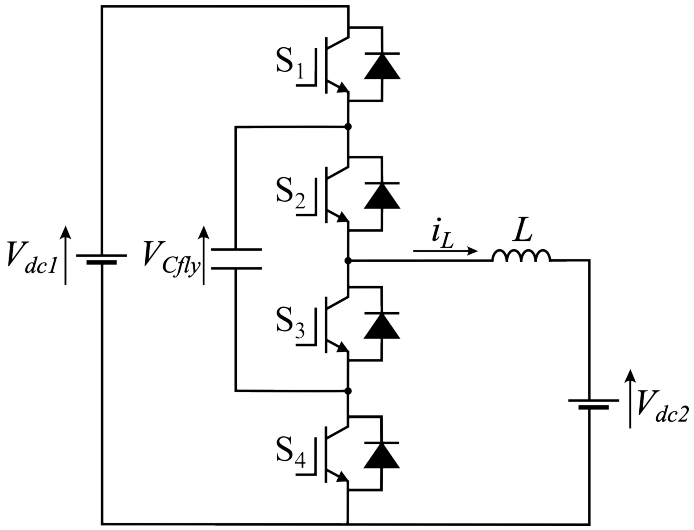

Figure 2.2: Circuit configuration of the TLFC.

CBC is conventionally employed for ESS application in EVs, renewable energy systems, and electric railways [72]–[74]. However, two-level choppers have several limitations, including limited voltage scalability, low efficiency at higher power applications, and high harmonics distortion [75]–[77]. Additionally, the reduction of the inductor volume and mass are achieved in the CBC by increasing its switching frequency, whereas an upper limit exists, as has been explained in the previous Chapter.

2.2 Multi-Level Chopper Topologies

Multi-level choppers are characterized by their ability to produce more than two voltage levels of phase voltage. This gives them the advantages in improved quality of the output waveform, less harmonic distortion, higher efficiency at higher power applications, reduced voltage stress across the power devices, and reduced inductor switching-ripple current, which makes them suitable for medium to high power applications such as electric vehicles [78]–[81]. Most commonly used topologies of the multilevel choppers include flying capacitor chopper, cascaded h-bridge chopper, and modular multilevel chopper. However, cascaded h-bridge chopper and modular multilevel chopper are less suitable for onboard EV application compared to the other topologies due to their complex control, high component-counts, and limited chopper size reduction [82]–[84].

2.2.1 Flying Capacitor Chopper

As the name suggests, the FCC (flying capacitor chopper) utilizes flying capacitors to clamp device voltage to the capacitor voltage level as the intermediate voltage levels. Its topology is made by serial connections of capacitors-clamped switching cell that allows the transfer of limited voltages to the power devices through the capacitors. By adding more flying capacitors, the chopper level can be increased. The circuit configuration of a TLFC (three-level flying capacitor converter) is shown in Fig. 2.2 [85]–[87]. It can produce three voltage levels of 0, V_{Cfly}, and V_{dc1}, where V_{Cfly} is the flying DC-capacitor voltage and V_{dc1} is the DC-source voltage. If the flying DC-capacitor voltage is set to be half of the DC-source voltage (i.e., $V_{Cfly} = \frac{V_{dc1}}{2}$), and no phase shift is considered in the operation, the TLFC can work as a bidirectional chopper with the voltage of $\frac{V_{dc1}}{2}$ at the high-voltage side and V_{dc2} at the low-voltage side, or that with $\frac{V_{dc1}}{2}$ at the high-voltage side and $V_{dc2} - \frac{V_{dc1}}{2}$ at the low-voltage side. Consequently, the maximum peak-to-peak current can be reduced to half of that produced by the CBC under the same switching frequency [88]. Meanwhile, if phase shift is applied to the power devices in the chopper, it is able to produce lower maximum peak-to-peak current that is a quarter of that produced by the CBC under the same switching frequency.

One of the major advantages of the FCC is its phase redundancies, which refers to the multiple ways it has to produce the same voltage level. For example, when $V_{Cfly} = \frac{V_{dc1}}{2}$ is held, the TLFC shown in Fig.2.2 is able to produce $\frac{V_{dc1}}{2}$ by setting S_1 and S_3 to ON and S_2 and S_4 to OFF, and S_2 and S_4 to ON and S_1 and S_3 to OFF. This is particularly useful for the achievement of capacitor-voltage-balancing control techniques and fault tolerance, and could minimize power losses [89]. Due to these merits, numerous studies focusing on its control and applications in power systems have been conducted [90]–[92]. However, the FCC suffers from several drawbacks, including an increased number of flying-capacitor as the level increases, difficulties to monitor and balance the capacitor voltages that could lead to increased voltage ripple, and complex controls where the controls of the inductor current and capacitor voltage are strongly coupled [93]–[95].

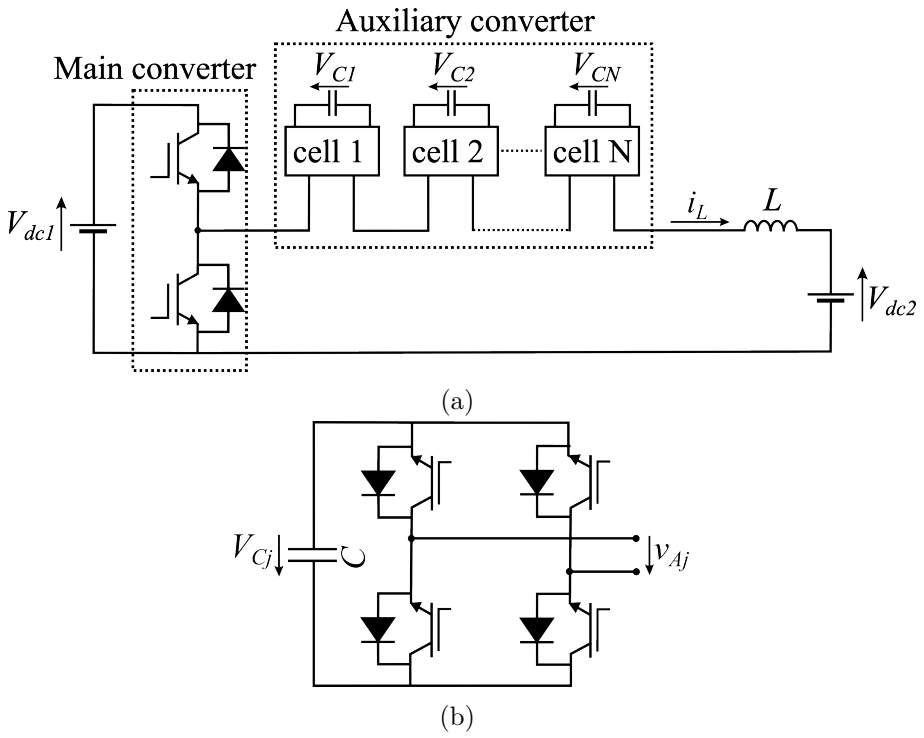

Figure 2.3: Circuit configuration of the BCAC: (a) Overall circuit, (b) Full-bridge converter cell of the auxiliary converter.

2.2.2 Bidirectional Chopper with Auxiliary Converter

The BCAC (bidirectional chopper with an auxiliary converter) combines a CBC with an auxiliary converter based on multiple cascaded single-phase full-bridge converter cells [96]–[102]. The circuit configuration of the BCAC is shown in Fig. 2.3, where V_{dc1} and V_{dc2} are the DC-voltage sources of the high-voltage and low-voltage sides, respectively. Meanwhile, V_{C1}, V_{C2}, and V_{CN} are the DC-capacitor voltages of the cells, with N being the number of cells in the auxiliary converter. It should be noted that only reactive power is processed by the auxiliary converter in the BCAC ideally, with no active power. Thus, the BCAC is a full power converter, and not a partial power DC-DC converter that processes a percentage of the converter total power [103].

In the BCAC, the switching-ripple current can be reduced by using the auxiliary converter as an active power filter that eliminates the AC voltage produced by the main converter. To do this, the switching frequencies of the main converter, f_{SM}, needs to be equal or less than that of the auxiliary converter, f_{SA} (i.e., $f_{SM} \leq f_{SA}$). It should be noted that the ripple frequency will increase when f_{SA} is raised. Additionally, to make sure that the auxiliary converter can work as an active power filter under all conditions

when $V_{dc1} \geq V_{dc2}$, the relationship $NV_C \geq V_{dc1}$ should hold. For example, by setting $N = 3$, $f_{SA} = 4f_{SM}$, and $V_C \leq \frac{V_{dc1}}{3}$, the switching-ripple current can be reduced to $\frac{1}{60}$ of that the CBC [96], [97]. Further, power-flow control can be achieved in high switching frequency performance under $N = 2$, $f_{SM} = 8\,\text{kHz}$, and $f_{SA} = 16\,\text{kHz}$, where the equivalent switching frequency is 64 kHz ($= 2Nf_{SA}$), using a small inductor with an inductance of 50 µH [98]. In [99], [100], interleaved topologies utilizing BCAC have been proposed to reduce the mass and volume of the chopper by setting $N = 3$, $M = 3$, $f_{SA} = 4f_{SM}$, and $V_C = \frac{V_{dc1}}{3}$, where M is the number of sub-converters in the interleaved topology. A noninverting BCAC that is able to operate in buck, buck-boost, and boost modes has been proposed in [101]

Other merits of the BCAC include the possibility to use the auxiliary converter as a solid-state DC circuit breaker equivalent. By monitoring the inductor current, short-circuit fault can be detected. Specifically, the circuit breaker operation is triggered when it reaches a specified threshold value. Since the measurement of the inductor current is also required for control purposes, no additional sensors are required for the circuit breaker operation. Additionally, the auxiliary converter can interrupt the inductor current when there is undesirable overcurrent much faster than mechanical DC circuit breakers. Considering that no arc occurs in the auxiliary converters, an arc extinguishing mechanism required for the mechanical DC circuit breakers is not needed, and high reliability can be realized. In addition, there is flexibility to place the main and auxiliary converters, since both converters can work as independent voltage sources. Due to the same reason, the decouple of controls between the inductor current and the DC-capacitor voltage can be achieved in the BCAC, which is not the case in FCC [102]. However, it suffers from increased power loss and potentially the cost, due to the installations of multiple cells in the auxiliary converter.

2.3 Conclusion

This Chapter has reviewed several conventional non-isolated bidirectional chopper topologies. The presented choppers are classified on the voltage levels they can produce into two-level and multi-level choppers. The two-level conventional bidirectional chopper (CBC) has the advantage in its simple design. However, there is a restriction in its ability to

reduce the inductor volume and mass due to the limitation on the switching frequency, especially in high power applications. On the other hand, multi-level chopper topologies offers more flexibility in reducing the inductor volume and mass through the switching-ripple current reduction. The flying capacitor chopper (FCC) has the advantage in its phase redundancies and voltage balancing control. However, its inductor current and capacitor voltage controls are strongly coupled. The bidirectional chopper with an auxiliary converter (BCAC) is able to reduce the switching-ripple current to $\frac{1}{60}$ of that the CBC. However, it produces a significant amount of power losses, which lowers its efficiency.

Chapter 3

Bidirectional Chopper with Single Full-Bridge Auxiliary Converter

This Chapter presents the proposal of a bidirectional chopper with a single full-bridge auxiliary converter (BCSAC), focusing on its application in electric railway systems. The proposed chopper is based on the bidirectional chopper with an auxiliary converter (BCAC), with the aims to reduce the inductor volume without a significant power loss compensation. In this Chapter, the circuit configuration and operating principle of the BCSAC are described, which includes the explanation regarding the role of the auxiliary converter in reducing the switching-ripple current of the inductor (i.e., the inductance) and the operating conditions set with the intention to reduce the generated power loss. The control methods of both the main and auxiliary converters are discussed, where the functions are separated into inductor current control, capacitor voltage control, and ripple-current mitigation. Theoretical analysis and comparison on the switching-ripple current, inductor volume, chopper volume and mass, power loss, and efficiency with other topologies are given to evaluate the efficacy of the BCSAC. Finally, the validity of the theoretical analysis on the switching-ripple current, as well as the confirmation of the BCSAC performances during steady and transient states are confirmed through experiments using a 2 kW down-scaled model.

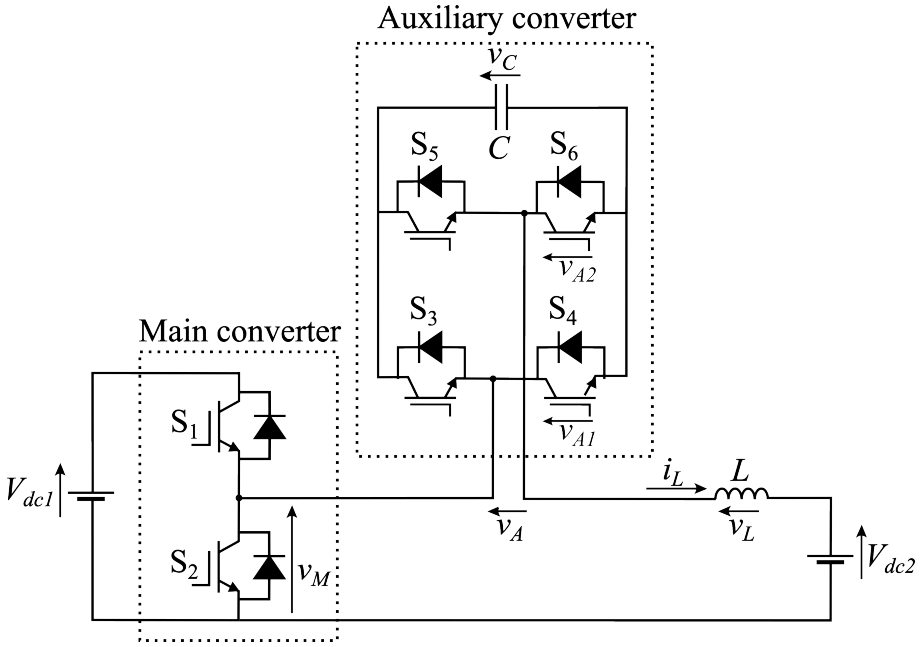

Figure 3.1: Circuit configuration of the BCSAC.

3.1 Circuit Configuration

The circuit configuration of the BCSAC is shown in Fig. 3.1, which is consisted of a CBC as the main converter, a single-phase full-bridge converter equipped with a floating DC-capacitor as the auxiliary converter, and an inductor. The main converter is connected to two DC-voltage sources, V_{dc1} as the high-voltage-side voltage and V_{dc2} as the low-voltage-side voltage, while v_M indicates the low-voltage-side voltage of the main converter. S_1 and S_2 indicate the upper and lower switching devices of the main converter, respectively. The auxiliary converter is connected in series with the main converter and the inductor, where v_A indicates the auxiliary converter voltage, v_C indicates the DC-capacitor voltage, v_L indicates the inductor voltage, and i_L indicates the inductor current. S_3 and S_4 indicate the upper and lower switching devices of one leg of the auxiliary converter that is connected to the main converter, respectively, and v_{A1} shows the low-voltage-side voltage of the leg. Meanwhile, S_5 and S_6 indicate those of another leg that is connected to the inductor, and v_{A2} shows the low-voltage-side voltage of the leg. Finally, triangular carrier waveforms are applied to the main and auxiliary converters, i.e., $\mathrm{tri_M}$ and $\mathrm{tri_A}$, respectively, where the relationship $\mathrm{tri_M} = \mathrm{tri_A}$ holds.

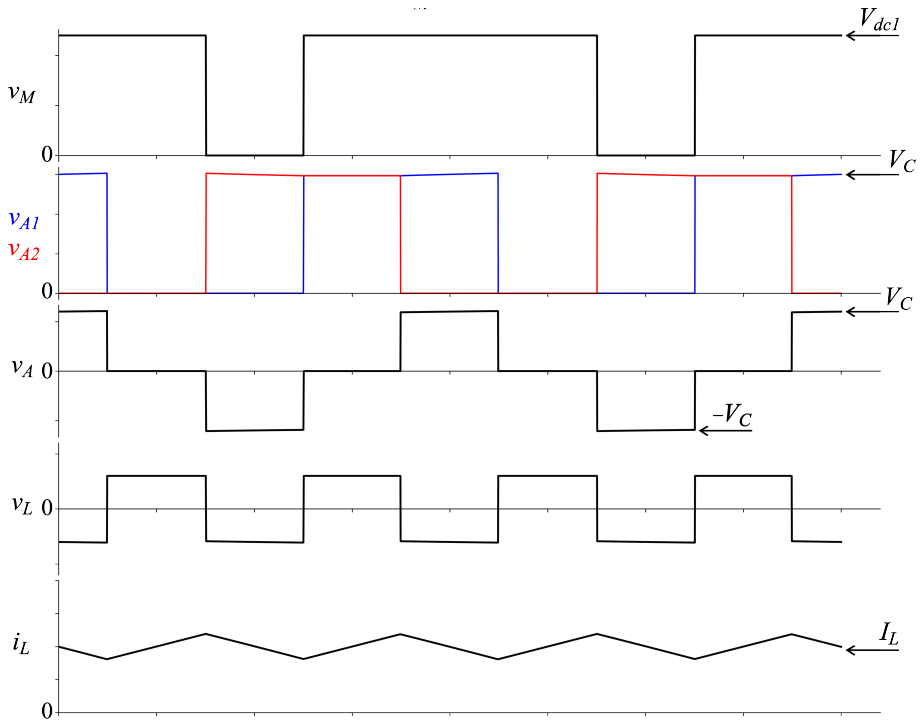

Figure 3.2: Example of the ideal voltage and current waveforms of the BCSAC.

3.2 Operating Conditions and Principle

3.2.1 Operating Conditions

The BCSAC operates under the following conditions:

1. The auxiliary converter consists of only a single full-bridge cell ($N = 1$).
2. The switching frequency of the main converter, f_{SM}, and that of the auxiliary converter, f_{SA}, are the same (i.e., $f_{SM} = f_{SA}$).
3. The DC-capacitor voltage is half of the DC-source voltage at the high-voltage side (i.e., $V_C = \frac{V_{dc1}}{2}$).

The focus of these operating conditions is to reduce the power loss and cost of the BCSAC, compared to the BCAC. The first condition is applied to reduce the number of switching devices in the auxiliary converter, which consequently should reduce the conduction loss, switching loss, and cost. Further, the second condition is applied to reduce the switching loss in the auxiliary converter, compared to when the relationship $f_{SA} > f_{SM}$ holds, as used in [96]–[98]. It should be noted that the equivalent switching frequency of v_A is $2f_{SA}$, due to the application of unipolar PWM in the auxiliary converter. Finally, by setting the

DC-capacitor voltage as in the second condition, the voltage rating of the power devices in the auxiliary converter can be reduced by a factor of 0.5, which is expected to reduce the switching loss and cost. To further verify the advantage of setting $V_C = \frac{V_{dc1}}{2}$, the comparison between different settings of V_C is given in Appendix A.

However, the application of these conditions come with its potential drawbacks. For example, setting the DC-capacitor voltage to $V_C = \frac{V_{dc1}}{2}$ could limit the auxiliary converter function as an active power filter, since it may not be able to output the necessary v_A. Further, setting the frequency of the auxiliary converter to $f_{SA} = f_{SM}$ will decrease the frequency of the ripple component in the inductor. Ultimately, these drawbacks may result in an increased switching-ripple current. As such, a detailed theoretical analysis of the switching-ripple current is required to confirm it, which is provided in Chapter 3.4.

3.2.2 Operating Principle

An example of the ideal voltage and current waveforms of the BCSAC is shown in Fig. 3.2. When the deadtime in the main converter is zero, the main converter voltage, v_M, in the BCSAC is given by:

$$v_M = \begin{cases} V_{dc1} & (\mathrm{S_1}\text{: ON, } \mathrm{S_2}\text{: OFF}) \\ 0 & (\mathrm{S_1}\text{: OFF, } \mathrm{S_2}\text{: ON}) \end{cases}, \tag{3.1}$$

where v_M consists of the DC component, $(v_M)_{dc}$, and the AC component, $(v_M)_{ac}$. If the duty ratio of $\mathrm{S_1}$ is assumed to be d_M, $(v_M)_{dc}$ is given by:

$$(v_M)_{dc} = d_M V_{dc1}. \tag{3.2}$$

From (3.1) and (3.2), $(v_M)_{ac}$ can be determined as:

$$(v_M)_{ac} = \begin{cases} (1 - d_M)\, V_{dc1} & (\mathrm{S_1}\text{: ON, } \mathrm{S_2}\text{: OFF}) \\ -d_M V_{dc1} & (\mathrm{S_1}\text{: OFF, } \mathrm{S_2}\text{: ON}) \end{cases}. \tag{3.3}$$

Meanwhile, when the deadtimes in the auxiliary converter are zero, v_{A1} and v_{A2} are given by:

$$v_{A1} = \begin{cases} V_C & (\mathrm{S_3}\text{: ON, } \mathrm{S_4}\text{: OFF}) \\ 0 & (\mathrm{S_3}\text{: OFF, } \mathrm{S_4}\text{: ON}) \end{cases} \tag{3.4}$$

$$v_{A2} = \begin{cases} V_C & (\mathrm{S_5}\text{: ON, } \mathrm{S_6}\text{: OFF}) \\ 0 & (\mathrm{S_5}\text{: OFF, } \mathrm{S_6}\text{: ON}) \end{cases}, \tag{3.5}$$

where $v_A = v_{A1} - v_{A2}$.

For the auxiliary converter to function as an active power filter, its AC output, $(v_A)_{ac}$, has to be equal to that of the main converter (i.e., $(v_A)_{ac} = (v_M)_{ac}$), so that the AC component in the inductor can be reduced to zero. Considering that $(v_M)_{ac}$ has the maximum value of V_{dc1} and the minimum value of $-V_{dc1}$ based on (3.3), $(v_A)_{ac}$ should have the same maximum and minimum values as $(v_M)_{ac}$. In the operation of the BCAC, V_C must satisfy $V_C \geq |(v_A)_{ac}|$, as has been explained in Chapter 2.2.2. When (3.3) is considered, this means that the relationship $V_C \geq V_{dc1}$ should be satisfied to enable the auxiliary converter to work as an active power filter under all conditions when $V_{dc1} \geq V_{dc2}$. However, the DC-capacitor voltage in the BCSAC is set to $V_C = \frac{V_{dc1}}{2}$ because of the reasons mentioned in Chapter 3.2.1. Consequently, a DC component may occur in v_A if the auxiliary converter attempts to produce the AC voltage given in (3.3) as a result of overmodulation in the converter. It should be noted that since v_A is an AC component and i_L is a DC component, the auxiliary converter only processes reactive power.

3.2.2.1 Voltage Compensation on v_A

To solve the overmodulation problem mentioned above, normalization should be applied to $(v_A)_{ac}$ to limit its maximum and minimum values to $0.5V_{dc1}$ and $-0.5V_{dc1}$, respectively (i.e., $-0.5V_{dc1} \leq (v_A)_{ac} \leq 0.5V_{dc1}$). Under the normalization, the value of $(v_M)_{ac}$ (i.e., $(v_A)_{ac}$) given by (3.3) should be regulated according to the following considerations:

- The value of $(v_A)_{ac}$ under $0 \leq d_M < 0.5$ is fixed to $0.5d_M$ when $\mathrm{S_1}$ is ON and $\mathrm{S_2}$ is OFF.

- The value of $(v_A)_{ac}$ under $0.5 \leq d_M \leq 1$ is fixed to $-0.5d_M$ when $\mathrm{S_1}$ is OFF and $\mathrm{S_2}$

is ON.

- The average value of $(v_A)_{ac}$ in one switching period T_{sw} is zero (i.e., $\int^{T_{sw}} (v_A)_{ac}\, dt = 0$).

Under these considerations, the value of $(v_A)_{ac}$ can be differently determined relative to the d_M. When $0 \leq d_M < 0.5$, it is given by:

$$(v_A)_{ac} = \begin{cases} 0.5V_{dc1} & (\mathrm{S_1}\text{: ON, } \mathrm{S_2}\text{: OFF}) \\ -d_M V_{dc1} + \frac{{d_M}^2 - 0.5 d_M}{d_M - 1} V_{dc1} & (\mathrm{S_1}\text{: OFF, } \mathrm{S_2}\text{: ON}) \end{cases}. \tag{3.6}$$

Meanwhile, $(v_A)_{ac}$ when $0.5 \leq d_M \leq 1$ is given by:

$$(v_A)_{ac} = \begin{cases} (1 - d_M)\, V_{dc1} + \frac{{d_M}^2 - 1.5 d_M + 0.5}{d_M} V_{dc1} & (\mathrm{S_1}\text{: ON, } \mathrm{S_2}\text{: OFF}) \\ -0.5 V_{dc1} & (\mathrm{S_1}\text{: OFF, } \mathrm{S_2}\text{: ON}) \end{cases}. \tag{3.7}$$

Based on (3.3), (3.6), and (3.7), the relationship $(v_A)_{ac} = (v_M)_{ac}$ holds when $d_M = 0.5$. In this situation, the frequency component f_{SM} contained in $(v_M)_{ac}$ is canceled out by the auxiliary converter so that no frequency component of f_{SM} exists in the inductor current. On the contrary, the relationship $(v_A)_{ac} = (v_M)_{ac}$ does not hold when $d_M \neq 0.5$. In this situation, the frequency component of f_{SM} remains in the inductor current.

3.3 Control Method

Based on the function, the control methods of the BCSAC can be mainly separated into inductor current control and DC-capacitor control. The control method closely resembles that of the BCAC introduced in [96]–[98], but differing primarily in the inductor current control. While [96]–[98] achieves the inductor current conrol through the main converter, the BCSAC uses the auxiliary converter to undertake that function. Since the equivalent switching frequency of the auxiliary converter is two times that of the main converter, as has been mentioned in Chapter 3.2.1, a more precised current controllability can be achieved.

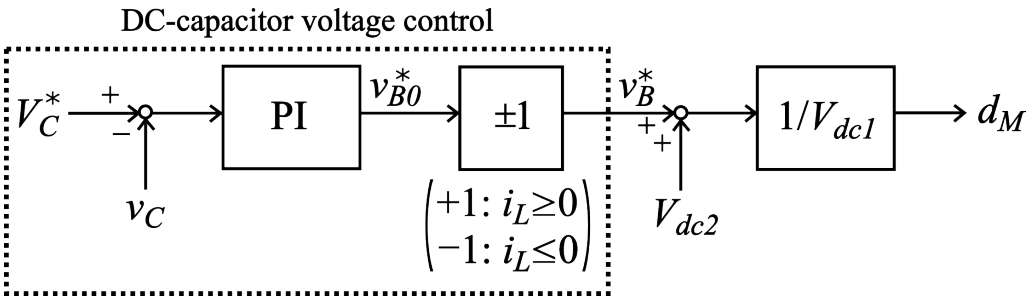

Figure 3.3: Block diagram of the main converter control.

3.3.1 Main Converter Control

The block diagram of the main converter control is shown in Fig. 3.3, where the objective is to regulate the DC-capacitor voltage. More specifically, the traditional PI (proportional-integral) control is applied to make the difference between the DC-capacitor voltage actual value, v_C, and its reference value, V_C^*, become zero, which generates the voltage reference v_{B0}^*. It should be noted that the polarity of v_{B0}^* is alternated based on that of the inductor current. For example, when $V_C^* > v_C$, the resulted v_B^* is as follows:

$$v_B^* = \begin{cases} v_{B0}^* & (i_L > 0) \\ -v_{B0}^* & (i_L < 0) \end{cases}. \tag{3.8}$$

Subsequently, V_{dc2} is added to v_B^* as a feedforward control, followed by the normalization by V_{dc1}. As a result, the duty ratio of S_1, d_M, with a maximum value of +1 and a minimum value of zero is produced, which can be expressed as:

$$d_M = \frac{v_B^* + V_{dc2}}{V_{dc1}}. \tag{3.9}$$

Finally, it is compared with $\mathrm{tri_M}$, which has the same maximum and minimum values.

To explain the principle of the DC-capacitor voltage control, a positive DC-inductor current of $i_L = I_L\,(> 0)$ is assumed to flow in the circuit. The DC power at the high-voltage side of the main converter is given from Fig. 3.3, (3.2), and (3.9) as:

$$(P_M)_{dc} = (v_M)_{dc}\, I_L = d_M V_{dc1} I_L = (v_B + V_{dc2})\, I_L. \tag{3.10}$$

where v_B is the actual voltage used for the DC-capacitor voltage control, and the relationship $v_B = v_B^*$ is assumed to hold. When $v_C = V_C^*$, the DC power at the low-voltage

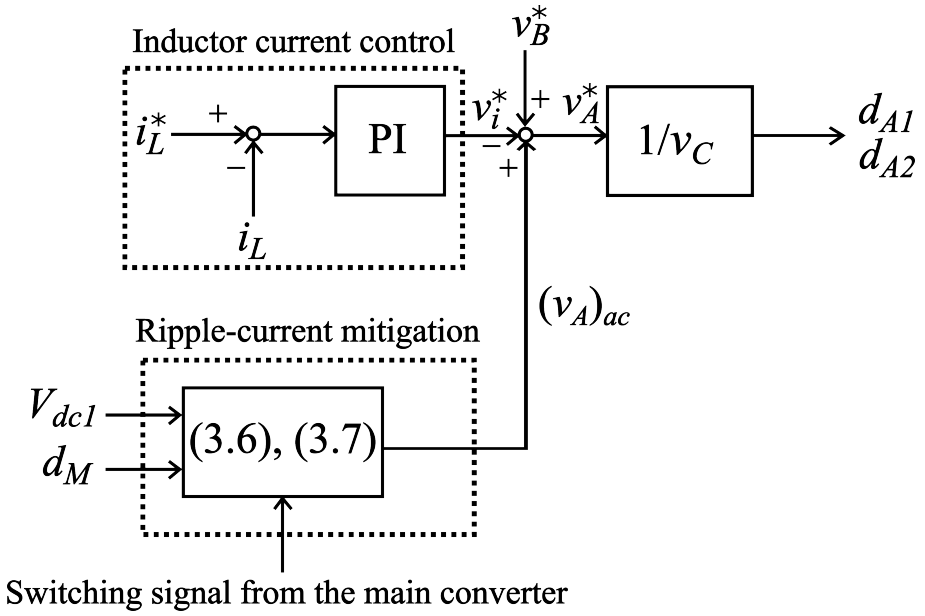

Figure 3.4: Block diagram of the auxiliary converter control.

sides of the main converter and the BCSAC are the same (i.e., $(v_M)_{dc} I_L = V_{dc2} I_L$), since the produced v_B is zero. In this case, there is no power flowing in the auxiliary converter. Meanwhile, when $v_C < V_C^*$, a positive v_B^* is produced and a positive power is formed between v_B and i_L. Subsequently, the resulted DC power is superimposed on $(v_M)_{dc} I_L$. This means that the relationship $(v_M)_{dc} I_L > V_{dc2} I_L$ holds in the circuit. Simultaneously, the auxiliary converter receives this power by producing v_B^*, as will be shown in Chapter 3.3.2. As a result, a positive power $V_{dc2} I_L$ flows into the auxiliary converter and v_C is increased. In other words, all of the additional power superimposed on the main converter flows to the auxiliary converter. It should be noted that the voltage component v_B^* produced by the main and auxiliary converters cancel each other out so that it does not affect the current control. Thus, the decouple between the DC-capacitor voltage control and the inductor current control can be achieved.

3.3.2 Auxiliary Converter Control

The block diagram of the auxiliary converter control is shown in Fig. 3.4, where the objective is to regulate the inductor current and mitigate the ripple-current. In the current control, the traditional PI control is used to make the difference between the inductor current actual value, i_L, and its reference value, i_L^*, become zero, which generates the voltage command v_i^*. Subsequently, $(v_A)_{ac}$ coming from the ripple-current mitigation control that is obtained from (3.6) and (3.7), and the voltage reference produced from

the main converter control, v_B^*, are added to v_i^* as a feedforward control. It produces the voltage reference of the auxiliary converter, v_A^*, which is followed by the normalization by v_C. As a result, the duty ratio of S_3, d_{A1}, and that of S_5, d_{A2}, with a maximum value of $+1$ and a minimum value of -1 are produced. Considering the application of unipolar PWM in the auxiliary converter, the duty ratios d_{A1} and d_{A2} can be expressed as:

$$d_{A1} = \frac{v_A^*}{v_C} = \frac{-v_i^* + v_B^* + (v_A)_{ac}}{v_C} \tag{3.11}$$

$$d_{A2} = -\frac{v_A^*}{v_C} = \frac{v_i^* - v_B^* - (v_A)_{ac}}{v_C}. \tag{3.12}$$

However, the d_{A1} and d_{A2} have to be further normalized to have a maximum value of $+1$ and a minimum value of zero. Finally, the newly obtained values of the d_{A1} and d_{A2} are compared with $\mathrm{tri_A}$, which has the same maximum and minimum values as them.

It is necessary to discern the difference between v_B^* and v_i^*. When there is no power loss in the BCSAC, the relationship $v_B^* = 0$ holds under the steady state. On the other hand, the relationship $v_i^* \neq 0$ holds under the same condition due to the existence of a DC voltage in v_A, which originates from the pulse-width modulation. Consequently, it has to be canceled v_i^*, meaning that the DC component of v_i^* is required to realize the average of v_A in one switching period become zero and achieve the current control. Further, the value of v_i^* will affect the value of the switching-ripple current, as will be explained in Chapter 3.4.

3.4 Theoretical Analysis on Switching-Ripple Current

As has been explained in Chapter 3.2.1, the switching-ripple current may increase due to some of the operating conditions used in the BCSAC. To confirm this point, a detailed theoretical analysis is conducted on the switching-ripple current.

3.4.1 Assumptions Used in the Analysis

The following assumptions are applied in the following analysis of the switching-ripple current:

- Steady-state operation with no power loss is considered.
- The deadtimes of the main and auxiliary converters are zero.

- The relationship $V_C = \frac{V_{dc1}}{2}$ holds, where the AC component in the DC-capacitor voltage is assumed to be zero.

Under the first assumption, the voltage reference v_B^* used for the DC-capacitor voltage is zero, as described in Chapter 3.3.2. As such, d_M obtained from (3.9) becomes:

$$d_M = \frac{V_{dc2}}{V_{dc1}}. \tag{3.13}$$

Further, d_{A1} and d_{A2} obtained from (3.11) and (3.12) becomes:

$$d_{A1} = \frac{-v_i^* + (v_A)_{ac}}{v_C} \tag{3.14}$$

$$d_{A2} = \frac{v_i^* - (v_A)_{ac}}{v_C}. \tag{3.15}$$

It should be noted that d_M, d_{A1}, and d_{A2} can be compared with tri_M because the relationship $\text{tri}_\text{M} = \text{tri}_\text{A}$ holds, as mentioned in Chapter 3.1. Meanwhile, the validity of the second assumption holds when the deadtime is sufficiently shorter than the switching period. Finally, considering the difference of the $(v_A)_{ac}$ equations relative to d_M (i.e., from (3.6) and (3.7)), the theoretical analysis on the switching-ripple current is done separately for d_M in the ranges of $0 \leq d_M < 0.5$ and $0.5 \leq d_M \leq 1$.

3.4.2 When $0 \leq d_M < 0.5$

The example of the ideal voltage and current waveforms of the BCSAC when $d_M = 0.25$ is shown in Fig. 3.5, where the following assumptions are considered:

- θ_1 and θ_6 are the intersection points between tri_M and d_M.
- θ_2 and θ_5 are the intersection points between tri_M and d_{A1}.
- θ_3 and θ_4 are the intersection points between tri_M and d_{A2}.
- The relationships $\theta_1 \leq \theta_3$, $\theta_2 \leq \theta_3$, $\theta_4 \leq \theta_6$, and $\theta_5 \leq \theta_6$ hold.

Based on Fig. 3.5, θ_1 and θ_6 can be determined as:

$$\theta_1 = \pi d_M \tag{3.16}$$

$$\theta_6 = 2\pi - \pi d_M, \tag{3.17}$$

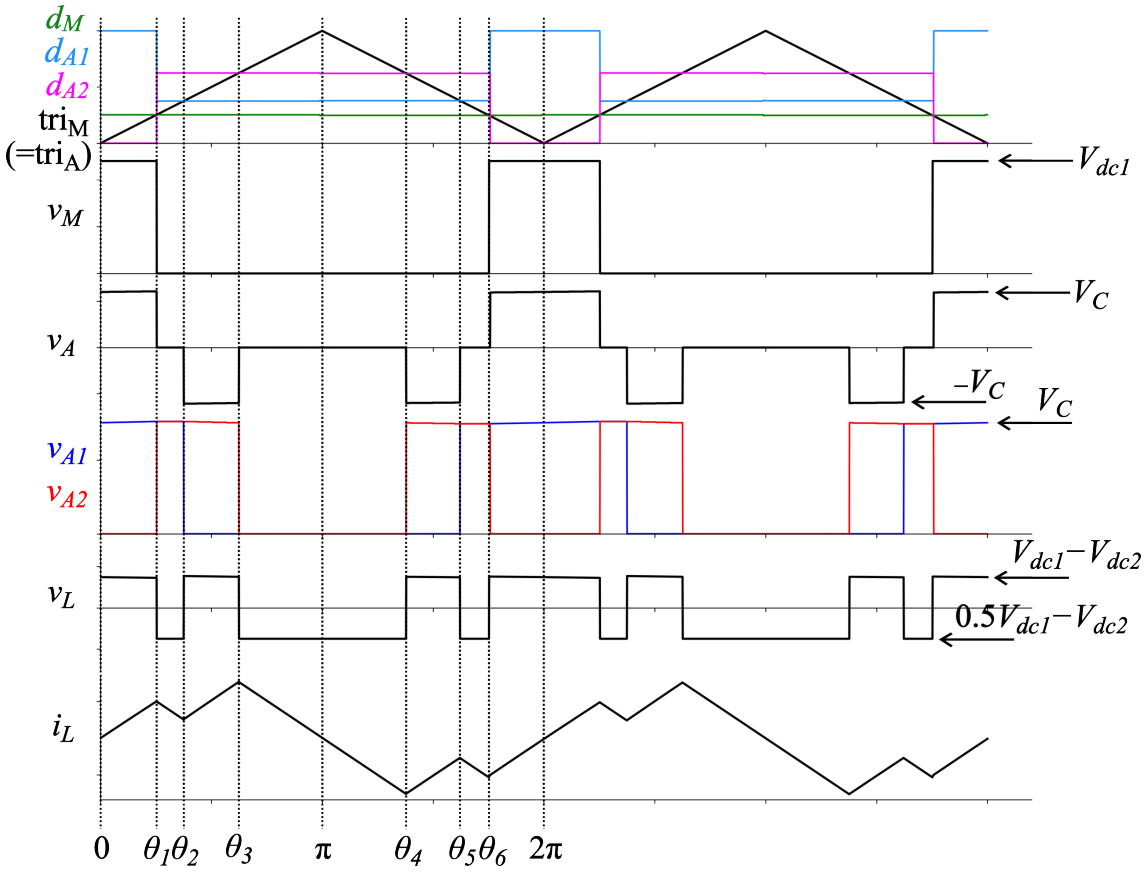

Figure 3.5: Ideal voltage and current waveforms of the BCSAC when $d_M = 0.25$.

where the relationship $\theta_1 \leq \theta_6$ always holds. Based on (3.1), v_M is given by:

$$v_M = \begin{cases} V_{dc1} & (0 \leq \theta < \theta_1, \theta_6 < \theta \leq 2\pi) \\ 0 & (\theta_1 \leq \theta \leq \theta_6) \end{cases}. \tag{3.18}$$

Based on (3.6), (3.14), and (3.15), while also applying $V_C = \frac{V_{dc1}}{2}$, the duty ratios d_{A1} and d_{A2} are given by:

$$d_{A1} = \begin{cases} -\frac{2v_i^*}{V_{dc1}} + 1 & (0 \leq \theta < \theta_1, \theta_6 < \theta \leq 2\pi) \\ -\frac{2v_i^*}{V_{dc1}} + \frac{1}{d_M - 1} + 1 & (\theta_1 \leq \theta \leq \theta_6) \end{cases} \tag{3.19}$$

$$d_{A2} = \begin{cases} \frac{2v_i^*}{V_{dc1}} - 1 & (0 \leq \theta < \theta_1, \theta_6 < \theta \leq 2\pi) \\ \frac{2v_i^*}{V_{dc1}} - \frac{1}{d_M - 1} - 1 & (\theta_1 \leq \theta \leq \theta_6) \end{cases}. \tag{3.20}$$

Since d_{A1} and d_{A2} obtained from (3.19) and (3.20) are in the ranges of $-1 \leq d_{A1} \leq 1$ and $-1 \leq d_{A2} \leq 1$, the duty ratios need to be further normalized to the ranges of $0 \leq d_{A1} \leq 1$

and $0 \leq d_{A2} \leq 1$. The normalized d_{A1} and d_{A2} are given as:

$$d_{A1} = \begin{cases} -\frac{v_i^*}{V_{dc1}} + 1 & (0 \leq \theta < \theta_1, \theta_6 < \theta \leq 2\pi) \\ -\frac{v_i^*}{V_{dc1}} + \frac{0.5}{d_M - 1} + 1 & (\theta_1 \leq \theta \leq \theta_6) \end{cases} \tag{3.21}$$

$$d_{A2} = \begin{cases} \frac{v_i^*}{V_{dc1}} & (0 \leq \theta < \theta_1, \theta_6 < \theta \leq 2\pi) \\ \frac{v_i^*}{V_{dc1}} - \frac{0.5}{d_M - 1} & (\theta_1 \leq \theta \leq \theta_6) \end{cases}. \tag{3.22}$$

Based on Fig. 3.5 and (3.21), θ_2 and θ_5 can be determined as:

$$\theta_2 = \pi \left(-\frac{v_i^*}{V_{dc1}} + \frac{0.5}{d_M - 1} + 1 \right) \tag{3.23}$$

$$\theta_5 = 2\pi - \pi \left(-\frac{v_i^*}{V_{dc1}} + \frac{0.5}{d_M - 1} + 1 \right). \tag{3.24}$$

Meanwhile, based on Fig. 3.5 and (3.22), θ_3 and θ_4 can be determined as:

$$\theta_3 = \pi \left(\frac{v_i^*}{V_{dc1}} - \frac{0.5}{d_M - 1} \right) \tag{3.25}$$

$$\theta_4 = 2\pi - \pi \left(\frac{v_i^*}{V_{dc1}} - \frac{0.5}{d_M - 1} \right). \tag{3.26}$$

Further, the value of v_A from θ_1 through θ_6 is given from Fig. 3.5 by:

$$v_A = \begin{cases} V_C & (0 \leq \theta \leq \theta_1) \\ 0 & (\theta_1 < \theta \leq \theta_2) \\ -V_C & (\theta_2 < \theta \leq \theta_3) \\ 0 & (\theta_3 < \theta \leq \theta_4) \\ -V_C & (\theta_4 < \theta \leq \theta_5) \\ 0 & (\theta_5 < \theta \leq \theta_6) \\ V_C & (\theta_6 < \theta \leq 2\pi) \end{cases}. \tag{3.27}$$

In the BCSAC, the power supplied into the auxiliary converter is given by:

$$P_A = v_A i_L. \tag{3.28}$$

When i_L is a DC quantity, v_i^* in the inductor current control will be adjusted so that v_A

under the steady-state contains only the AC component. Hence, the following relationship holds:

$$\int_0^{2\pi} v_A d\theta = V_C \left(\theta_1 + \theta_2 + \theta_4 + 2\pi - \theta_3 - \theta_5 - \theta_6\right) = 0$$
$$\therefore \theta_1 + \theta_2 + \theta_4 + 2\pi - \theta_3 - \theta_5 - \theta_6 = 0. \tag{3.29}$$

Substituting (3.16), (3.17), (3.23), (3.24), (3.25), and (3.26) into (3.29) yields:

$$v_i^* = \frac{{d_M}^2}{2\left(d_M - 1\right)} V_{dc1}. \tag{3.30}$$

Substituting (3.30) into (3.23) and (3.24) yields:

$$\theta_2 = \pi\left(-\frac{d_M}{2} + \frac{1}{2}\right) \tag{3.31}$$
$$\theta_5 = \pi\left(\frac{d_M}{2} + \frac{3}{2}\right). \tag{3.32}$$

Similarly, substituting (3.30) into (3.25) and (3.26) yields:

$$\theta_3 = \pi\left(\frac{d_M}{2} + \frac{1}{2}\right) \tag{3.33}$$
$$\theta_4 = \pi\left(-\frac{d_M}{2} + \frac{3}{2}\right). \tag{3.34}$$

Based on (3.16), (3.17), (3.31), (3.32), (3.33), and (3.34), the relationships $\theta_1 \leq \theta_3$, $\theta_2 \leq \theta_3$, $\theta_4 \leq \theta_6$, and $\theta_5 \leq \theta_6$ always hold in the range $0 \leq d_M < 0.5$, which validates the fourth assumption.

Further, the validity of the assumptions that d_{A1} intersects $\mathrm{tri_M}$ at θ_2 and θ_5 (the second assumption), while d_{A2} intersects $\mathrm{tri_M}$ at θ_3 and θ_4 (the third assumption), should be confirmed. Substituting (3.30) into (3.21) and (3.22) yields:

$$d_{A1} = \begin{cases} 1 & (0 \leq \theta < \theta_1, \theta_6 < \theta \leq 2\pi) \\ -\frac{d_M}{2} + \frac{1}{2} & (\theta_1 \leq \theta \leq \theta_6) \end{cases} \tag{3.35}$$

$$d_{A2} = \begin{cases} 0 & (0 \leq \theta < \theta_1, \theta_6 < \theta \leq 2\pi) \\ \frac{d_M}{2} + \frac{1}{2} & (\theta_1 \leq \theta \leq \theta_6) \end{cases}, \tag{3.36}$$

where the values of d_{A1} and d_{A2} within the range of $(0 \leq \theta < \theta_1, \theta_6 < \theta \leq 2\pi)$ are modified due to the normalization. From Fig. 3.5, the values of tri_M at θ_1 and θ_6 correspond to d_M. Meanwhile, the values of d_{A1} at θ_1 and θ_6 are obtained from (3.35) as $-\frac{d_M}{2} + \frac{1}{2}$, which only gives higher value than d_M in the range of $0 \leq d_M < 0.33$. This signifies that the phase θ_2 that satisfies $\theta_2 \geq \theta_1$ and the phase θ_5 that satisfies $\theta_5 \leq \theta_6$ only exist for d_M in the range of $0 \leq d_M < 0.33$. On the contrary, $-\frac{d_M}{2} + \frac{1}{2}$ gives lower value than d_M in the range of $0.33 \leq d_M < 0.5$, which signifies that the phases θ_2 and θ_5 do not exist within the range. Subsequently, the values of d_{A2} at θ_1 and θ_6 are obtained from (3.36) as $\frac{d_M}{2} + \frac{1}{2}$, which always gives higher value than d_M in the range of $0 \leq d_M < 0.5$. This signifies that the phase θ_3 that satisfies $\theta_3 \geq \theta_1$ and the phase θ_4 that satisfies $\theta_4 \leq \theta_6$ always exist for d_M in the range of $0 \leq d_M < 0.5$. As such, d_{A2} invariably intersects tri_M at θ_3 and θ_4. Considering these results, the following analysis on the switching-ripple current will be done separately for d_M in the range of $0 \leq d_M < 0.33$ and $0.33 \leq d_M < 0.5$.

3.4.2.1 When $0 \leq d_M < 0.33$

Based on KVL (kirchhoff's voltage law), (3.18), (3.27), while also applying $V_C = \frac{V_{dc1}}{2}$, the inductor voltage, v_L, can be determined as:

$$
\begin{aligned}
v_L &= v_M - v_A - V_{dc2} \\
&= \begin{cases}
0.5V_{dc1} - V_{dc2} & (0 \leq \theta \leq \theta_1) \\
-V_{dc2} & (\theta_1 < \theta \leq \theta_2) \\
0.5V_{dc1} - V_{dc2} & (\theta_2 < \theta \leq \theta_3) \\
-V_{dc2} & (\theta_3 < \theta \leq \theta_4) \\
0.5V_{dc1} - V_{dc2} & (\theta_4 < \theta \leq \theta_5) \\
-V_{dc2} & (\theta_5 < \theta \leq \theta_6) \\
0.5V_{dc1} - V_{dc2} & (\theta_6 < \theta \leq 2\pi)
\end{cases} .
\end{aligned} \tag{3.37}
$$

From (3.37), given that the relationship $d_M = \frac{V_{dc2}}{V_{dc1}} < 0.5$ holds, the following trends hold for the inductor current, i_L:

- i_L rises with the rate of $0.5V_{dc1} - V_{dc2}$ within the range of $0 \leq \theta \leq \theta_1$ $(= I_{rise1})$, $\theta_2 < \theta \leq \theta_3$ $(= I_{rise2})$, $\theta_4 < \theta \leq \theta_5$ $(= I_{rise3})$, and $\theta_6 < \theta \leq 2\pi$ $(= I_{rise4})$.

- i_L drops with the rate of $-V_{dc2}$ within the range of $\theta_1 < \theta \leq \theta_2$ $(= I_{drop1})$, $\theta_3 < \theta \leq \theta_4$ $(= I_{drop2})$, and $\theta_5 < \theta \leq \theta_6$ $(= I_{drop3})$.

Further, the rising and dropping rates remain consistent under steady state. From (3.16) and (3.37), I_{rise1} is given by:

$$I_{rise1} = \frac{1}{\omega L}\int_0^{\theta_1} (0.5V_{dc1} - V_{dc2})\, d\theta \;= \frac{V_{dc1}}{2f_{SM}L}\frac{(1-2d_M)\, d_M}{2}. \tag{3.38}$$

From (3.16), (3.31), and (3.37), I_{drop1} is given by:

$$I_{drop1} = -\frac{1}{\omega L}\int_{\theta_1}^{\theta_2} (-V_{dc2})\, d\theta \;= \frac{V_{dc1}}{2f_{SM}L}\frac{(1-3d_M)\, d_M}{2}. \tag{3.39}$$

From (3.31), (3.33), and (3.37), I_{rise2} is given by:

$$I_{rise2} = \frac{1}{\omega L}\int_{\theta_2}^{\theta_3} (0.5V_{dc1} - V_{dc2})\, d\theta \;= \frac{V_{dc1}}{2f_{SM}L}\frac{(1-2d_M)\, d_M}{2}. \tag{3.40}$$

From (3.33), (3.34), and (3.37), I_{drop2} is given by:

$$I_{drop2} = -\frac{1}{\omega L}\int_{\theta_3}^{\theta_4} (-V_{dc2})\, d\theta \;= \frac{V_{dc1}}{2f_{SM}L}(1-d_M)\, d_M. \tag{3.41}$$

From (3.32), (3.34), and (3.37), I_{rise3} is given by:

$$I_{rise3} = \frac{1}{\omega L}\int_{\theta_4}^{\theta_5} (0.5V_{dc1} - V_{dc2})\, d\theta \;= \frac{V_{dc1}}{2f_{SM}L}\frac{(1-2d_M)\, d_M}{2}. \tag{3.42}$$

From (3.17), (3.32), and (3.37), I_{drop3} is given by:

$$I_{drop3} = -\frac{1}{\omega L}\int_{\theta_5}^{\theta_6} (-V_{dc2})\, d\theta \;= \frac{V_{dc1}}{2f_{SM}L}\frac{(1-3d_M)\, d_M}{2}. \tag{3.43}$$

From (3.17), and (3.37), I_{rise4} is given by:

$$I_{rise4} = \frac{1}{\omega L}\int_{\theta_6}^{2\pi} (0.5V_{dc1} - V_{dc2})\, d\theta \;= \frac{V_{dc1}}{2f_{SM}L}\frac{(1-2d_M)\, d_M}{2}. \tag{3.44}$$

Based on (3.38) to (3.44), the relationship $I_{drop2} > I_{rise1} = I_{rise2} = I_{rise3} = I_{rise4} > I_{drop1} = I_{drop3}$ always holds for d_M in the range of $0 < d_M < 0.33$. As such, the peak-to-

peak ripple current, I_{ripple}, in the given range is determined as:

$$I_{ripple} = \frac{V_{dc1}}{f_{SM}L}\left(1 - d_M\right)\frac{d_M}{2}. \tag{3.45}$$

3.4.2.2 When $0.33 \leq d_M < 0.5$

As has been explained before, the intersections between d_{A1} and tri_M (i.e., θ_2 and θ_5) do not exist for d_M in the range of $0.33 \leq d_M < 0.5$. Consequently, v_A that is given by (3.27) should be modified into:

$$v_A = \begin{cases} V_C & (0 \leq \theta \leq \theta_1) \\ -V_C & (\theta_1 < \theta \leq \theta_3) \\ 0 & (\theta_3 < \theta \leq \theta_4) \\ -V_C & (\theta_4 < \theta \leq \theta_6) \\ V_C & (\theta_6 < \theta \leq 2\pi) \end{cases}. \tag{3.46}$$

It should be noted that the change in v_A, due to the nonexistence of θ_2 and θ_5, will subsequently change the value of v_i^*. Substituting (3.16), (3.17), (3.25), and (3.26) into (3.46) yields:

$$v_i^* = \frac{\left(2d_M - 1\right)^2}{2\left(d_M - 1\right)}V_{dc1}. \tag{3.47}$$

Substituting (3.47) into (3.25) and (3.26) yields:

$$\theta_3 = 2\pi d_M \tag{3.48}$$

$$\theta_4 = \pi\left(2 - 2d_M\right). \tag{3.49}$$

Based on (3.16), (3.17), (3.48), and (3.49), the relationships $\theta_3 > \theta_1$ and $\theta_4 < \theta_6$ always hold for d_M in the range of $0.33 \leq d_M < 0.5$.

Based on KVL, (3.18), and (3.46), while also applying $V_C = \frac{V_{dc1}}{2}$, v_L can be determined

as:

$$v_L = \begin{cases} 0.5V_{dc1} - V_{dc2} & (0 \leq \theta \leq \theta_1) \\ 0.5V_{dc1} - V_{dc2} & (\theta_1 < \theta \leq \theta_3) \\ -V_{dc2} & (\theta_3 < \theta \leq \theta_4) \\ 0.5V_{dc1} - V_{dc2} & (\theta_4 < \theta \leq \theta_6) \\ 0.5V_{dc1} - V_{dc2} & (\theta_6 < \theta \leq 2\pi) \end{cases} . \tag{3.50}$$

From (3.50), the following trends hold in i_L:

- i_L rises with the rate of $0.5V_{dc1} - V_{dc2}$ within the range of $(0 \leq \theta \leq \theta_3)$.
- i_L drops with the rate of $-V_{dc2}$ within the range of $(\theta_3 < \theta \leq \theta_4)$.

Further, the rising and dropping rates remain consistent under steady state. Since i_L continuously rise from θ_4 until $2\pi + \theta_3$, the I_{ripple} for d_M in the range of $0.33 \leq d_M < 0.5$ can be determined as:

$$I_{ripple} = \frac{1}{\omega L} \int_{\theta_4}^{2\pi+\theta_3} (0.5V_{dc1} - V_{dc2})\, d\theta \; = \frac{V_{dc1}}{f_{SM} L} (1 - 2d_M)\, d_M. \tag{3.51}$$

3.4.3 When $0.5 \leq d_M \leq 1$

Based on Fig. 3.6, where the example of the ideal voltage and current waveforms of the BCSAC when $d_M = 0.75$ is shown, the following assumptions are considered:

- θ_1 and θ_6 are the intersection points between tri_M and d_{A2}.
- θ_2 and θ_5 are the intersection points between tri_M and d_{A1}.
- θ_3 and θ_4 are the intersection points between tri_M and d_M.
- The relationships $\theta_1 \leq \theta_3$, $\theta_2 \leq \theta_3$, $\theta_4 \leq \theta_6$, and $\theta_5 \leq \theta_6$ hold.

Based on Fig. 3.6, θ_3 and θ_4 can be determined as:

$$\theta_3 = \pi d_M \tag{3.52}$$

$$\theta_4 = 2\pi - \pi d_M, \tag{3.53}$$

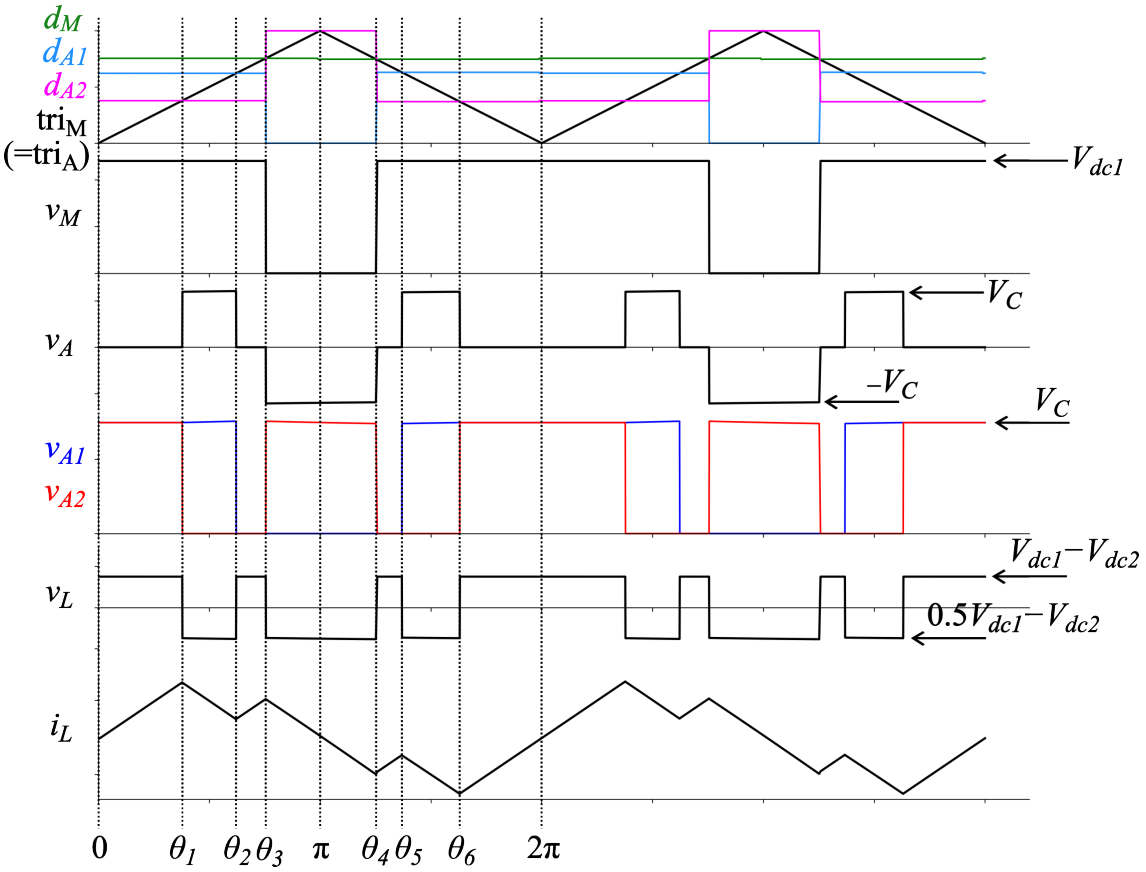

Figure 3.6: Ideal voltage and current waveforms of the BCSAC when $d_M = 0.75$.

where the relationship $\theta_3 \leq \theta_4$ always holds. Based on (3.1), v_M is given by:

$$v_M = \begin{cases} V_{dc1} & (0 \leq \theta \leq \theta_3, \theta_4 \leq \theta \leq 2\pi) \\ 0 & (\theta_3 < \theta < \theta_4) \end{cases}. \tag{3.54}$$

Based on (3.7), (3.14), and (3.15), while also applying $V_C = \frac{V_{dc1}}{2}$, the duty ratios d_{A1} and d_{A2} that have been normalized (i.e., $0 \leq d_{A1} \leq 1$ and $0 \leq d_{A2} \leq 1$) are given as:

$$d_{A1} = \begin{cases} -\frac{v_i^*}{V_{dc1}} + \frac{0.5}{d_M} & (0 \leq \theta \leq \theta_3, \theta_4 \leq \theta \leq 2\pi) \\ -\frac{v_i^*}{V_{dc1}} & (\theta_3 < \theta < \theta_4) \end{cases} \tag{3.55}$$

$$d_{A2} = \begin{cases} \frac{v_i^*}{V_{dc1}} + 1 - \frac{0.5}{d_M} & (0 \leq \theta \leq \theta_3, \theta_4 \leq \theta \leq 2\pi) \\ \frac{v_i^*}{V_{dc1}} + 1 & (\theta_3 < \theta < \theta_4) \end{cases}. \tag{3.56}$$

Based on Fig. 3.6 and (3.55), θ_2 and θ_5 can be determined as:

$$\theta_2 = \pi\left(-\frac{v_i^*}{V_{dc1}} + \frac{0.5}{d_M}\right) \tag{3.57}$$

$$\theta_5 = 2\pi - \pi\left(-\frac{v_i^*}{V_{dc1}} + \frac{0.5}{d_M}\right). \tag{3.58}$$

Meanwhile, based on Fig. 3.6 and (3.56), θ_1 and θ_6 can be determined as:

$$\theta_1 = \pi\left(\frac{v_i^*}{V_{dc1}} - \frac{0.5}{d_M} + 1\right) \tag{3.59}$$

$$\theta_6 = 2\pi - \pi\left(\frac{v_i^*}{V_{dc1}} - \frac{0.5}{d_M} + 1\right). \tag{3.60}$$

The value of v_A from θ_1 through θ_6 is given by:

$$v_A = \begin{cases} 0 & (0 \le \theta \le \theta_1) \\ V_C & (\theta_1 < \theta \le \theta_2) \\ 0 & (\theta_2 < \theta \le \theta_3) \\ -V_C & (\theta_3 < \theta \le \theta_4) \\ 0 & (\theta_4 < \theta \le \theta_5) \\ V_C & (\theta_5 < \theta \le \theta_6) \\ 0 & (\theta_6 < \theta \le 2\pi) \end{cases}, \tag{3.61}$$

while its average value in one switching period is zero. Similarly, considering (3.52), (3.53), and (3.57) to (3.61) the voltage command v_i^* can be determined as:

$$v_i^* = \frac{(d_M - 1)^2}{2d_M} V_{dc1}. \tag{3.62}$$

Substituting (3.62) into (3.57) and (3.58) yields:

$$\theta_2 = \pi\left(-\frac{d_M}{2} + 1\right) \tag{3.63}$$

$$\theta_5 = \pi\left(\frac{d_M}{2} + 1\right). \tag{3.64}$$

Substituting (3.62) into (3.59) and (3.60) yields:

$$\theta_1 = \pi \frac{d_M}{2} \tag{3.65}$$

$$\theta_6 = \pi \left(-\frac{d_M}{2} + 2 \right). \tag{3.66}$$

Based on (3.52), (3.53), and (3.63) to (3.66), the relationships $\theta_1 \leq \theta_3$, $\theta_2 \leq \theta_3$, $\theta_4 \leq \theta_6$, and $\theta_5 \leq \theta_6$ always hold in the range $0.5 \leq d_M \leq 1$, which validates the fourth assumption.

Further, the validity of the assumptions that d_{A2} intersects $\mathrm{tri_M}$ at θ_1 and θ_6 (the first assumption), while d_{A1} intersects $\mathrm{tri_M}$ at θ_2 and θ_5 (the second assumption), should be confirmed. Substituting (3.62) into (3.55) and (3.56) yields:

$$d_{A1} = \begin{cases} -\frac{d_M}{2} + 1 & (0 \leq \theta \leq \theta_3, \theta_4 \leq \theta \leq 2\pi) \\ 0 & (\theta_3 < \theta < \theta_4) \end{cases} \tag{3.67}$$

$$d_{A2} = \begin{cases} \frac{d_M}{2} & (0 \leq \theta \leq \theta_3, \theta_4 \leq \theta \leq 2\pi) \\ 1 & (\theta_3 < \theta < \theta_4) \end{cases}, \tag{3.68}$$

where the values of d_{A1} and d_{A2} within the range of $\theta_3 < \theta < \theta_4$ are modified due to the normalization. From Fig. 3.6, the values of $\mathrm{tri_M}$ at θ_3 and θ_4 correspond to d_M. Meanwhile, the values of d_{A1} at θ_3 and θ_4 are obtained from (3.67) as $-\frac{d_M}{2} + 1$, which gives lower value than d_M in the range of $0.67 \leq d_M \leq 1$. This signifies that the phase θ_2 that satisfies $\theta_2 \leq \theta_3$ and the phase θ_5 that satisfies $\theta_5 \geq \theta_4$ only exist for d_M in the range of $0.67 \leq d_M \leq 1$. On the contrary, $-\frac{d_M}{2} + 1$ gives higher value than d_M in the range of $0.5 \leq d_M < 0.67$, which signifies that the phases θ_2 and θ_5 do not exist within the range. Subsequently, the values of d_{A2} at θ_3 and θ_4 are obtained from (3.68) as $-\frac{d_M}{2}$, which always gives higher value than d_M in the range of $0.5 \leq d_M \leq 1$. This signifies that the phase θ_1 and θ_6 that satisfies $\theta_1 \leq \theta_3$ and the phase θ_6 that satisfies $\theta_6 \geq \theta_4$ always exist for d_M in the range of $0.5 \leq d_M \leq 1$. As such, d_{A2} invariably intersects $\mathrm{tri_M}$ at θ_1 and θ_6. Considering these results, the following analysis on the switching-ripple current will be done separately for d_M in the range of $0.5 \leq d_M < 0.67$ and $0.67 \leq d_M \leq 1$.

3.4.3.1 When $0.67 \leq d_M \leq 1$

Based on KVL, (3.54), (3.61), while also applying $V_C = \frac{V_{dc1}}{2}$, the inductor voltage, v_L, can be determined as:

$$v_L = \begin{cases} V_{dc1} - V_{dc2} & (0 \leq \theta \leq \theta_1) \\ 0.5V_{dc1} - V_{dc2} & (\theta_1 < \theta \leq \theta_2) \\ V_{dc1} - V_{dc2} & (\theta_2 < \theta \leq \theta_3) \\ 0.5V_{dc1} - V_{dc2} & (\theta_3 < \theta \leq \theta_4) \\ V_{dc1} - V_{dc2} & (\theta_4 < \theta \leq \theta_5) \\ 0.5V_{dc1} - V_{dc2} & (\theta_5 < \theta \leq \theta_6) \\ V_{dc1} - V_{dc2} & (\theta_6 < \theta \leq 2\pi) \end{cases} . \tag{3.69}$$

From (3.69), given that the relationship $d_M = \frac{V_{dc2}}{V_{dc1}} \geq 0.5$ holds, the following trends hold for the inductor current, i_L:

- i_L rises with the rate of $V_{dc1} - V_{dc2}$ within the range of $0 \leq \theta \leq \theta_1$ $(= I_{rise1})$, $\theta_2 < \theta \leq \theta_3$ $(= I_{rise2})$, $\theta_4 < \theta \leq \theta_5$ $(= I_{rise3})$, and $\theta_6 < \theta \leq 2\pi$ $(= I_{rise4})$.

- i_L drops with the rate of $0.5V_{dc1} - V_{dc2}$ within the range of $\theta_1 < \theta \leq \theta_2$ $(= I_{drop1})$, $\theta_3 < \theta \leq \theta_4$ $(= I_{drop2})$, and $\theta_5 < \theta \leq \theta_6$ $(= I_{drop3})$.

Further, the rising and dropping rates remain consistent under steady state. Through similar processes done in the previous section, the I_{ripple} for d_M in the range of $0.67 \leq d_M \leq 1$ can be determined as:

$$I_{ripple} = \frac{1}{\omega L} \int_{\theta_6}^{2\pi+\theta_1} (V_{dc1} - V_{dc2})\, d\theta \; = \frac{V_{dc1}}{f_{SM} L} (1 - d_M) \frac{d_M}{2}. \tag{3.70}$$

3.4.3.2 When $0.5 \leq d_M < 0.67$

As has been explained before, the intersections between d_{A1} and tri_M (i.e., θ_2 and θ_5) do not exist for d_M in the range of $0.5 \leq d_M < 0.67$. Consequently, v_A that is given by (3.61)

is modified into:

$$v_A = \begin{cases} 0 & (0 \leq \theta \leq \theta_1) \\ V_C & (\theta_1 < \theta \leq \theta_3) \\ -V_C & (\theta_3 < \theta \leq \theta_4) \\ V_C & (\theta_4 < \theta \leq \theta_6) \\ 0 & (\theta_6 < \theta \leq 2\pi) \end{cases}. \tag{3.71}$$

Substituting (3.52), (3.53), (3.65), and (3.66) into (3.71) yields:

$$v_i^* = \frac{(2d_M - 1)^2}{2d_M} V_{dc1}. \tag{3.72}$$

Substituting (3.72) into (3.65) and (3.66) yields:

$$\theta_1 = \pi\left(-1 + 2d_M\right) \tag{3.73}$$

$$\theta_6 = \pi\left(3 - 2d_M\right). \tag{3.74}$$

Based on (3.52), (3.53), (3.73), and (3.74), the relationships $\theta_1 < \theta_3$ and $\theta_6 > \theta_4$ always hold for d_M in the range of $0.5 \leq d_M < 0.67$.

Based on KVL, (3.54), and (3.71), while also applying $V_C = \frac{V_{dc1}}{2}$, v_L can be determined as:

$$v_L = \begin{cases} V_{dc1} - V_{dc2} & (0 \leq \theta \leq \theta_1) \\ 0.5V_{dc1} - V_{dc2} & (\theta_1 < \theta \leq \theta_3) \\ 0.5V_{dc1} - V_{dc2} & (\theta_3 < \theta \leq \theta_4) \\ 0.5V_{dc1} - V_{dc2} & (\theta_4 < \theta \leq \theta_6) \\ V_{dc1} - V_{dc2} & (\theta_6 < \theta \leq 2\pi) \end{cases}. \tag{3.75}$$

From (3.75), the following trends hold in i_L:

- i_L rises with the rate of $V_{dc1} - V_{dc2}$ within the range of $(0 \leq \theta \leq \theta_1)$ and $(\theta_6 < \theta \leq 2\pi)$.
- i_L drops with the rate of $0.5V_{dc1} - V_{dc2}$ within the range of $(\theta_1 < \theta \leq \theta_6)$.

Further, the rising and dropping rates remain consistent under steady state. Since i_L continuously drops from θ_1 until θ_6, the I_{ripple} for d_M in the range of $0.5 \leq d_M < 0.67$ can

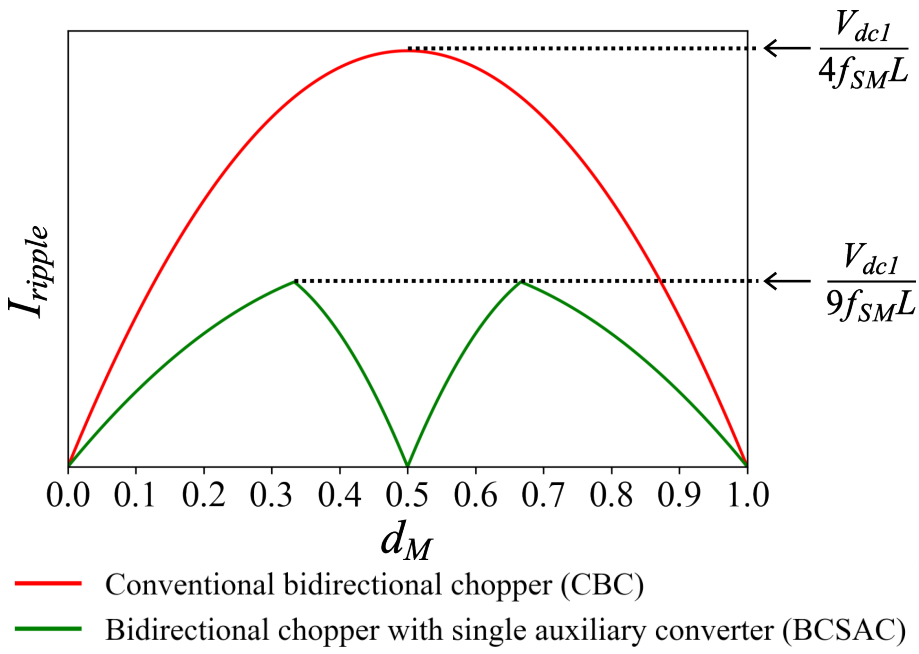

Figure 3.7: Theoretical results for the switching-ripple current of the BCSAC and CBC.

be determined as:

$$I_{ripple} = -\frac{1}{\omega L}\int_{\theta_1}^{\theta_6}(0.5V_{dc1} - V_{dc2})\,d\theta \;= \frac{V_{dc1}}{f_{SM}L}(2d_M - 1)(1 - d_M). \tag{3.76}$$

Based on (3.45), (3.51), (3.70), and (3.76), the maximum value for I_{ripple} of the BCSAC is obtained when $d_M = \frac{1}{3}$ and $d_M = \frac{2}{3}$, which is equivalent to:

$$(I_{ripple})_{max} = \frac{V_{dc1}}{9f_{SM}L}. \tag{3.77}$$

Meanwhile, the switching-ripple current of the CBC can be determined as:

$$I_{ripple} = \frac{V_{dc1}}{f_{SM}L}(1 - d_M)\,d_M. \tag{3.78}$$

Based on (3.78), the $(I_{ripple})_{max}$ of the CBC is obtained when $d_M = \frac{1}{2}$ as:

$$(I_{ripple})_{max} = \frac{V_{dc1}}{4f_{SM}L}. \tag{3.79}$$

Based on (3.77) and (3.79), the BCSAC is able to reduce the switching-ripple current to $\frac{4}{9}$ of that produced by the CBC. Fig. 3.7 shows the theoretical results for the switching-ripple current of the BCSAC (green line) and CBC (red line) under d_M in the range of

$0 \leq d_M \leq 1$. It shows that there is a symmetry in the switching-ripple current of the BCSAC between that when d_M in the range of $0 \leq d_M < 0.5$ and $0.5 \leq d_M \leq 1$. Further, the advantage of the BCSAC over the CBC is especially apparent when the operating duty ratio is around $d_M = 0.5$, where the relationship $(v_A)_{ac} = (v_M)_{ac}$ holds, which eliminates the frequency component f_{SM} in the inductor current.

3.5 Comparison with Other Topologies

The objective of the BCSAC is to reduce the inductor volume without a significant power loss compensation. To evaluate the performance and efficacy of the BCSAC, theoretical comparisons on the inductor volume, chopper volume and mass, power loss, and efficiency with the CBC, TLFC, and BCAC with three cells are carried out. The circuit configurations of the CBC, TLFC, and BCAC are given in Fig. 2.1, Fig. 2.2, and Fig. 2.3, respectively. However, cost comparison is beyond the scope of this study, and should be left for future work.

3.5.1 Inductor Volume

3.5.1.1 Assumptions Used in the Comparison

Theoretical analysis on the inductor volume is conducted for the four choppers based on the method described in [101], [104]. The following assumptions are applied in the analysis:

- Air-core inductors are used, where brooks coil geometry is adopted.
- The inductors operate under a maximum current capacity, I_{max}, of 1000 A and a maximum current density, J_{max}, of 2×10^6 A/m^2.
- Under the same switching frequency, the same amount of ripple current is produced by all choppers.

Air-core inductors are employed because they are widely used in choppers for electric railways, due to their characteristics that show better size reduction in higher operating frequencies, non-existent core saturation, and produce no iron loss [105]–[109]. Further, the inductors is assumed to obey the Brooks coil geometry, which gives the highest possible inductance value for a given wire length [104]. Finally, all choppers should produce the

same amount of ripple current under the same switching frequency to do a fair comparison, from which the inductance value for each chopper can be determined.

3.5.1.2 Comparison

The comparison of the calculated parameters of the air-core inductors for all four choppers are summarized in Table 3.1. These parameters are calculated based on the set values of the I_{max} and J_{max} (the second assumption) using similar methods as those described in [101], [104], while the parameter definitions and detailed calculation processes are provided in Appendix B.1. Considering the third assumption held in this analysis and the theoretical results of the switching-ripple current analysis, the inductance value for each chopper is set to $L = 0.9\,\text{mH}$ for the CBC, $L = 0.45\,\text{mH}$ for the TLFC, $L = 0.015\,\text{mH}$ for the BCAC with three cells, and $L = 0.4\,\text{mH}$ for the BCSAC. Further, based on the results shown in Table 3.1, the BCSAC enables the utilizations of an inductor with smaller volume ($40.73\,\text{dm}^3$) compared to the CBC ($66.09\,\text{dm}^3$) and TLFC ($45.50\,\text{dm}^3$) under the same frequency. This translates to inductor volume reductions of around 38.4 % and 10.5 % from the CBC and TLFC, respectively. However, the volume-reduction achieved by the BCSAC is still lower than that achieved by the BCAC, where the required inductor volume is $7.26\,\text{dm}^3$.

Table 3.1: Parameters used in the inductor volume analysis

Parameter	**CBC**	**TLFC**	**BCAC**	**BCSAC**
$\boldsymbol{L}$	0.9 mH	0.45 mH	0.015 mH	0.4 mH
$\boldsymbol{a}$	27.6 cm	25.6 cm	17.2 cm	23.8 cm
$\boldsymbol{b}$	15.6 cm	13 cm	5.2 cm	13 cm
$\boldsymbol{c}$	18.2 cm	15.6 cm	7.8 cm	15.6 cm
$\boldsymbol{d}$	25.23 mm	25.23 mm	25.23 mm	25.23 mm
d_i	26 mm	26 mm	26 mm	26 mm
n_t	6	5	2	5
n_l	7	6	3	6
n	42	30	6	30
v_L	$66.09\,\text{dm}^3$	$45.50\,\text{dm}^3$	$7.26\,\text{dm}^3$	$40.73\,\text{dm}^3$

3.5.2 Chopper Volume and Mass

3.5.2.1 Assumptions Used in the Comparison

Theoretical analysis on the chopper total volume is conducted for the four choppers under the following assumptions:

- The components of the chopper are consisted of the inductor, capacitor, and power devices along with the cooling systems in both the main and auxiliary converters.
- The DC film capacitor E50.N15-323NT0 (32 µF, I_{max} = 50 A) from Electronicon is used, where a parallel connection of twenty capacitors is used in the auxiliary converter, giving an equivalent capacitance value of 0.64 mF.
- Air-cooling system with heatsink is applied, where it is designed based on the CSPI (cooling system performance index) that is set to 7.0 and its density is the same as the density of aluminum (i.e., 2.7 g/cm^3).
- Junction temperature, T_j, is 125°C, while the ambient temperature, T_a, is 40°C.
- The power devices used in the main and auxiliary converters have the same mass.

DC film capacitor is chosen since it is widely used in electric railways due to its large capacity, long service life, and low impedance [110]–[112]. Further, a parallel connection of twenty capacitors is used in the auxiliary converter to account for the assumed I_{max} given in Chapter 3.5.1 (I_{max} = 1000 A). Air-cooling system is applied since it is commonly used in electric railways, due to their simple design and cost-effective performances [113]–[115]. Further, the CSPI indicates the cooling performance per unit volume of the system, where higher value reflects higher performances. The CSPI value is to 7.0 in the analysis [116]–[118].

3.5.2.2 Comparison

Theoretical analysis on the chopper total volume and mass is conducted to confirm the significance of the inductor volume reduction achieved by the BCSAC related to the additional components required in the auxiliary converter. The volume breakdown of the four choppers is shown in Fig. 3.8a. The volumes of the capacitor and power devices are estimated based on the dimensions provided in [119]–[121]. Meanwhile, the volume of the cooling system is calculated based on its CSPI value using the methods described in [101], [122], while the detailed calculation processes are provided in Appendix B.2. Based on Fig. 3.8a, the BCSAC has a slightly higher volume (77.21 dm^3) than the CBC (76.14 dm^3) and TLFC (77.04 dm^3). The additional volume mainly comes from the capacitor and cooling system attached to the auxiliary converter (17.02 dm^3 and 8.37 dm^3, respectively). On the other hand, the BCSAC is almost 20 % smaller than the BCAC (95.33 dm^3).

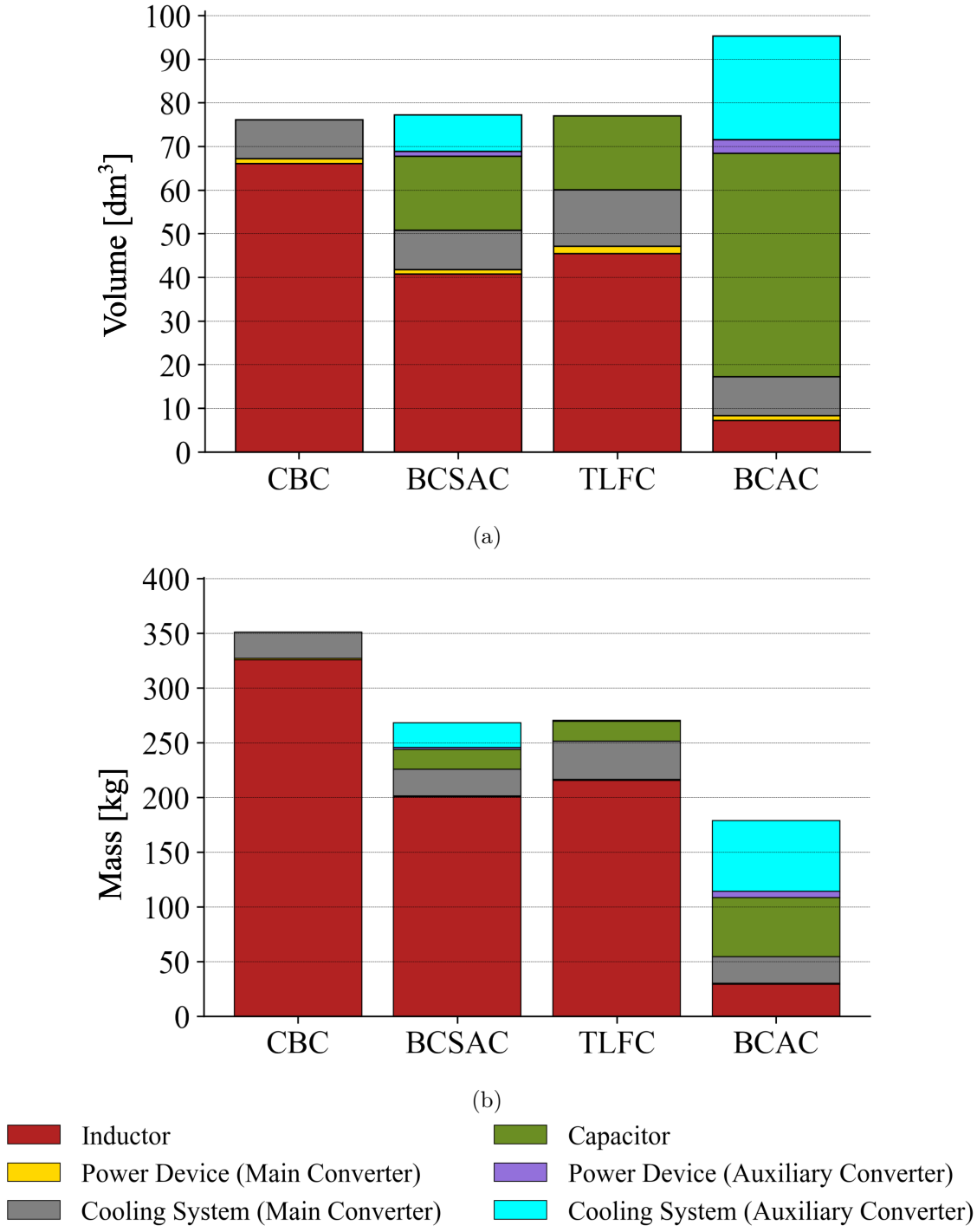

Figure 3.8: Breakdown of the four choppers: (a) Chopper volume, and (b) Chopper mass.

The mass breakdown of the four choppers is shown in Fig. 3.8b. The masses of the capacitor and power devices are provided in [119]–[121]. Meanwhile, the mass of the cooling system is calculated based on its volume and density. Based on Fig. 3.8b, the mass of the BCSAC (268.2 kg) is around 23.6 % lower than that of the CBC (351.06 kg), and 0.8 % lower than that of the TLFC (270.4 kg). However, the BCSAC is heavier than the BCAC (178.53 kg).

3.5.3 Power Loss and Efficiency

3.5.3.1 Assumptions Used in the Comparison

Theoretical analysis on the power loss and efficiency is conducted for the four choppers under the following assumptions:

- The deadtimes of the main and auxiliary converters are zero.
- The DC inductor current is positive and constant, while the DC-capacitor voltage is constant.
- The IGBT (insulated-gate bipolar transistor) power modules 1MBI1000UG-330 (Si-IGBT, 1-in-1, 3.3 kV) from Fuji Electric and CM1000DX-24T (Si-IGBT, 1-in-1, 1.2 kV) from Mitsubishi Electric are used.
- The conduction losses of the IGBT and the FWD (free-wheeling diode), the switching loss of the IGBT, the reverse recovery loss of the FWD, and the inductor loss are considered.

The IGBT power modules are selected based on the required voltage rating in real applications of the BCSAC. For the 1MBI1000UG-330 model, two modules are used in each of the CBC, the TLFC, and the main converters of both the BCAC and BCSAC. Meanwhile, for the CM1000DX-24T model, two modules are used in the TLFC, twelve modules are used in the three-cells auxiliary converter of the BCAC, and four modules are used in the full-bridge auxiliary converter of the BCSAC. The calculation for the losses utilize approximated values that are based on the specifications of the IGBT power modules that can be found in [119], [120]. The approximations data and the explanations on the calculation processes are given in Appendix C.

Table 3.2: Parameters used in the power loss and efficiency analysis

Parameter	Description	Value
ALL		
$\boldsymbol{P}$	Rated power	1.5 MW
$\boldsymbol{V_{dc1}}$	DC-voltage source 1 (high-voltage side)	1.5 kV
$\boldsymbol{V_{dc2}}$	DC-voltage source 2 (low-voltage side)	0.3 kV and 1.2 kV
$\boldsymbol{f}$	Switching frequency of the chopper	5 kHz
$\boldsymbol{f_{SM}}$	Switching frequency of the main converter	5 kHz
$\boldsymbol{f_{SA}}$	Switching frequency of the auxiliary converter	5 kHz
CBC		
$\boldsymbol{L}$	Inductance	0.9 mH
TLFC		
$\boldsymbol{L}$	Inductance	0.45 mH
$\boldsymbol{V_C}$	DC-capacitor voltage	0.75 kV
BCAC		
$\boldsymbol{L}$	Inductance	0.015 mH
$\boldsymbol{V_C}$	DC-capacitor voltage	0.45 kV
BCSAC		
$\boldsymbol{L}$	Inductance	0.4 mH
$\boldsymbol{V_C}$	DC-capacitor voltage	0.75 kV

3.5.3.2 Comparison

The parameters used in the power loss and efficiency analysis for all four choppers are summarized in Table 3.2. The rated power is set to $P = 1.5\,\text{MW}$ with $V_{dc1} = 1.5\,\text{kV}$, which is the typical DC voltage supply used for the electric railway systems in Japan [123]. Meanwhile, V_{dc2} is alternated between 0.3 and 1.2 kV to conduct the analysis under different values of d_M based on (3.13). All choppers operate under the same switching frequency at 5 kHz. It should be noted that for the TLFC, the equivalent switching frequency could be $2f_{TLFC}$, depending on the relationship between V_{dc1} and V_{dc2}. The inductance values are set to be the same as in Chapter 3.5.1. Finally, V_C is set to be half of V_{dc1} at $V_C = 0.75\,\text{kV}$ for the TLFC and BCSAC, while it set to $V_C = 0.45\,\text{kV}$ for the BCAC.

The power loss breakdowns of the four choppers under two different duty ratios (i.e., $d_M = 0.2$ and $d_M = 0.8$) are shown in Fig. 3.9. From Figs. 3.9a and 3.9b, the CBC loses around 7.8 kW of power in total, in average, for the maximum power rating under both d_M values, and it is spread almost evenly among the conduction loss (3.1 kW), switching loss (2.1 kW), and inductor loss (2.6 kW). From Figs. 3.9c and 3.9d, the total power loss of the TLFC is slightly higher at 8.8 kW, in average, where the majority comes from the conduction loss (5.3 kW), followed by the switching loss (1.8 kW) and the inductor loss

(1.7 kW). Meanwhile, from Figs. 3.9e and 3.9f, the BCAC produces a significantly higher loss (19.5 kW), in average, which is more than doubled those of the CBC and TLFC. Most of it comes from the additional auxiliary converter that is equipped with three cells (14.2 kW). However, the BCAC is able to reduce the inductor loss compared to the previous two topologies (0.2 kW). In comparison, from Figs. 3.9g and 3.9h, the BCSAC produces a total power loss of around 11.7 kW, which is significantly less than that of the BCAC, but still slightly higher than those of the CBC and the TLFC. The reason is that the loss produced by the auxiliary converter in the BCSAC (5 kW) is significantly less than that of the BCAC. In addition, the BCSAC produces lower inductor loss (1.6 kW) than the CBC and TLFC.

The efficiencies for all choppers are calculated based on the results of the power loss analysis and shown in Fig. 3.10, where red line indicates the CBC, blue line indicates the TLFC, brown line indicates the BCAC, and green line indicates the BCSAC. From Fig. 3.10a, the BCSAC is able to perform at around 97 %, in average, under $d_M = 0.2$. This is higher than the average efficiency of BCAC at 95 %, but lower than those of CBC and TLFC at 98 %. From Fig. 3.10b, the BCSAC is able to perform at around 99.2 %, in average, under $d_M = 0.8$. This is higher than the average efficiency of BCAC at 98.7 %, but lower than those of CBC and TLFC at 99.5 % and 99.4 %, respectively.

The comparison results between the four choppers are summarized in Table 3.3. Overall, there is a trade-off between the inductor volume, chopper dimensions, and the power loss (i.e., efficiency) of the BCSAC, compared to the other three topologies. More specifically, compared to the BCAC, the BCSAC is smaller in volume and able to produce significantly lower power loss, but it is heavier and achieves less reduction in the inductor volume. On the other hand, the BCSAC produces higher power loss compared to the CBC and TLFC. However, considering the reduction in the inductor volume that can be achieved by the BCSAC, the slightly lower efficiency to the CBC and TLFC is a minor issue. In addition, the mass reduction achieved by the BCSAC could reduce the energy required to move the vehicle, which could potentially give positive impact to the overall energy efficiency of the vehicle.

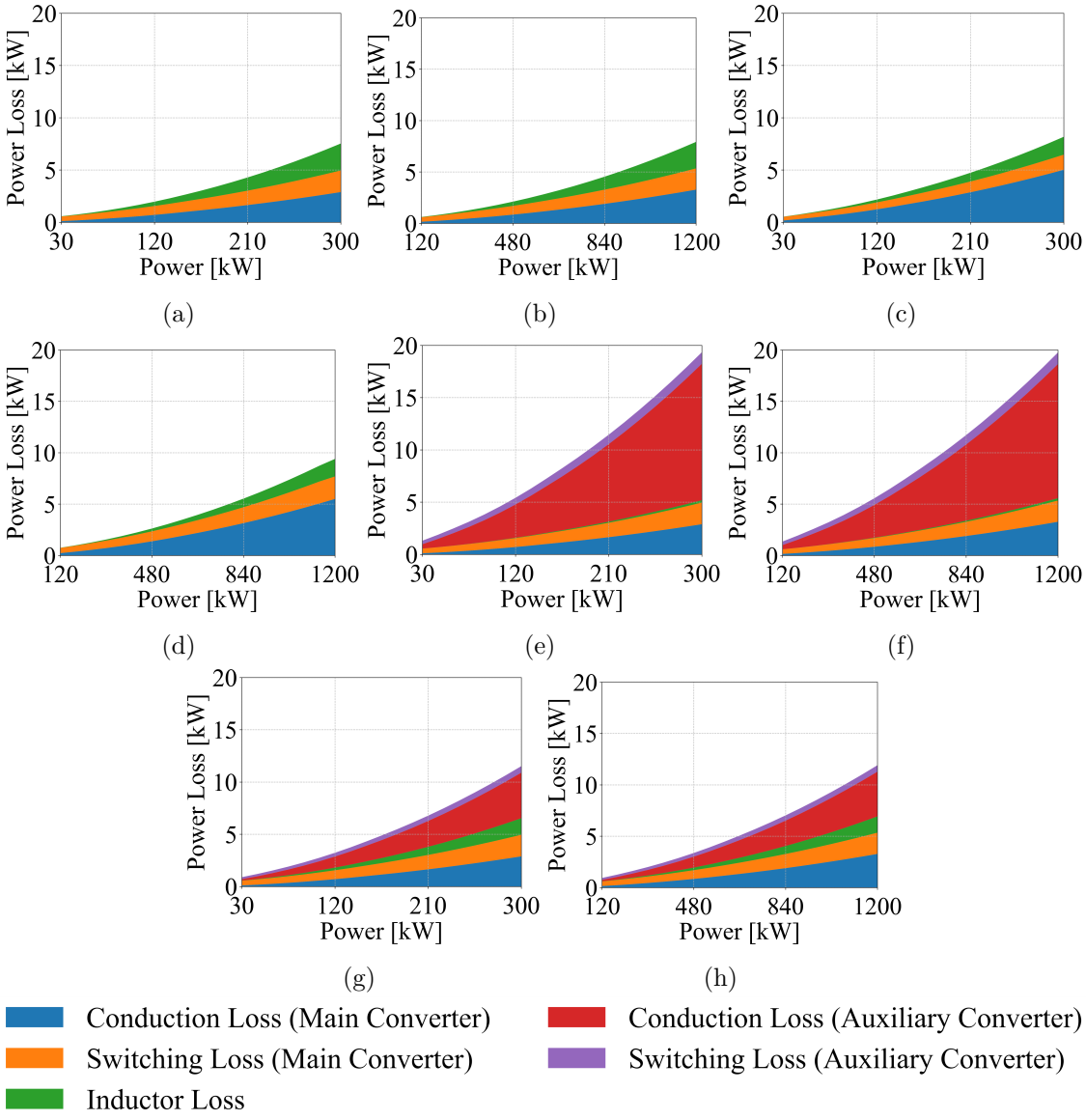

Figure 3.9: Loss breakdown of (a) CBC when $V_{dc2} = 0.3\,\text{kV}$, (b) CBC when $V_{dc2} = 1.2\,\text{kV}$, (c) TLFC when $V_{dc2} = 0.3\,\text{kV}$, (d) TLFC when $V_{dc2} = 1.2\,\text{kV}$, (e) BCAC when $V_{dc2} = 0.3\,\text{kV}$, (f) BCAC when $V_{dc2} = 1.2\,\text{kV}$, (g) BCSAC when $V_{dc2} = 0.3\,\text{kV}$, (h) BCSAC when $V_{dc2} = 1.2\,\text{kV}$.

Table 3.3: Comparison results between the BCSAC, CBC, TLFC, and BCAC

Comparison	**BCSAC**	**CBC**	**TLFC**	**BCAC**
Inductor volume	40.73 dm^3	66.09 dm^3	45.50 dm^3	7.26 dm^3
Chopper volume	77.21 dm^3	76.14 dm^3	77.04 dm^3	95.33 dm^3
Chopper mass	252.59 kg	342.99 kg	258.78 kg	149.01 kg
Power loss	11.7 kW	7.7 kW	8.8 kW	19.5 kW
Efficiency	96–99.3 %	97.2–99.6 %	97.4–99.5 %	94–99 %

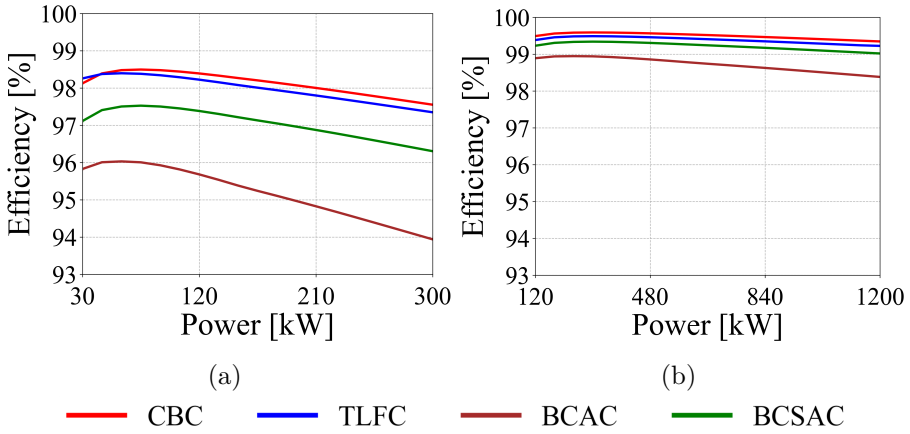

Figure 3.10: Efficiency of the four choppers when: (a) $V_{dc} = 0.3\,\text{kV}$ ($d_M = 0.2$), (b) $V_{dc} = 1.2\,\text{kV}$ ($d_M = 0.8$).

3.6 Experimental Results

To validate the result obtained from the theoretical analysis, as well as the operations and controls of the BCSAC, experiments are conducted using a down-scaled model in a controlled environment. This Chapter discusses the experimental results on the switching-ripple current, steady-state operations, and transient-state operations.

3.6.1 Experimental Configuration and Conditions

The 2 kW down-scaled model of the BCSAC used to conduct the experiments is shown in Fig. 3.11. The model is set as the following:

- The DC-voltage sources V_{dc1} and V_{dc2} are connected to either of DC-power supply KIKUSUI PAT160-50T or HEADSPRING biATLAS-5D525.
- The reference value for the DC-capacitor voltage is set to $V_C^* = 75\,\text{V}$.
- An air-core inductor with linear frequency characteristics and an inductance value of $L = 0.395\,\text{mH}$ is used, while the switching frequencies of the main and auxiliary converter are accordingly set to 5 kHz (i.e., $f_{SM} = f_{SA} = 5\,\text{kHz}$).
- The reference values for the inductor current can be alternately set to positive and negative values. Positive current means that the power direction is from V_{dc1} to V_{dc2}, while negative current means the opposite.
- The controls of the BCSAC are achieved using a combination of Texas Instru-

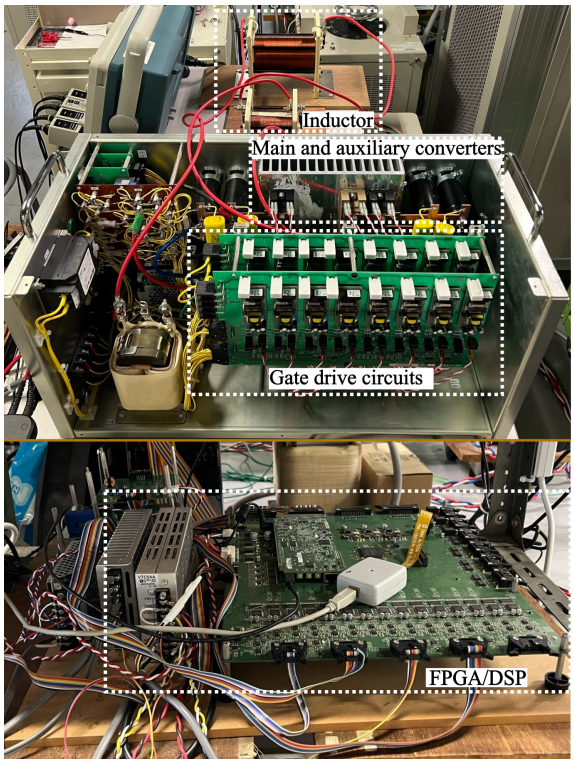

Figure 3.11: Experimental setup of the BCSAC using the down-scaled model.

ments TMS320C6678 as the DSP (digital signal processor) and Altera Cyclone IV E EP4CE30F29C7 as the FPGA (field-programmable gate array). The FPGA is used to generate the triangular carriers and to compare the duty ratios (i.e., d_M, d_{A1}, and d_{A2}) with the triangular carriers.

- The experimental waveforms are taken using Tektronix oscilloscope DPO4104B-L with a frequency band of 1 GHz. i_L is measured using the Tektronix current probe TCP0020 with a frequency band of 50 MHz, while v_M, v_A, v_L, and v_C are measured using the Tektronix high-voltage differential probes THDP0200 with a frequency band of 200 MHz.

Further, the following experiments are carried using the down-scaled model under the experimental parameters listed in Table 3.4:

1. Ripple current values (including those of the CBC) when $V_{dc1} = 150\,\text{V}$, $i_L^* = \pm 10\,\text{A}$, and v_C is initially charged to 75 V.

2. Steady-state operation when $V_{dc1} = 150\,\text{V}$, $V_{dc2} = 65\,\text{V}$, $i_L^* = 20\,\text{A}$, and v_C is initially charged to 75 V.

3. Steady-state operation when $V_{dc1} = 150\,\text{V}$, $V_{dc2} = 85\,\text{V}$, $i_L^* = -20\,\text{A}$, and v_C is initially charged to 75 V.

4. Transient behavior during initial charging of v_C from 0 V to 75 V.

5. Transient behavior during step change of V_{dc2} from 65 V to 75 V.

It should be noted that the down-scaled model used to conduct the experiments comes with several limitations that could affect the produced power loss, including parasitic effects, loss distributions, and devices characteristics [124]–[126]. Thus, experiments to verify power loss and efficiency of the BCSAC are not done in this paper, and should be deferred for future research.

Table 3.4: Parameters of the experiments

Parameter	Description	Value
$\boldsymbol{P}$	Rated power	2 kW
$\boldsymbol{V_{dc1}}$	DC-voltage source 1 (high-voltage side)	150 V
$\boldsymbol{L}$	Inductance	0.395 mH
$\boldsymbol{C}$	Capacitance	0.4 mF
$\boldsymbol{V_C^*}$	DC-capacitor voltage	75 V
$\boldsymbol{f_{SM}}$	Switching frequency of the main converter	5 kHz
$\boldsymbol{f_{SA}}$	Switching frequency of the auxiliary converter	5 kHz

3.6.2 Switching-Ripple Current Verification

The results of the theoretical switching-ripple current obtained from (3.45), (3.51), (3.70), (3.76), and (3.78), and the experimental switching-ripple current for the CBC and the BCSAC based on the values of d_M under positive and negative currents are given in Fig. 3.12. The theoretical and experimental switching-ripple currents of the CBC are illustrated by the red line and black crosses, respectively, while those of the BCSAC are illustrated by the green line and brown crosses, respectively. The experimental results are obtained under $V_{dc1} = 150\,\text{V}$ and v_C is initially charged to 75 V, while V_{dc2} is gradually changed from 30–140 V to alter the d_M. The reference values of the inductor current are set to $i_L^* = 10\,\text{A}$ in Fig. 3.12a and $i_L^* = -10\,\text{A}$ in Fig. 3.12b. Positive current implies that the current flows from the high-voltage side to the low-voltage side, while negative current implies that the current flows from the low-voltage side to the high-voltage side.

It can be seen from Fig. 3.12 that the experimental results agree well with the theoretical results for both choppers. Fig. 3.12a shows that the maximum experimental

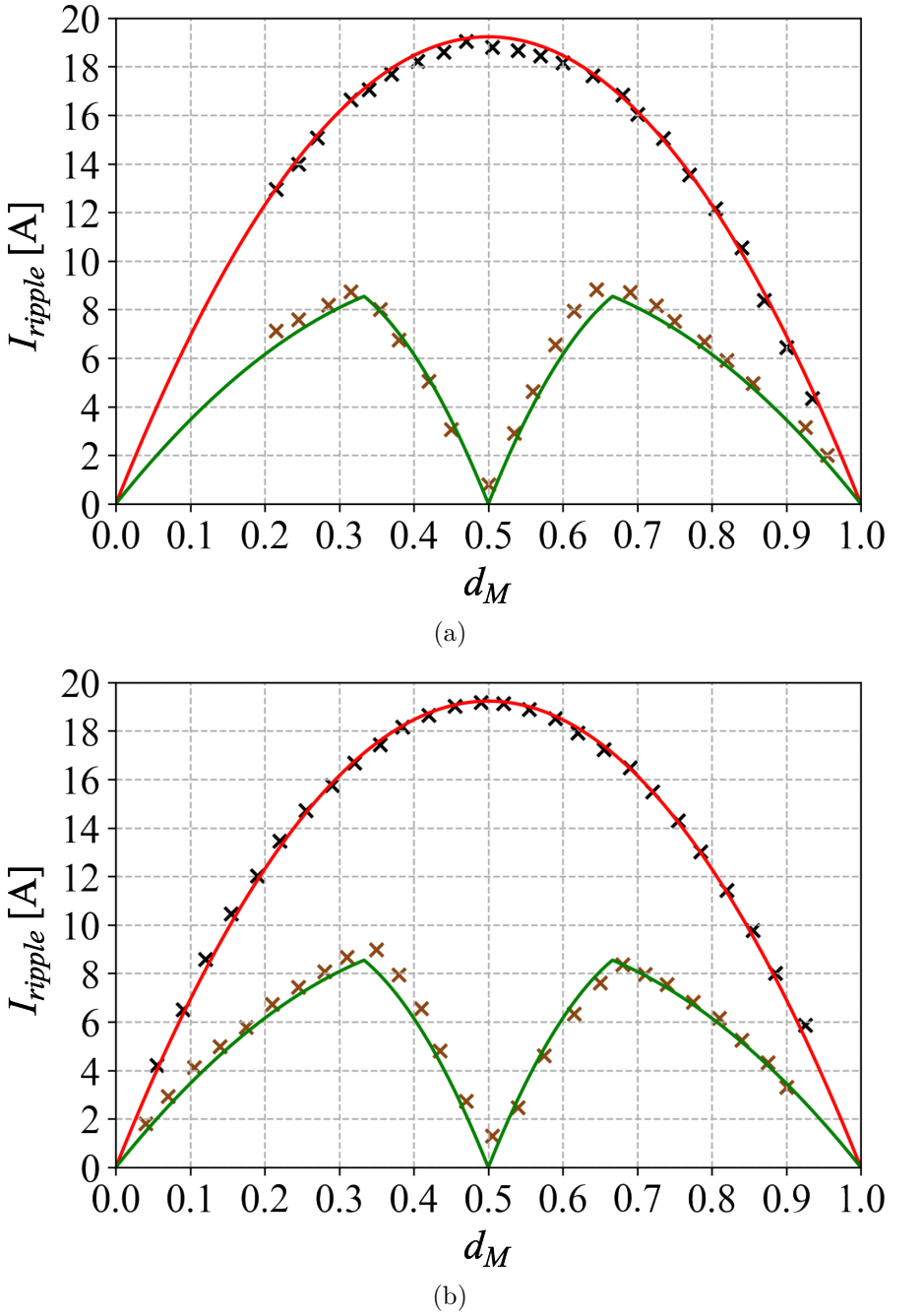

Figure 3.12: Theoretical and experimental ripple currents of CBC and BCSAC under $V_{dc1} = 150\,\mathrm{V}$: (a) $i_L^* = 10\,\mathrm{A}$, (b) $i_L^* = -10\,\mathrm{A}$.

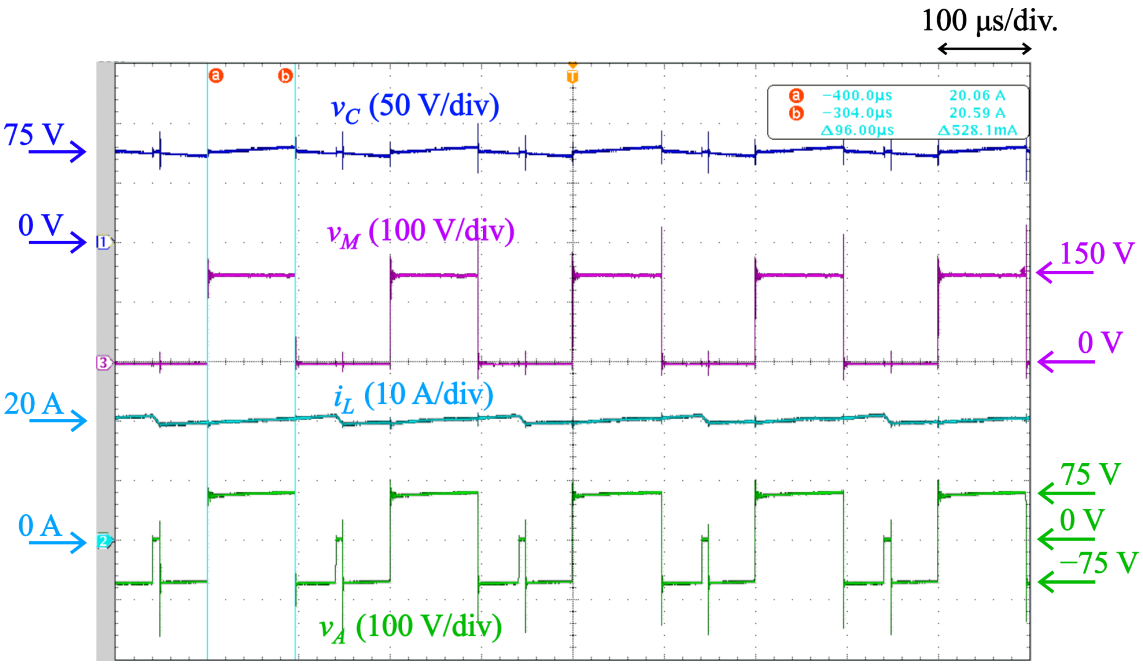

Figure 3.13: Experimental waveforms for the steady-state operation of the BCSAC under $V_{dc1} = 150\,\text{V}$, $V_{dc2} = 65\,\text{V}$, and $i_L^* = 20\,\text{A}$.

switching-ripple current under $i_L^* = 10\,\text{A}$ for the CBC is 19 A (when $d_M = 0.47$), while that for the BCSAC is around 8.8 A (when $d_M = 0.32$ or 0.65). Fig. 3.12b shows that the maximum experimental switching-ripple current under $i_L^* = -10\,\text{A}$ for the CBC is 19.2 A (when $d_M = 0.49$), while that for the BCSAC is around 8.7 A (when $d_M = 0.35$ or 0.68). In comparison, the maximum value for the theoretical ripple current of the BCSAC obtained from (3.77) is 8.4 A. The reason why there are small differences between the theoretical and experimental ripple currents for the BCSAC is the omission of v_B^* in the theoretical analysis. This affects the calculation of d_M, which consequently affect the calculation of I_{ripple}. However, the differences are negligible if compared to the value of I_{ripple}.

3.6.3 Steady-State Operations

3.6.3.1 Operation under Positive i_L

The steady-state experimental waveforms of the BCSAC under $V_{dc1} = 150\,\text{V}$, $V_{dc2} = 65\,\text{V}$, and $i_L^* = 20\,\text{A}$ are given in Fig. 3.13. Positive current implies that the current flows from the high-voltage side to the low-voltage side. The main converter voltage, v_M, is a rectangular wave with DC and AC components, which alternates between V_{dc1} (= 150 V) and 0. Further, d_M is indicated to be 0.48, which is higher than the theoretical value of 0.43 obtained from (3.13). The small difference between the experimental and theoretical

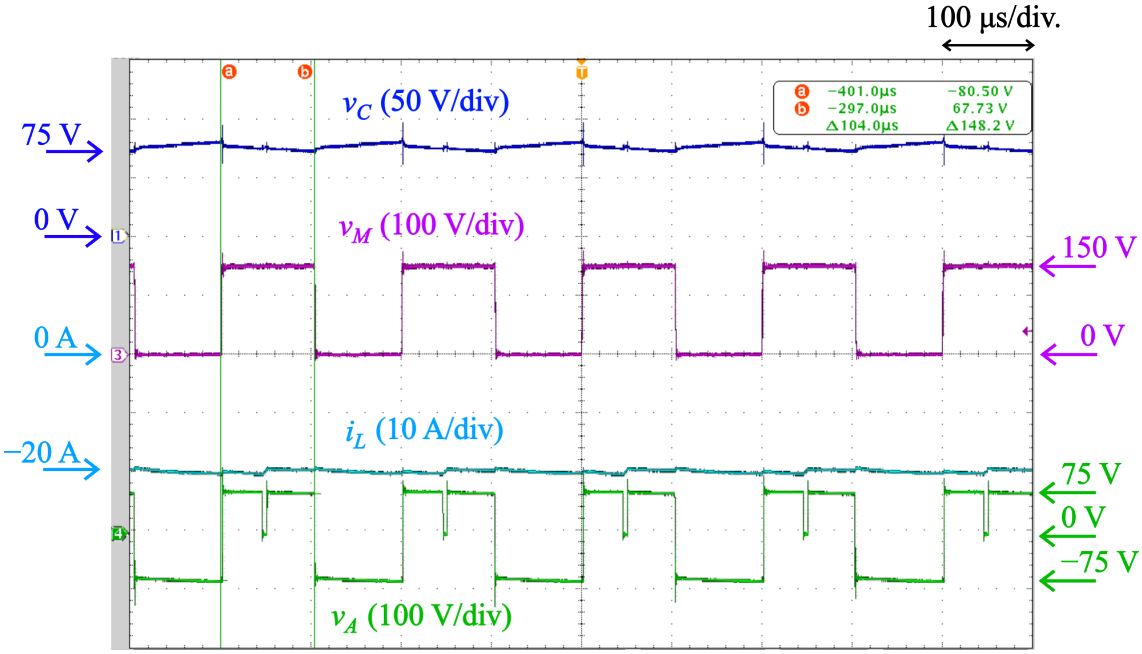

Figure 3.14: Experimental waveforms for the steady-state operation of the BCSAC under $V_{dc1} = 150\,\text{V}$, $V_{dc2} = 85\,\text{V}$, and $i_L^* = -20\,\text{A}$.

results is due to the existence of v_B^* in the main converter control shown in Fig. 3.3. Meanwhile, the auxiliary converter voltage, v_A, alternates between $-V_C$ $(= -75\,\text{V})$, 0, and V_C $(= 75\,\text{V})$.

From Fig. 3.13, the DC-capacitor voltage, v_C, can be regulated at $75\,\text{V}$ $(= \frac{V_{dc1}}{2})$ with no steady-state error. Similarly, the inductor current, i_L, can be regulated to its reference value at $20\,\text{A}$ with no steady-state error. Further, the ripple current of i_L is shown to be $1.89\,\text{A}$, which agrees well with the theoretical peak-to-peak ripple current for d_M in the range of $0.33 \leq d_M < 0.5$ obtained from (3.51) at $1.46\,\text{A}$. The small difference in the experimental and theoretical values for the ripple current is caused by the v_B^* in the main converter control.

3.6.3.2 Operation under Negative i_L

The steady-state experimental waveforms of the BCSAC under $V_{dc1} = 150\,\text{V}$, $V_{dc2} = 85\,\text{V}$, and $i_L^* = 20\,\text{A}$ are given in Fig. 3.14. Negative current implies that the current flows from the low-voltage side to the high-voltage side. The main converter voltage, v_M, is a rectangular wave with DC and AC components, which alternates between V_{dc1} $(= 150\,\text{V})$ and 0. Further, d_M is indicated to be 0.53, which is lower than the theoretical value of 0.57 obtained from (3.13). The small difference between the experimental and theoretical

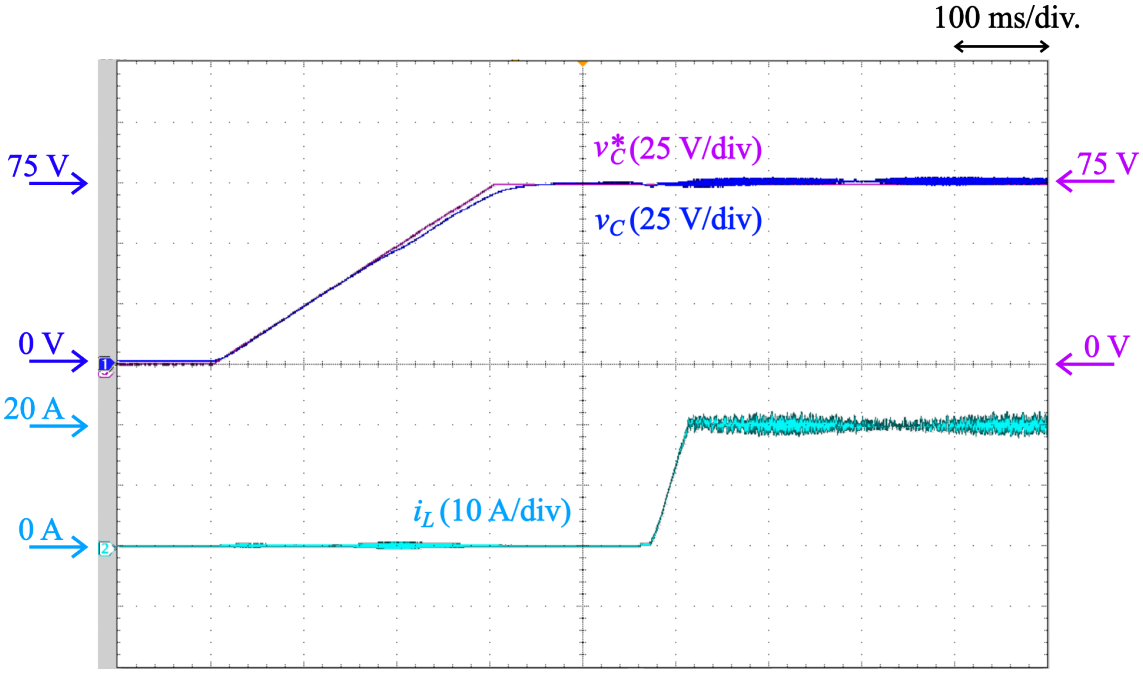

Figure 3.15: Experimental waveforms during the initial charging procedure of the BCSAC under $V_{dc1} = 150\,\text{V}$ and $V_{dc2} = 75\,\text{V}$.

results is due to the existence of v_B^* in the main converter control shown in Fig. 3.3. Meanwhile, the auxiliary converter voltage, v_A, alternates between $-V_C$ ($= -75\,\text{V}$), 0, and V_C ($= 75\,\text{V}$).

From Fig. 3.14, the DC-capacitor voltage, v_C, can be regulated at $75\,\text{V}$ ($= \frac{V_{dc1}}{2}$) with no steady-state error. Similarly, the inductor current, i_L, can be regulated to its reference value at $-20\,\text{A}$ with no steady-state error. Further, the ripple current of i_L is shown to be $1.45\,\text{A}$, which agrees well with the theoretical peak-to-peak ripple current for d_M in the range of $0.5 \leq d_M < 0.67$ obtained from (3.76) at $2.14\,\text{A}$. The small difference in the experimental and theoretical values for the ripple current is caused by the v_B^* in the main converter control.

3.6.4 Transient-State Operations

3.6.4.1 Operation during the Initial Charging of v_C

The transient experimental waveforms of the BCSAC during initial charging procedure under $V_{dc1} = 150\,\text{V}$ and $V_{dc2} = 75\,\text{V}$ are shown in Fig. 3.15. Since V_{dc1} is set as the high-voltage side, while V_{dc2} is the low-voltage side, V_{dc1} is used to charge the capacitor. To send the power from V_{dc1} to the capacitor, the full-bridge auxiliary converter is operated in charging mode during the initial state of the operation, where S_3 and S_6 are ON, while S_4

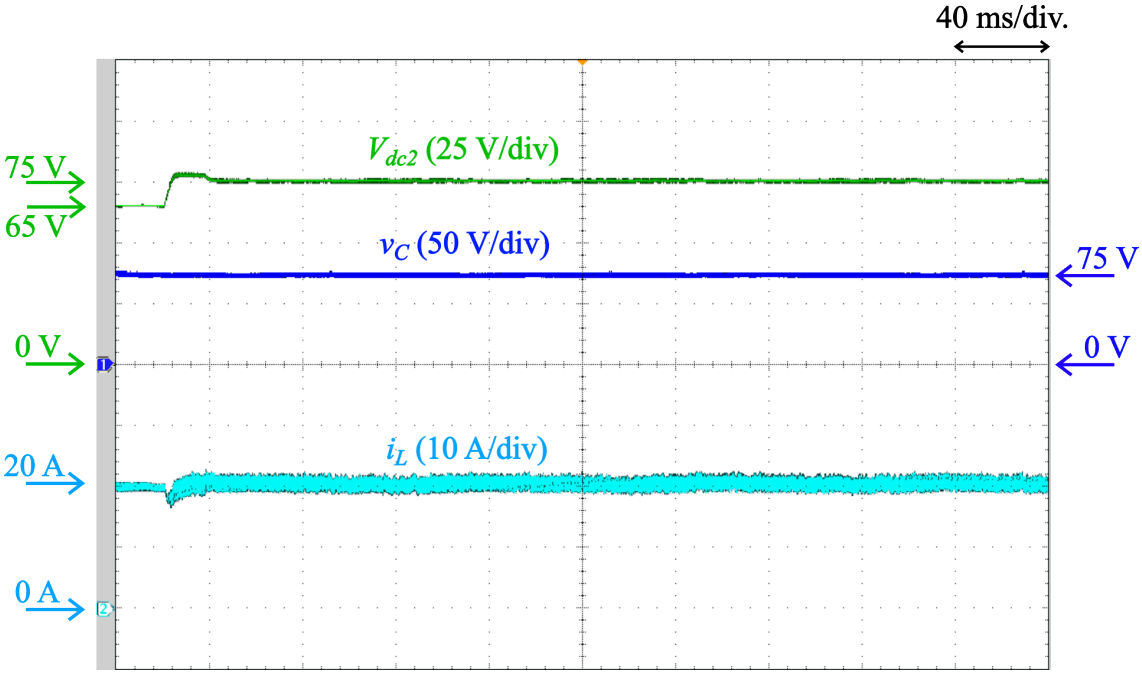

Figure 3.16: Experimental waveform during a step change in the V_{dc2} from 65 V to 75 V of the BCSAC under $V_{dc1} = 150$ V and $i_L^* = 20$ A.

and S_5 are OFF. Meanwhile, in the main converter, S_2 is always OFF, and S_1 is controlled to charge the capacitor voltage, v_C. Specifically, the duty ratio of S_1, d_M, is determined using the traditional PI control to apply feedback control, where v_C is changed from zero to 75 V in 300 ms. After v_C reaches 75 V, the BCSAC operates normally, and i_L goes from zero to 20 A in approximately 40 ms. It can be seen from Fig. 3.15 that the initial charging procedure can be completed with neither overvoltage nor overcurrent occuring in the process.

3.6.4.2 Operation during the Step Change in V_{dc2}

The transient experimental waveforms during a step change in the V_{dc2} of the BCSAC under $V_{dc1} = 150$ V and $i_L^* = 20$ A are shown in Fig. 3.16. It can be seen that V_{dc2} changes from 65 V to 75 V in 20 ms with no overvoltage. There is a slight drop in the inductor current, i_L, at the initial part of the step change. This is because the increase in V_{dc2} inversely affects the inductor voltage, v_L. Further, the ripple current is increased when V_{dc2} is changed. This is because the change in V_{dc2} increases d_M, added by the existence of v_B^*, which consequently affects the resulting ripple current. Meanwhile, the DC-capacitor voltage, v_C, can be stably regulated with no error even during the transient state (i.e., step change).

3.7 Conclusion

This Chapter presents the proposal of a bidirectional chopper with a single full-bridge auxiliary converter (BCSAC) to reduce the inductor volume without a significant power loss compensation. The BCSAC consists of a conventional bidirectional chopper (CBC) as its main converter, a single-phase full-bridge converter equipped with a floating capacitor as its auxiliary converter, and an inductor. The auxiliary converter functions as an active power filter that cancels the AC voltage produced by the main converter, which reduces the switching-ripple current in the inductor. Further, in order to produce less power loss than the bidirectional chopper with an auxiliary converter (BCAC), the DC-capacitor voltage in the BCSAC is set to be half of the DC-voltage-source voltage of the high-voltage side, V_{dc1}, and the switching frequencies of the main and auxiliary converters are set to be the same. Although these settings can potentially results in an increased switching-ripple current, theoretical analysis has shown that the BCSAC is able to reduce the maximum switching-ripple current to $\frac{4}{9}$ of that the CBC. Consequently, the inductor volume can be reduced by 38.4 % and 10.5 % compared to the CBC and three-level flying capacitor converter (TLFC), respectively. Overall, the BCSAC is smaller in volume than the BCAC and lighter than the CBC and TLFC. Further, loss analysis has shown that the BCSAC produces significantly lower power loss than the BCAC, which is only slightly higher than the CBC and TLFC. Thus, high efficiency performance can be achieved. Finally, experimental results using a 2 kW down-scaled model has verified the theoretical analysis results of the switching-ripple current, as well as the operations and controls of the BCSAC in the steady states under both positive and negative currents, and transient states, i.e., during the initial charging procedure and under a step change.

Chapter 4

Evaluation of Phase Shift Application in BCSAC

This Chapter proposes the application of phase shift to the carrier waveforms of the main and auxiliary converters in the bidirectional chopper with a single full-bridge auxiliary converter (BCSAC) to further reduce the switching-ripple current produced by the chopper, while similarly focusing on its implementation in electric railways. In this Chapter, the circuit configuration and operating principle of the BCSAC-PS are presented. The control methods for both the main and auxiliary converters are explained. Theoretical analysis and comparison on the switching-ripple current, inductor volume, chopper volume and mass, power loss, and efficiency with other topologies, including the results given in Chapter 3, are given to validate the significance of phase shift application in the BCSAC. Finally, the validity of the theoretical analysis on the switching-ripple current is confirmed through an experiment using a 2 kW down-scaled model.

4.1 Circuit Configuration and Operating Principle

4.1.1 Circuit Configuration

The circuit configuration of the BCSAC-PS is shown in Fig. 4.1a, which is the same as that shown in Chapter 3.1. In the BCSAC-PS, the main converter carrier, $\mathrm{tri_M}$, lags the auxiliary converter carrier, $\mathrm{tri_A}$, by 90°, as shown in Fig. 4.1b. The application of phase shift to the carriers is intended to further reduce the switching-ripple current produced by the BCSAC. To confirm this point, the results of the theoretical analysis

on the switching-ripple current is given in Chapter 4.3. The other operating conditions used in this Chapter is the same as that used in Chapter 3 with the same objective, i.e., to minimize the produced power loss in the chopper. The DC-capacitor voltage is set to be half of the DC-source voltage at the high voltage side (i.e., $V_C = \frac{V_{dc1}}{2}$). Meanwhile, the relationship $f_{SM} = f_{SA}$ holds, where f_{SM} indicates the frequency of tri_M, while f_{SA} indicates the frequency of tri_A.

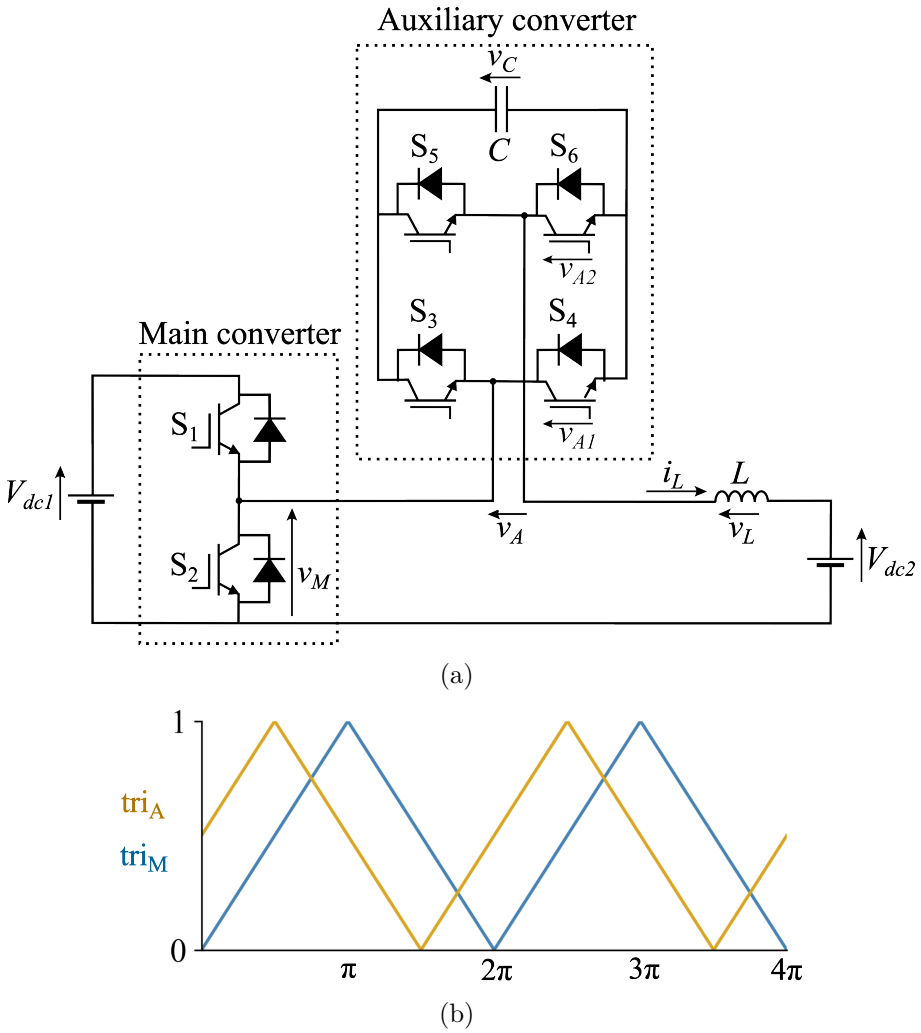

Figure 4.1: The BCSAC-PS: (a) Circuit configuration, (b) Carrier waveforms

4.1.2 Operating Principle

The operating principle of the BCSAC when phase shift is applied is the same as that explained in Chapter 3.2.2. When the deadtime is zero, v_M in the BCSAC-PS is given by:

$$v_M = \begin{cases} V_{dc1} & (\mathrm{S_1}\text{: ON, } \mathrm{S_2}\text{: OFF}) \\ 0 & (\mathrm{S_1}\text{: OFF, } \mathrm{S_2}\text{: ON}) \end{cases}. \tag{4.1}$$

If the duty ratio of $\mathrm{S_1}$ is assumed to be d_M, the DC component of v_M, $(v_M)_{dc}$, is given by:

$$(v_M)_{dc} = d_M V_{dc1}. \tag{4.2}$$

From (4.1) and (4.2), the AC component of v_M, $(v_M)_{ac}$ can be determined as:

$$(v_M)_{ac} = \begin{cases} (1-d_M)\, V_{dc1} & (\mathrm{S_1}\text{: ON, } \mathrm{S_2}\text{: OFF}) \\ -d_M V_{dc1} & (\mathrm{S_1}\text{: OFF, } \mathrm{S_2}\text{: ON}) \end{cases}. \tag{4.3}$$

Meanwhile, for the auxiliary converter to function as an active power filter, its AC output has to be equal to that of the main converter (i.e., $(v_A)_{ac} = (v_M)_{ac}$), so that the AC component in the inductor can be reduced to zero. Considering that $(v_M)_{ac}$ has the maximum value of V_{dc1} and the minimum value of $-V_{dc1}$ based on (4.3), $(v_A)_{ac}$ should have the same maximum and minimum values. When overmodulation is considered, $(v_A)_{ac}$ when $0 \leq d_M < 0.5$ is given by:

$$(v_A)_{ac} = \begin{cases} 0.5 V_{dc1} & (\mathrm{S_1}\text{: ON, } \mathrm{S_2}\text{: OFF}) \\ -d_M V_{dc1} + \frac{{d_M}^2 - 0.5 d_M}{d_M - 1} V_{dc1} & (\mathrm{S_1}\text{: OFF, } \mathrm{S_2}\text{: ON}) \end{cases}. \tag{4.4}$$

Meanwhile, when $0.5 \leq d_M \leq 1$, it is given by:

$$(v_A)_{ac} = \begin{cases} (1-d_M)\, V_{dc1} + \frac{{d_M}^2 - 1.5 d_M + 0.5}{d_M} V_{dc1} & (\mathrm{S_1}\text{: ON, } \mathrm{S_2}\text{: OFF}) \\ -0.5 V_{dc1} & (\mathrm{S_1}\text{: OFF, } \mathrm{S_2}\text{: ON}) \end{cases}. \tag{4.5}$$

Based on (4.3), (4.4), and (4.5), the relationship $(v_A)_{ac} = (v_M)_{ac}$ holds when $d_M = 0.5$. In this situation, the frequency component f_{SM} contained in $(v_M)_{ac}$ is canceled out by the

auxiliary converter so that no frequency component of f_{SM} exists in the inductor current. On the contrary, the relationship $(v_A)_{ac} = (v_M)_{ac}$ does not hold when $d_M \neq 0.5$. In this situation, the frequency component of f_{SM} remains in the inductor current.

4.2 Control Method

The control methods of the BCSAC-PS are basically the same as the ones for the BCSAC given in Chapter 3.3. The DC-capacitor voltage control is performed by the main converter, while the auxiliary converter is used to achieve the inductor current control. Similarly, the resulting duty ratio of S_1, d_M, can be expressed as:

$$d_M = \frac{v_B^* + V_{dc2}}{V_{dc1}}, \tag{4.6}$$

with a maximum value of +1 and a minimum value of zero. The detailed explanation on the principle of the DC-capacitor voltage control has been given in Chapter 3.3.1. Meanwhile, the resulting duty ratios of S_3 and S_5, d_{A1} and d_{A2}, respectively, can be expressed as:

$$d_{A1} = \frac{-v_i^* + v_B^* + (v_A)_{ac}}{v_C} \tag{4.7}$$

$$d_{A2} = \frac{v_i^* - v_B^* - (v_A)_{ac}}{v_C}, \tag{4.8}$$

with a maximum value of +1 and a minimum value of −1. The detailed explanation on the principle of the inductor current control has been given in Chapter 3.3.2.

4.3 Theoretical Analysis on Switching-Ripple Current

The objective of the application of phase shift to the BCSAC is to further reduce the switching-ripple current in the inductor. To evaluate the achievement of that objective, theoretical analysis of the switching-ripple current is conducted.

4.3.1 Assumptions Used in the Analysis

The theoretical analysis of the switching-ripple current in this Chapter is conducted under similar assumptions as those applied in Chapter 3.4:

- Steady-state operation with no power loss is considered (i.e., $v_B^* = 0$).

- The deadtimes of the main and auxiliary converters are zero, which is held when the deadtime is sufficiently shorter than the switching period.
- The relationship $V_C = \frac{V_{dc1}}{2}$ holds, where the AC component in the DC-capacitor voltage is assumed to be zero.

Under the first assumption, d_M becomes:

$$d_M = \frac{V_{dc2}}{V_{dc1}}. \tag{4.9}$$

Further, d_{A1} and d_{A2} obtained from (4.7) and (4.8) becomes:

$$d_{A1} = \frac{-v_i^* + (v_A)_{ac}}{v_C} \tag{4.10}$$

$$d_{A2} = \frac{v_i^* - (v_A)_{ac}}{v_C}. \tag{4.11}$$

In the following analysis, d_M is compared with $\mathrm{tri_M}$, while d_{A1} and d_{A2} are compared with $\mathrm{tri_A}$. Further, considering the difference of the $(v_A)_{ac}$ equations relative to d_M, the theoretical analysis on the switching-ripple current is done separately for d_M in the ranges of $0 \leq d_M < 0.5$ and $0.5 \leq d_M \leq 1$.

4.3.2 When $0 \leq d_M < 0.5$

The example of the ideal voltage and current waveforms of the BCSAC-PS when $d_M = 0.25$ is shown in Fig. 4.2, where the following assumptions are considered:

- θ_1 and θ_4 are the intersection points between $\mathrm{tri_M}$ and d_M.
- θ_2 is the intersection point between $\mathrm{tri_A}$ and d_{A2}.
- θ_3 is the intersection point between $\mathrm{tri_A}$ and d_{A1}.
- The relationships $\theta_1 \leq \theta_2$ and $\theta_3 \leq \theta_4$ hold.

Based on Fig. 4.2, θ_1 and θ_4 can be determined as:

$$\theta_1 = \pi d_M \tag{4.12}$$

$$\theta_4 = 2\pi - \pi d_M, \tag{4.13}$$

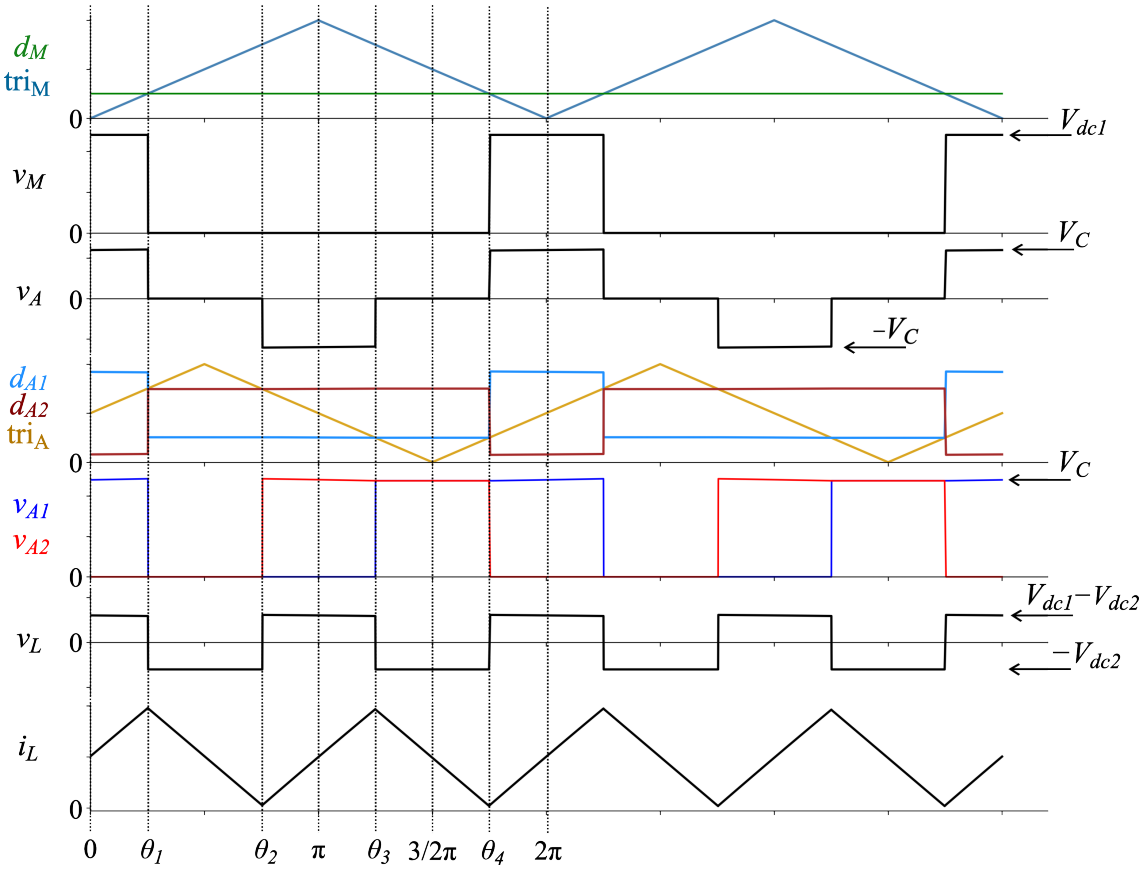

Figure 4.2: Ideal voltage and current waveforms of the BCSAC-PS when $d_M = 0.25$.

where the relationship $\theta_1 \leq \theta_4$ always holds. Based on (4.1), v_M is given by:

$$v_M = \begin{cases} V_{dc1} & (0 \leq \theta < \theta_1, \theta_4 < \theta \leq 2\pi) \\ 0 & (\theta_1 \leq \theta \leq \theta_4) \end{cases}. \tag{4.14}$$

Based on (4.4), (4.10), and (4.11), while also applying $V_C = \frac{V_{dc1}}{2}$, the duty ratios d_{A1} and d_{A2} that have been normalized (i.e., $0 \leq d_{A1} \leq 1$ and $0 \leq d_{A2} \leq 1$) are given by:

$$d_{A1} = \begin{cases} -\frac{v_i^*}{V_{dc1}} + 1 & (0 \leq \theta < \theta_1, \theta_4 < \theta \leq 2\pi) \\ -\frac{v_i^*}{V_{dc1}} + \frac{0.5}{d_M - 1} + 1 & (\theta_1 \leq \theta \leq \theta_4) \end{cases} \tag{4.15}$$

$$d_{A2} = \begin{cases} \frac{v_i^*}{V_{dc1}} & (0 \leq \theta < \theta_1, \theta_4 < \theta \leq 2\pi) \\ \frac{v_i^*}{V_{dc1}} - \frac{0.5}{d_M - 1} & (\theta_1 \leq \theta \leq \theta_4) \end{cases}. \tag{4.16}$$

Based on Fig. 4.2 and (4.15), θ_3 can be determined as:

$$\theta_3 = \pi \left(\frac{v_i^*}{V_{dc1}} - \frac{0.5}{d_M - 1} + \frac{1}{2} \right). \tag{4.17}$$

Meanwhile, based on Fig. 4.2 and (4.16), θ_2 can be determined as:

$$\theta_2 = \pi \left(-\frac{v_i^*}{V_{dc1}} + \frac{0.5}{d_M - 1} + \frac{3}{2} \right). \tag{4.18}$$

Further, the value of v_A from θ_1 through θ_4 is given from Fig. 4.2 by:

$$v_A = \begin{cases} V_C & (0 \leq \theta \leq \theta_1) \\ 0 & (\theta_1 < \theta \leq \theta_2) \\ -V_C & (\theta_2 < \theta \leq \theta_3) \\ 0 & (\theta_3 < \theta \leq \theta_4) \\ V_C & (\theta_4 \leq \theta \leq 2\pi) \end{cases}. \tag{4.19}$$

In the auxiliary converter control using DC component-based control, the voltage command v_i^* is adjusted so that v_A under the steady-state contains only the AC component (i.e., it should average zero in one switching period). Thus, considering (4.12), (4.13), (4.17), and (4.18), v_i^* can be determined as:

$$v_i^* = \frac{(2d_M - 1)\, d_M}{2\,(2d_M - 1)} V_{dc1}. \tag{4.20}$$

Substituting (4.20) into (4.18) and (4.17) yields:

$$\theta_2 = \pi\,(-d_M + 1) \tag{4.21}$$

$$\theta_3 = \pi\,(d_M + 1)\,. \tag{4.22}$$

Based on (4.12), (4.13), (4.21), and (4.22), the relationships $\theta_1 \leq \theta_2$ and $\theta_3 \leq \theta_4$ always hold in the range $0 \leq d_M < 0.5$, which validates the fourth assumption.

Further, the validity of the assumptions that d_{A2} intersects $\mathrm{tri_A}$ at θ_2 (the second assumption), while d_{A1} intersects $\mathrm{tri_A}$ at θ_3 (the third assumption), should be confirmed.

Substituting (4.20) into (4.15) and (4.16) yields:

$$d_{A1} = \begin{cases} -d_M - \frac{0.5}{(d_M-1)} + \frac{1}{2} & (0 \le \theta < \theta_1, \theta_4 < \theta \le 2\pi) \\ -d_M + \frac{1}{2} & (\theta_1 \le \theta \le \theta_4) \end{cases} \tag{4.23}$$

$$d_{A2} = \begin{cases} d_M + \frac{0.5}{(d_M-1)} + \frac{1}{2} & (0 \le \theta < \theta_1, \theta_4 < \theta \le 2\pi) \\ d_M + \frac{1}{2} & (\theta_1 \le \theta \le \theta_4) \end{cases}. \tag{4.24}$$

From Fig. 4.2, the values of $\mathrm{tri_M}$ at θ_1 and θ_4 correspond to d_M. Meanwhile, the value of d_{A2} at θ_1 is obtained from (4.24) as $d_M + \frac{1}{2}$, which always gives higher value than d_M in the range of $0 \le d_M < 0.5$. This signifies that the phase θ_2 that satisfies $\theta_2 \ge \theta_1$ always exists for d_M in the range of $0 \le d_M < 0.5$. Meanwhile, the value of d_{A1} at θ_4 is obtained from (4.23) as $-d_M + \frac{1}{2}$, which only gives higher value than d_M in the range of $0 \le d_M < 0.25$. However, when the phase shift applied to $\mathrm{tri_A}$ is considered, the phase θ_3 that satisfies $\theta_3 \le \theta_4$ similarly always exists for d_M in the range of $0 \le d_M < 0.5$.

Based on KVL, (4.14), (4.19), while also applying $V_C = \frac{V_{dc1}}{2}$, the inductor voltage, v_L, can be determined as:

$$\begin{aligned} v_L &= v_M - v_A - V_{dc2} \\ &= \begin{cases} 0.5V_{dc1} - V_{dc2} & (0 \le \theta \le \theta_1) \\ -V_{dc2} & (\theta_1 < \theta \le \theta_2) \\ 0.5V_{dc1} - V_{dc2} & (\theta_2 < \theta \le \theta_3) \\ -V_{dc2} & (\theta_3 < \theta \le \theta_4) \\ 0.5V_{dc1} - V_{dc2} & (\theta_4 < \theta \le 2\pi) \end{cases}. \end{aligned} \tag{4.25}$$

From (4.25), given that the relationship $d_M = \frac{V_{dc2}}{V_{dc1}} < 0.5$ holds, the following trends hold for the inductor current, i_L:

- i_L rises with the rate of $0.5V_{dc1} - V_{dc2}$ within the range of $0 \le \theta \le \theta_1$ $(= I_{rise1})$, $\theta_2 < \theta \le \theta_3$ $(= I_{rise2})$, and $\theta_4 < \theta \le 2\pi$ $(= I_{rise3})$.

- i_L drops with the rate of $-V_{dc2}$ within the range of $\theta_1 < \theta \le \theta_2$ $(= I_{drop1})$ and $\theta_3 < \theta \le \theta_4$ $(= I_{drop2})$.

Further, the rising and dropping rates remain consistent under steady state. From (4.12) and (4.25), I_{rise1} is given by:

$$I_{rise1} = \frac{1}{\omega L}\int_{0}^{\theta_1}(0.5V_{dc1} - V_{dc2})\,d\theta \;= \frac{V_{dc1}}{2f_{SM}L}\frac{(1-2d_M)\,d_M}{2}. \tag{4.26}$$

From (4.12), (4.21), and (4.25), I_{drop1} is given by:

$$I_{drop1} = -\frac{1}{\omega L}\int_{\theta_1}^{\theta_2}(-V_{dc2})\,d\theta \;= \frac{V_{dc1}}{2f_{SM}L}(1-2d_M)\,d_M. \tag{4.27}$$

From (4.21), (4.22), and (4.25), I_{rise2} is given by:

$$I_{rise2} = \frac{1}{\omega L}\int_{\theta_2}^{\theta_3}(0.5V_{dc1} - V_{dc2})\,d\theta \;= \frac{V_{dc1}}{2f_{SM}L}(1-2d_M)\,d_M. \tag{4.28}$$

From (4.22), (4.13), and (4.25), I_{drop2} is given by:

$$I_{drop2} = -\frac{1}{\omega L}\int_{\theta_3}^{\theta_4}(-V_{dc2})\,d\theta \;= \frac{V_{dc1}}{2f_{SM}L}(1-2d_M)\,d_M. \tag{4.29}$$

From (4.13), and (4.25), I_{rise3} is given by:

$$I_{rise3} = \frac{1}{\omega L}\int_{\theta_4}^{\theta_5}(0.5V_{dc1} - V_{dc2})\,d\theta \;= \frac{V_{dc1}}{2f_{SM}L}\frac{(1-2d_M)\,d_M}{2}. \tag{4.30}$$

Based on (4.26) to (4.30), the relationship $I_{drop1} = I_{rise2} = I_{drop2} > I_{rise1} = I_{rise3}$ always holds for d_M in the range of $0 \leq d_M < 0.5$. As such, the peak-to-peak ripple current, I_{ripple}, in the given range is determined as:

$$I_{ripple} = \frac{V_{dc1}}{2f_{SM}L}(1-2d_M)\,d_M. \tag{4.31}$$

4.3.3 When $0.5 \leq d_M \leq 1$

The example of the ideal voltage and current waveforms of the BCSAC-PS when $d_M = 0.75$ is shown in Fig. 4.3, where the following assumptions are considered:

- θ_1 is the intersection point between tri_A and d_{A1}.
- θ_2 and θ_3 are the intersection points between tri_M and d_M.
- θ_4 is the intersection point between tri_A and d_{A2}.

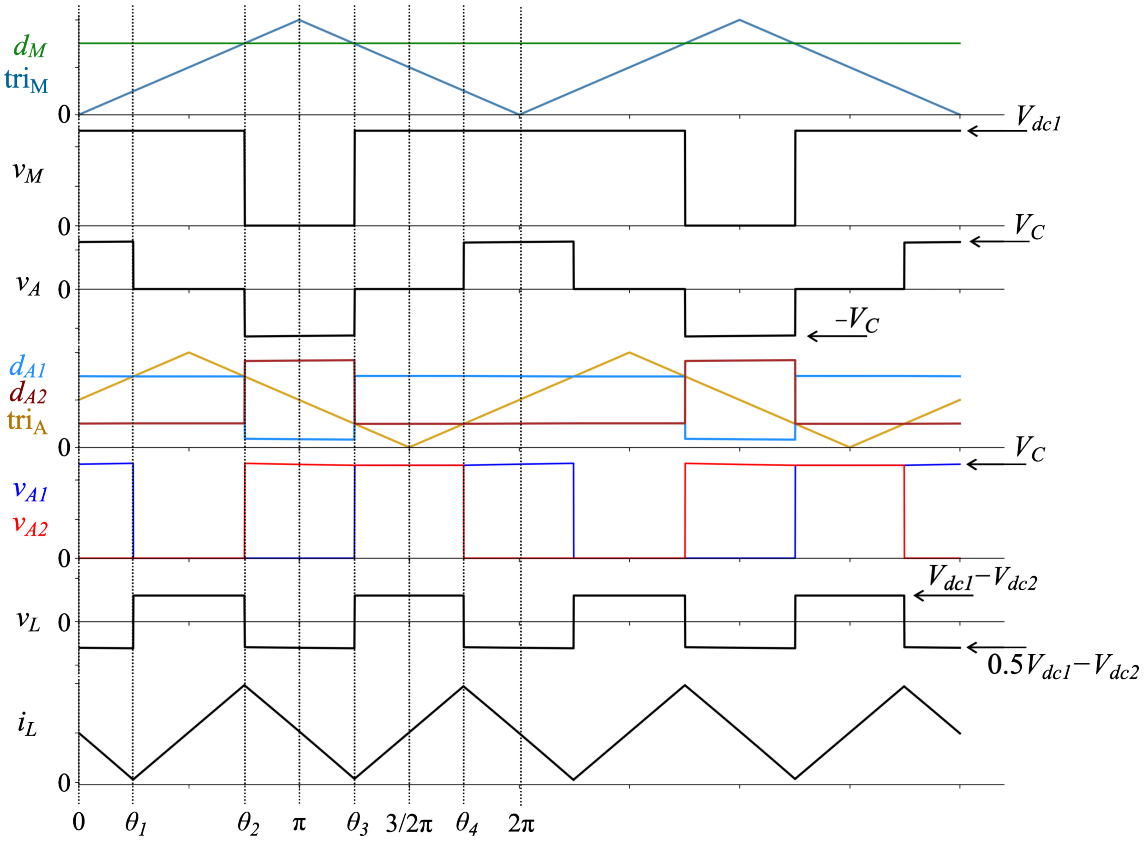

Figure 4.3: Ideal voltage and current waveforms of the BCSAC-PS when $d_M = 0.75$.

- The relationships $\theta_1 \leq \theta_2$ and $\theta_3 \leq \theta_4$ hold.

Based on Fig. 4.3, θ_2 and θ_3 can be determined as:

$$\theta_2 = \pi d_M \tag{4.32}$$

$$\theta_3 = 2\pi - \pi d_M, \tag{4.33}$$

where the relationship $\theta_2 \leq \theta_3$ always holds. Based on (4.1), v_M is given by:

$$v_M = \begin{cases} V_{dc1} & (0 \leq \theta \leq \theta_2, \theta_3 \leq \theta \leq 2\pi) \\ 0 & (\theta_2 < \theta < \theta_3) \end{cases}. \tag{4.34}$$

Based on (4.5), (4.10), and (4.11), while also applying $V_C = \frac{V_{dc1}}{2}$, the duty ratios d_{A1}

and d_{A2} that have been normalized (i.e., $0 \leq d_{A1} \leq 1$ and $0 \leq d_{A2} \leq 1$) are given by:

$$d_{A1} = \begin{cases} -\frac{v_i^*}{V_{dc1}} + \frac{0.5}{d_M} & (0 \leq \theta \leq \theta_2, \theta_3 \leq \theta \leq 2\pi) \\ -\frac{v_i^*}{V_{dc1}} & (\theta_2 < \theta < \theta_3) \end{cases} \tag{4.35}$$

$$d_{A2} = \begin{cases} \frac{v_i^*}{V_{dc1}} + 1 - \frac{0.5}{d_M} & (0 \leq \theta \leq \theta_2, \theta_3 \leq \theta \leq 2\pi) \\ \frac{v_i^*}{V_{dc1}} + 1 & (\theta_2 < \theta < \theta_3) \end{cases}. \tag{4.36}$$

Based on Fig. 4.3 and (4.35), θ_1 can be determined as:

$$\theta_1 = \pi \left(-\frac{v_i^*}{V_{dc1}} + \frac{0.5}{d_M} - \frac{1}{2} \right). \tag{4.37}$$

Meanwhile, based on Fig. 4.3 and (4.36), θ_4 can be determined as:

$$\theta_4 = \pi \left(\frac{v_i^*}{V_{dc1}} - \frac{0.5}{d_M} + \frac{5}{2} \right). \tag{4.38}$$

Further, the value of v_A from θ_1 through θ_4 is given from Fig. 4.3 by:

$$v_A = \begin{cases} V_C & (0 \leq \theta \leq \theta_1) \\ 0 & (\theta_1 < \theta \leq \theta_2) \\ -V_C & (\theta_2 < \theta \leq \theta_3) \\ 0 & (\theta_3 < \theta \leq \theta_4) \\ V_C & (\theta_4 \leq 2\pi) \end{cases}. \tag{4.39}$$

Similarly, the voltage command v_i^* is adjusted so that v_A under the steady-state contains only the AC component (i.e., it should average zero in one switching period). Thus, considering (4.32), (4.33), (4.37), and (4.38), v_i^* can be determined as:

$$v_i^* = \frac{(2d_M - 1)(d_M - 1)}{2d_M} V_{dc1}. \tag{4.40}$$

Substituting (4.40) into (4.37) and (4.38) yields:

$$\theta_1 = \pi\left(-d_M + 1\right) \tag{4.41}$$

$$\theta_4 = \pi\left(d_M + 1\right). \tag{4.42}$$

Based on (4.18), (4.17), (4.41), and (4.42), the relationships $\theta_1 \leq \theta_2$ and $\theta_3 \leq \theta_4$ always hold in the range $0.5 \leq d_M \leq 1$, which validates the fourth assumption.

Further, the validity of the assumptions that d_{A1} intersects $\mathrm{tri_A}$ at θ_1 (the first assumption), while d_{A2} intersects $\mathrm{tri_A}$ at θ_4 (the third assumption), should be confirmed. Substituting (4.40) into (4.35) and (4.36) yields:

$$d_{A1} = \begin{cases} -d_M + \frac{3}{2} & (0 \leq \theta \leq \theta_2, \theta_3 \leq \theta \leq 2\pi) \\ -d_M - \frac{0.5}{d_M} + \frac{3}{2} & (\theta_2 < \theta < \theta_3) \end{cases} \tag{4.43}$$

$$d_{A2} = \begin{cases} d_M - \frac{1}{2} & (0 \leq \theta \leq \theta_2, \theta_3 \leq \theta \leq 2\pi) \\ d_M + \frac{0.5}{d_M} - \frac{1}{2} & (\theta_2 < \theta < \theta_3) \end{cases}. \tag{4.44}$$

From Fig. 4.3, the values of $\mathrm{tri_M}$ at θ_2 and θ_3 correspond to d_M. Meanwhile, the value of d_{A1} at θ_2 is obtained from (4.43) as $-d_M + \frac{3}{2}$, which only gives lower value than d_M in the range of $0.75 \leq d_M \leq 1$. However, when the phase shift applied to $\mathrm{tri_A}$ is considered, the phase θ_1 that satisfies $\theta_1 \leq \theta_2$ always exists for d_M in the range of $0.5 \leq d_M \leq 1$. Meanwhile, the value of d_{A2} at θ_3 is obtained from (4.44) as $d_M - \frac{1}{2}$, which always gives lower value than d_M in the range of $0.5 \leq d_M \leq 1$. This signifies that the phase θ_4 that satisfies $\theta_4 \geq \theta_3$ always exists for d_M in the range of $0.5 \leq d_M \leq 1$.

Based on KVL, (4.34), (4.39), while also applying $V_C = \frac{V_{dc1}}{2}$, the inductor voltage, v_L,

can be determined as:

$$v_L = v_M - v_A - V_{dc2}$$
$$= \begin{cases} 0.5V_{dc1} - V_{dc2} & (0 \leq \theta \leq \theta_1) \\ V_{dc1} - V_{dc2} & (\theta_1 < \theta \leq \theta_2) \\ 0.5V_{dc1} - V_{dc2} & (\theta_2 < \theta \leq \theta_3) \\ V_{dc1} - V_{dc2} & (\theta_3 < \theta \leq \theta_4) \\ 0.5V_{dc1} - V_{dc2} & (\theta_4 < \theta \leq 2\pi) \end{cases} . \tag{4.45}$$

From (4.45), given that the relationship $d_M = \frac{V_{dc2}}{V_{dc1}} \geq 0.5$ holds, the following trends hold for the inductor current, i_L:

- i_L rises with the rate of $V_{dc1} - V_{dc2}$ within the range of $\theta_1 < \theta \leq \theta_2$ $(= I_{rise1})$ and $\theta_3 < \theta \leq \theta_4$ $(= I_{rise2})$.

- i_L drops with the rate of $0.5V_{dc1} - V_{dc2}$ within the range of $0 \leq \theta \leq \theta_1$ $(= I_{drop1})$, $\theta_2 < \theta \leq \theta_3$ $(= I_{drop2})$, and $\theta_4 < \theta \leq 2\pi$ $(= I_{drop3})$.

Further, the rising and dropping rates remain consistent under steady state. Through similar processes done in the previous section, the I_{ripple} for d_M in the range of $0.5 \leq d_M \leq 1$ can be determined as:

$$I_{ripple} = \frac{1}{\omega L} \int_{\theta_3}^{\theta_4} (V_{dc1} - V_{dc2})\, d\theta \; = \frac{V_{dc1}}{2 f_{SM} L} (2d_M - 1)(1 - d_M) . \tag{4.46}$$

4.4 Comparison with Other Topologies

When phase shift is applied in the BCSAC and the switching-ripple current is further reduced, it will correspondingly reduce the inductor volume, chopper volume and mass, and potentially the power loss in the chopper. To evaluate the achievement of that objective, theoretical comparisons on the inductor volume, chopper volume and mass, power loss, and efficiency are carried out between the BCSAC-PS, CBC, TLFC-PS (TLFC with phase shift), and BCSAC. However, cost comparison is beyond the scope of this study, and should be left for future work.

4.4.1 Assumptions Used in the Comparison

The comparison of the switching-ripple current in this Chapter uses the results obtained in Chapter 4.3. Meanwhile, the theoretical analysis of the inductor volume is conducted under similar assumptions as those applied in Chapter 3.5.1:

- Air-core inductors are used, where brooks coil geometry is adopted.
- The inductors operate under a maximum current capacity, I_{max}, of 1000 A and a maximum current density, J_{max}, of 2×10^6 A/m^2.
- Under the same switching frequency, the same amount of ripple current is produced by all choppers.

Additionally, the theoretical analysis of the chopper volume and mass is conducted under similar assumptions as those applied in Chapter 3.5.2:

- The components of the chopper are consisted of the inductor, capacitor, and power devices along with the cooling systems in both the main and auxiliary converters.
- The DC film capacitor E50.N15-323NT0 (32 µF, I_{max} = 50 A) from Electronicon is used, where a parallel connection of twenty capacitors is used in the auxiliary converter, giving an equivalent capacitance value of 0.64 mF.
- Air-cooling system with heatsink is applied, where it is designed based on the CSPI that is set to 7.0 and its density is the same as the density of aluminum (i.e., 2.7 g/cm^3).
- Junction temperature, T_j, is 125°C, while the ambient temperature, T_a, is 40°C.
- The power devices used in the main and auxiliary converters have the same mass.

Finally, the theoretical analysis of the power loss and efficiency is conducted under similar assumptions as those applied in Chapter 3.5.3:

- The deadtimes of the main and auxiliary converters are zero.
- The DC inductor current is positive and constant, while the DC-capacitor voltage is constant.

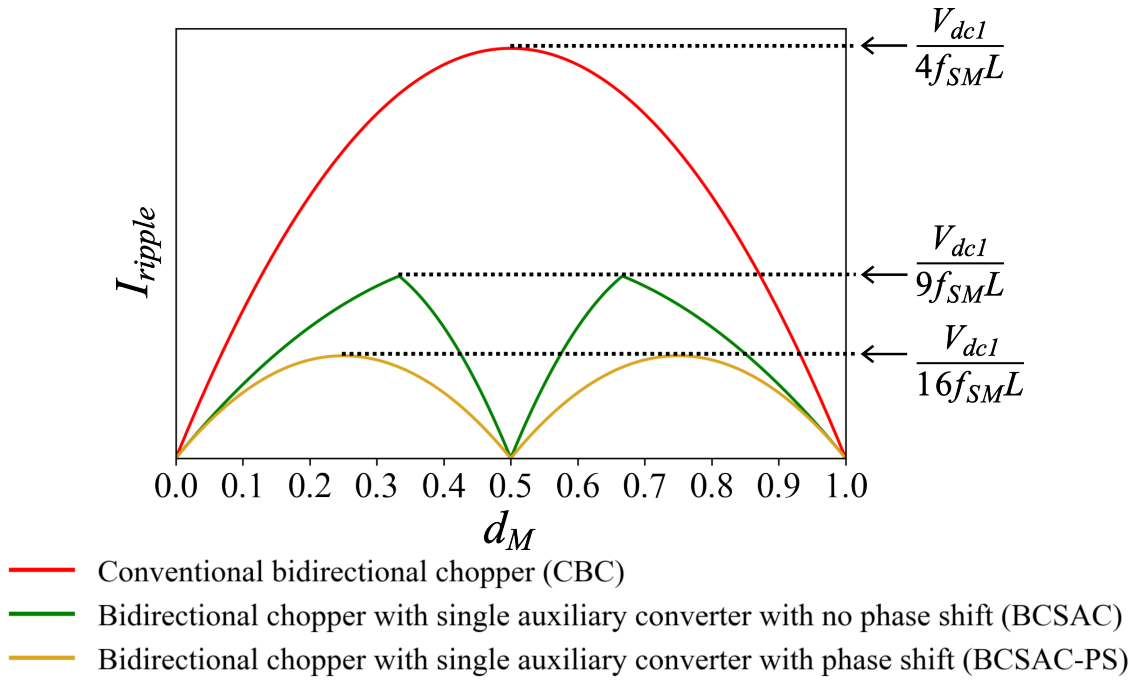

Figure 4.4: Theoretical results for the switching-ripple current of the BCSAC-PS, CBC, and BCSAC.

- The IGBT power modules 1MBI1000UG-330 (Si-IGBT, 1-in-1, 3.3 kV) from Fuji Electric and CM1000DX-24T (Si-IGBT, 1-in-1, 1.2 kV) from Mitsubishi Electric are used.

- The conduction losses of the IGBT and the FWD, the switching loss of the IGBT, the reverse recovery loss of the FWD, and the inductor loss are considered.

4.4.2 Switching-Ripple Current

Based on (4.31) and (4.46), the maximum value for I_{ripple} of the BCSAC-PS is obtained when $d_M = \frac{1}{4}$ and $d_M = \frac{3}{4}$, which is equivalent to:

$$(I_{ripple})_{max} = \frac{V_{dc1}}{16 f_{SM} L}. \tag{4.47}$$

Meanwhile, the $(I_{ripple})_{max}$ of the BCSAC obtained from Chapter 3.4 is:

$$(I_{ripple})_{max} = \frac{V_{dc1}}{9 f_{SM} L}. \tag{4.48}$$

The $(I_{ripple})_{max}$ of the CBC is given as:

$$(I_{ripple})_{max} = \frac{V_{dc1}}{4 f_{SM} L}. \tag{4.49}$$

Based on (4.47) and (4.49), the BCSAC is able to reduce the switching-ripple current to $\frac{1}{4}$ of that produced by the CBC, which is significantly lower than that produced by the BCSAC (i.e., $\frac{4}{9}$ of the CBC). Fig. 4.4 shows the theoretical results for the switching-ripple current of the BCSAC-PS (yellow line), CBC (red line), and BCSAC (green line) under d_M in the range of $0 \leq d_M \leq 1$. It shows that there is a symmetry in the switching-ripple current of the BCSAC-PS between that when d_M in the range of $0 \leq d_M < 0.5$ and $0.5 \leq d_M \leq 1$, similar to that of the BCSAC, and that the advantage of the BCSAC-PS over the CBC is especially apparent when the operating duty ratio is around $d_M = 0.5$. This is because the relationship $(v_A)_{ac} = (v_M)_{ac}$ holds, which eliminates the frequency component f_{SM} in the inductor current.

4.4.3 Inductor Volume

Theoretical analysis on the inductor volume is conducted for the four choppers based on the method described in [101], [104]. The comparison of the calculated parameters of the air-core inductors for all four choppers are summarized in Table 4.1, while the parameter definitions and detailed calculation processes are provided in Appendix B.1. Considering the third assumption held in this analysis and the theoretical results of the switching-ripple current analysis, the inductance value for each chopper is set to $L = 0.9\,\text{mH}$ for the CBC, $L = 0.4\,\text{mH}$ for the BCSAC, and $L = 0.225\,\text{mH}$ for the TLFC-PS and BCSAC-PS. Further, based on the results shown in Table 4.1, the BCSAC-PS enables the utilizations of an inductor with smaller volume ($24.94\,\text{dm}^3$) than the BCSAC ($40.73\,\text{dm}^3$), and certainly the CBC($66.09\,\text{dm}^3$). This translates to inductor volume reductions of around 38.8 % from the BCSAC, and 62.3 % from the CBC, which is comparable to the reduction that can be achieved by the TLFC-PS.

4.4.4 Chopper Volume and Mass

Theoretical analysis on the chopper total volume and mass is conducted to confirm the significance of the improvement on the inductor volume reduction achieved by the BCSAC-

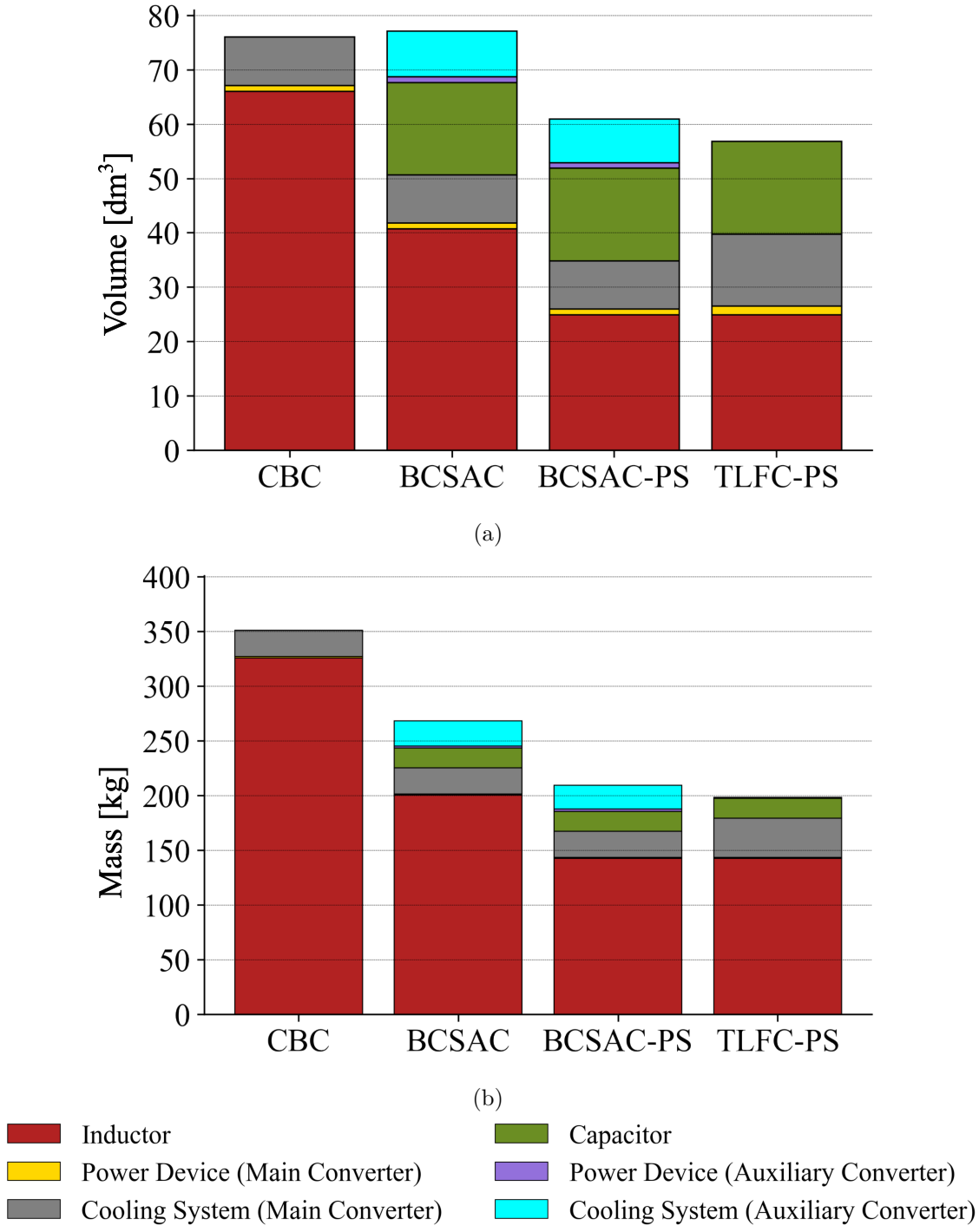

Figure 4.5: Breakdown of the four choppers: (a) Chopper volume, and (b) Chopper mass.

Table 4.1: Parameters used in the inductor volume analysis

Parameter	CBC	BCSAC	TLFC-PS / BCSAC-PS
$\boldsymbol{L}$	0.9 mH	0.4 mH	0.225 mH
$\boldsymbol{a}$	27.6 cm	23.8 cm	16.9 cm
$\boldsymbol{b}$	15.6 cm	13 cm	13 cm
$\boldsymbol{c}$	18.2 cm	15.6 cm	15.6 cm
$\boldsymbol{d}$	25.23 mm	25.23 mm	25.23 mm
d_i	26 mm	26 mm	26 mm
n_t	6	5	5
n_l	7	6	6
n	42	30	30
v_L	66.09 dm^3	40.73 dm^3	24.94 dm^3

PS. The volume breakdown of the four choppers is shown in Fig. 4.5a. The volumes of the capacitor and power devices are estimated based on the dimensions provided in [119]–[121]. Meanwhile, the volume of the cooling system is calculated based on its CSPI value using the methods described in [101], [122], while the detailed calculation processes are provided in Appendix B.2. Based on Fig. 3.8a, the volume of the BCSAC-PS (60.97 dm^3) is around 20 % smaller than the CBC (76.04 dm^3), while also around 21 % smaller than the BCSAC (77.11 dm^3). This is because the achieved inductor volume reduction (41.15 dm^3) is significantly higher than the combined volume of the additional components that come with the auxiliary converter, i.e., the capacitors (17.02 dm^3), the power devices (1.04 dm^3), and the cooling system (8.02 dm^3). Further, the total volume of the BCSAC-PS is only slightly higher than the TLFC-PS (56.83 dm^3).

The mass breakdown of the four choppers is shown in Fig. 4.5b. The masses of the capacitor and power devices are provided in [119]–[121]. Meanwhile, the mass of the cooling system is calculated based on its volume and density. Based on Fig. 4.5b, the mass of the BCSAC-PS (209.09 kg) is around 40.4 % lower than that of the CBC (350.79 kg), and 22 % lower than that of the BCSAC (267.93 kg). However, the BCSAC-PS is slightly heavier than the TLFC-PS (198.34 kg).

4.4.5 Power Loss and Efficiency

The theoretical analysis on the power loss and efficiency is similarly conducted using the specifications data that can be found in [119], [120], while the explanations on the calculation processes are given in Appendix C. The parameters used in the power loss and efficiency analysis for all four choppers are summarized in Table 4.2. The rated power is

Table 4.2: Parameters used in the power loss and efficiency analysis

Parameter	Description	Value
ALL		
$\boldsymbol{P}$	Rated power	1.5 MW
$\boldsymbol{V_{dc1}}$	DC-voltage source 1 (high-voltage side)	1.5 kV
$\boldsymbol{V_{dc2}}$	DC-voltage source 2 (low-voltage side)	0.3 kV and 1.2 kV
$\boldsymbol{f}$	Switching frequency of the chopper	5 kHz
$\boldsymbol{f_{SM}}$	Switching frequency of the main converter	5 kHz
$\boldsymbol{f_{SA}}$	Switching frequency of the auxiliary converter	5 kHz
$\boldsymbol{V_C}$	DC-capacitor voltage	0.75 kV
CBC		
$\boldsymbol{L}$	Inductance	0.9 mH
BCSAC		
$\boldsymbol{L}$	Inductance	0.4 mH
TLFC-PS / BCSAC-PS		
$\boldsymbol{L}$	Inductance	0.225 mH

set to $P = 1.5\,\text{MW}$ with $V_{dc1} = 1.5\,\text{kV}$. Meanwhile, V_{dc2} is alternated between 0.45 and 1.05 kV to conduct the analysis under different values of d_M. All choppers operate under the same switching frequency at 5 kHz. It should be noted that for the TLFC-PS, the equivalent switching frequency is $2f_{TLFC-PS}$, due to the application of phase shift. The inductance values are set to be the same as in Chapter 4.4.3. Finally, V_C is set to be half of V_{dc1} at $V_C = 0.75\,\text{kV}$ for all choppers.

The power loss breakdowns of the four choppers under two different duty ratios (i.e., $d_M = 0.3$ and $d_M = 0.7$) are shown in Fig. 4.6. From Figs. 4.6a and 4.6b, the CBC loses around 7.7 kW of power in total, in average, for the maximum power rating under both d_M values, and it is spread almost evenly among the conduction loss (3.1 kW), switching loss (2 kW), and inductor loss (2.6 kW). Comparatively, both the TLFC-PS and BCSAC produce larger power losses. From Figs. 4.6c and 4.6d, the total power loss of the TLFC-PS is 8.9 kW, in average, where the majority comes from the conduction loss (5.3 kW) and the switching loss (2.5 kW), while the inductor loss contributes less (1.1 kW). Meanwhile, from Figs. 4.6e and 4.6f, the BCSAC produces a total power loss of 11.7 kW, in average. The conduction loss and switching loss contribute 7.4 kW and 2.7 kW, respectively. In comparison, from Figs. 4.6g and 4.6h, the BCSAC-PS produces a total power loss of around 11 kW, which less than that of the BCSAC, but still slightly higher than those of the CBC and the TLFC-PS. The loss reduction comes from the inductor loss and the switching loss of the auxiliary converter (i.e., 1.1 kW and 0.4 kW, respectively), compared

with those produced by the BCSAC (i.e., 1.6 kW and 0.6 kW, respectively). The total induction and switching losses in average are 7.4 kW and 2.5 kW, respectively. In general, the common biggest power loss contributor across the four choppers is the conductor loss, especially that produced by the auxiliary converter, for the BCSAC and BCSAC-PS.

Subsequently, the efficiency for all choppers are calculated based on the results of the power loss analysis and shown in Fig. 4.7, where red line indicates the CBC, blue line indicates the TLFC-PS, green line indicates the BCSAC, and gold line indicates the BCSAC-PS. From Fig. 4.7a, the BCSAC-PS is able to perform at around 98 %, in average, under $d_M = 0.3$. This is slightly higher than the average efficiency of BCSAC at 97.9 %, but lower than those of CBC and TLFC-PS at 98.7 % and 98.4 %, respectively. From Fig. 4.7b, the BCSAC-PS is able to perform at around 99.1 %, in average, under $d_M = 0.7$. This is also higher than the average efficiency of BCSAC at 99 %, but lower than those of CBC and TLFC-PS at 99.4 % and 99.3 %, respectively. It should be noted that the efficiency differences between the four choppers become smaller as the dM increases. Further, the efficiencies for all choppers are the highest when the power rating is 75 kW, where the current is $i_L = 250$ A, for both d_M values.

The comparison results between the four choppers are summarized in Table 4.3. Overall, the BCSAC-PS has shown better performance than the BCSAC, i.e., producing lower switching-ripple current, requiring smaller inductor volume, allowing smaller and lighter chopper, producing lower power loss, and achieving higher efficiency. Compared to the CBC, the BCSAC-PS produces higher power loss and lower efficiency, but enables an inductor with smaller volume, resulting in a smaller and lighter chopper. The results are comparable to those achieved by the TLFC-PS. Additionally, BCSAC-PS will still produce higher power loss and lower efficiency than the CBC with the same chopper volume but produced the same amount of switching-ripple current (i.e., operates with higher frequency). However, considering the reduction in the inductor volume that can be achieved by the BCSAC-PS, the slightly lower efficiency to the CBC and TLFC-PS is a minor issue. In addition, the mass reduction achieved by the BCSAC-PS could reduce the energy required to move the vehicle, which could potentially give positive impact to the overall energy efficiency of the vehicle.

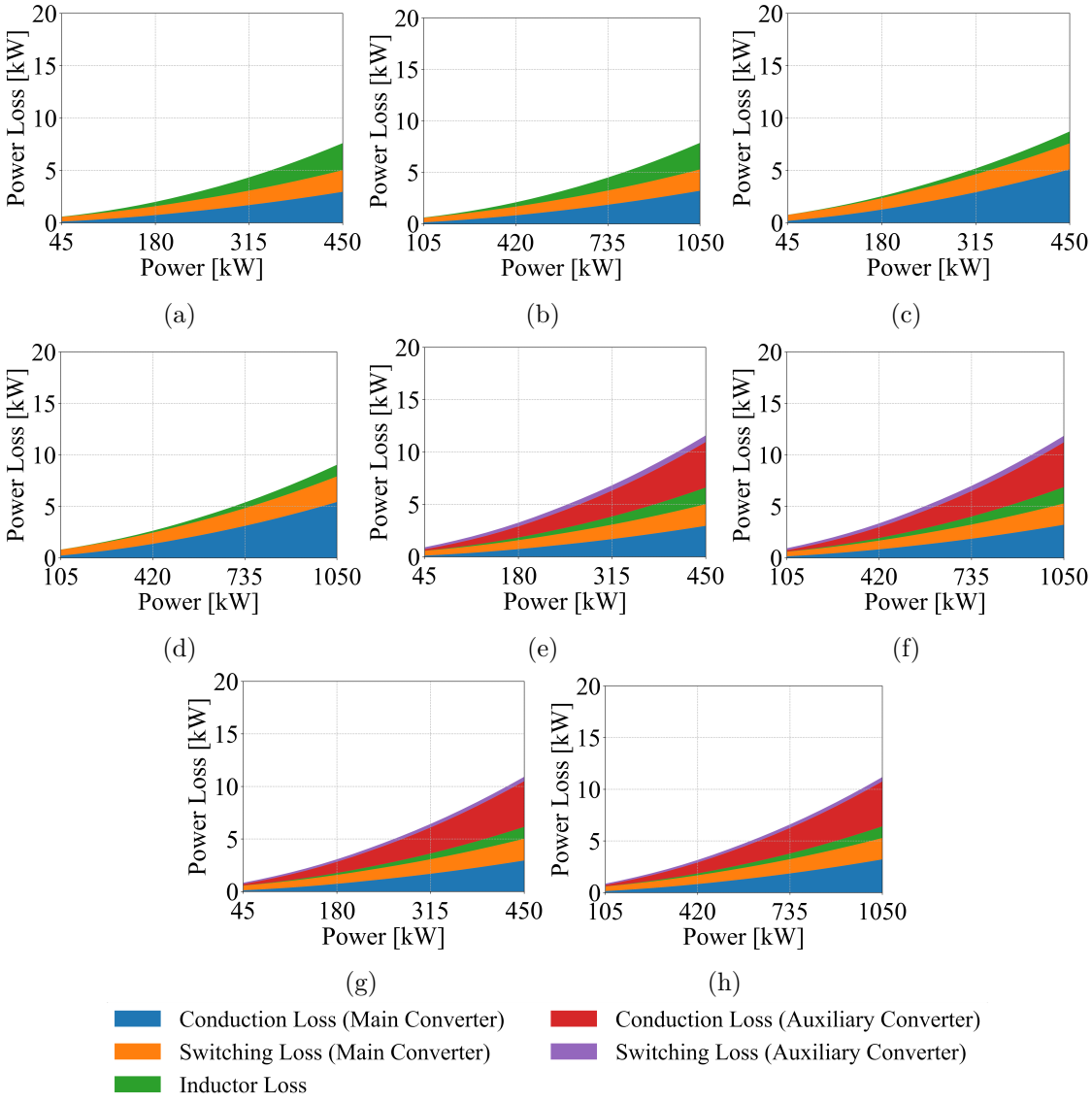

Figure 4.6: Loss breakdown of (a) CBC when $V_{dc2} = 0.45\,\text{kV}$, (b) CBC when $V_{dc2} = 1.05\,\text{kV}$, (c) TLFC-PS when $V_{dc2} = 0.45\,\text{kV}$, (d) TLFC-PS when $V_{dc2} = 1.05\,\text{kV}$, (e) BCSAC when $V_{dc2} = 0.45\,\text{kV}$, (f) BCSAC when $V_{dc2} = 1.05\,\text{kV}$, (g) BCSAC-PS when $V_{dc2} = 0.45\,\text{kV}$, (h) BCSAC-PS when $V_{dc2} = 1.05\,\text{kV}$.

Table 4.3: Comparison results between the BCSAC-PS, CBC, TLFC-PS, and BCSAC

Comparison	**BCSAC-PS**	**CBC**	**TLFC-PS**	**BCSAC**
Inductor volume	$24.94\,\text{dm}^3$	$66.09\,\text{dm}^3$	$24.94\,\text{dm}^3$	$40.73\,\text{dm}^3$
Chopper volume	$60.97\,\text{dm}^3$	$76.04\,\text{dm}^3$	$56.83\,\text{dm}^3$	$77.11\,\text{dm}^3$
Chopper mass	209.09 kg	350.79 kg	198.34 kg	267.93 kg
Power loss	11.04 kW	7.7 kW	8.9 kW	11.7 kW
Efficiency	97.4–99.3 %	98.1–99.6 %	97.6–99.4 %	97.2–99.3 %

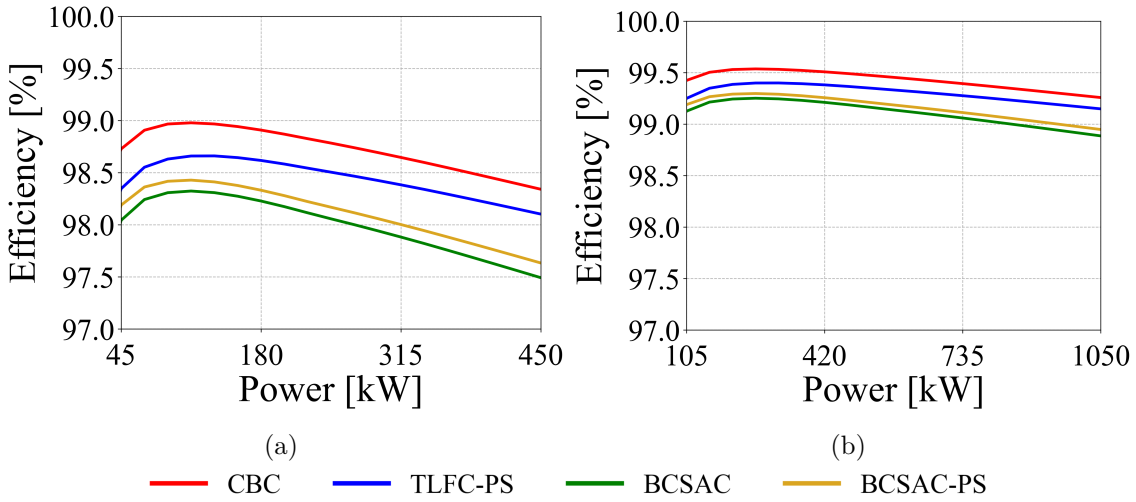

Figure 4.7: Efficiency of the four choppers when: (a) $V_{dc} = 0.45\,\text{kV}$ ($d_M = 0.3$), (b) $V_{dc} = 1.05\,\text{kV}$ ($d_M = 0.7$).

4.5 Experimental Results

To validate the result obtained from the theoretical analysis, an experiment is conducted using a down-scaled model in a controlled environment. This Chapter discusses the experimental result on the switching-ripple current of the BCSAC-PS.

4.5.1 Experimental Configuration and Conditions

The 2 kW down-scaled model of the BCSAC-PS used to conduct the experiment is the same as the one shown in Fig. 3.11, with the following set ups:

- The DC-voltage sources V_{dc1} and V_{dc2} are connected to either of DC-power supply KIKUSUI PAT160-50T or HEADSPRING biATLAS-5D525.
- The reference value for the DC-capacitor voltage is set to $V_C^* = 75\,\text{V}$.
- An air-core inductor with linear frequency characteristics is used, while the switching frequencies of the main and auxiliary converter are accordingly set to 5 kHz (i.e., $f_{SM} = f_{SA} = 5\,\text{kHz}$). Consequently, the actual inductance values are $L_{CBC} = 0.4\,\text{mH}$ for the CBC and $L_{BCSAC-PS} = 0.334\,\text{mH}$ for the BCSAC-PS.
- The reference values for the inductor current can be alternately set to positive and negative values. Positive current means that the power direction is from V_{dc1} to V_{dc2}, while negative current means the opposite.

- The controls of the BCSAC are achieved using a combination of Texas Instruments TMS320C6678 as the DSP and Altera Cyclone IV E EP4CE30F29C7 as the FPGA. The FPGA is used to generate the triangular carriers and to compare the duty ratios (i.e., d_M, d_{A1}, and d_{A2}) with the triangular carriers.

- The experimental waveforms are taken using Tektronix oscilloscope DPO4104B-L with a frequency band of 1 GHz. i_L is measured using the Tektronix current probe TCP0020 with a frequency band of 50 MHz, while v_M, v_A, v_L, and v_C are measured using the Tektronix high-voltage differential probes THDP0200 with a frequency band of 200 MHz.

Table 4.4: Parameters of the experiments

Parameter	**Description**	**Value**
$\boldsymbol{P}$	Rated power	2 kW
$\boldsymbol{V_{dc1}}$	DC-voltage source 1 (high-voltage side)	150 V
$\boldsymbol{V_{dc2}}$	DC-voltage source 2 (low-voltage side)	10 V–140 V
$\boldsymbol{L_{CBC}}$	Inductance of the CBC	0.4 mH
$\boldsymbol{L_{BCSAC-PS}}$	Inductance of the BCSAC-PS	0.334 mH
$\boldsymbol{C}$	Capacitance	0.4 mF
$\boldsymbol{V_C^*}$	DC-capacitor voltage	75 V
$\boldsymbol{f_{SM}}$	Switching frequency of the main converter	5 kHz
$\boldsymbol{f_{SA}}$	Switching frequency of the auxiliary converter	5 kHz

The parameters of the experiment is summarized in Table 4.4, where under $V_{dc1} = 150\,\text{V}$, $i_L^* = -10\,\text{A}$, and v_C is initially charged to 75 V. Negative current implies that the current flows from the low-voltage side to the high-voltage side. Meanwhile, V_{dc2} is gradually changed from 10–140 V to alter the d_M. The results of the theoretical switching-ripple current obtained from (3.78), (4.31), and (4.46), and the experimental switching-ripple current for the CBC and the BCSAC-PS based on the values of d_M under negative current are given in Fig. 4.8. The theoretical and experimental switching-ripple currents of the CBC are illustrated by the red line and black crosses, respectively, while those of the BCSAC-PS are illustrated by the gold line and blue crosses, respectively.

It can be seen from Fig. 4.8 that the experimental results agree well with the theoretical results for both choppers.It shows that the maximum experimental switching-ripple current for the CBC is 19.2 A (when $d_M = 0.49$), while that for the BCSAC-PS is around 5.4 A (when $d_M = 0.24$ or 0.74). In comparison, the maximum value for the theoretical ripple current of the BCSAC-PS obtained from (4.48) is 4.8 A. The reason why there are small

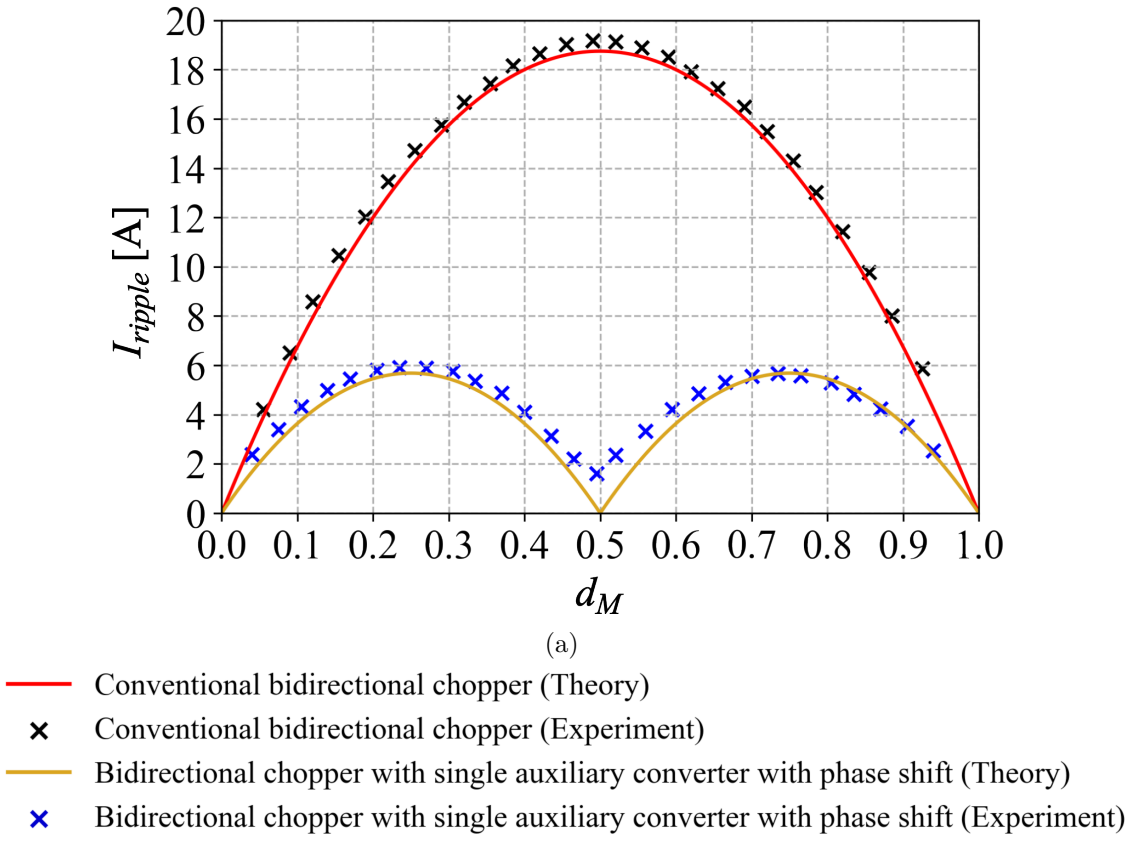

Figure 4.8: Theoretical and experimental ripple currents of CBC and BCSAC-PS under $V_{dc1} = 150\,\mathrm{V}$ and $i_L^* = -10\,\mathrm{A}$.

differences between the theoretical and experimental ripple currents for the BCSAC-PS is the omission of v_B^* in the theoretical analysis. This affects the calculation of d_M, which consequently affect the calculation of I_{ripple}. However, the differences are negligible if compared to the value of I_{ripple}.

4.6 Conclusion

This Chapter presents the evaluation of phase shift application to the carrier waves of the main and auxiliary converters in the bidirectional chopper with a single full-bridge auxiliary converter (BCSAC), which is intended to further reduce the switching-ripple current in the inductor. Theoretical analysis conducted on the switching-ripple current has shown that the BCSAC with phase shift (BCSAC-PS) is able to reduce the maximum switching-ripple current to $\frac{1}{4}$ of that the conventional bidirectional chopper (CBC), which is significantly lower than that produced by the BCSAC (i.e., $\frac{4}{9}$ of the CBC). Consequently, the inductor volume can be reduced by 62.3 % compared to the CBC, which is also 38.8 %

smaller than that of the BCSAC, where the reduction is comparable to that achieved by the TLFC with phase shift with phase shift (TLFC-PS). Overall, the BCSAC-PS is smaller in volume and lighter than the CBC and BCSAC, and comparable to the TLFC-PS. Further, loss analysis has shown that the BCSAC-PS can achieve high efficiency performances that are better than the BCSAC, even though it still produces slightly higher losses than the CBC and TLFC-PS. These results verify the advantage of phase shift application. Finally, experimental results using a 2 kW down-scaled model has verified the theoretical analysis results of the switching-ripple current in the BCSAC-PS.

Chapter 5

AC Component-Based Control Supplementary Application in BCSAC

This Chapter presents the supplementary application of AC component-based control to the BCSAC with phase shift (BCSAC-PS) to allow the achievement of the DC-capacitor voltage control when there is no power transfer between the voltage sources, which would improve the stability of the chopper operation. In this Chapter, the circuit configuration and operating principle of the modified BCSAC-PS are presented. The control methods based on DC and AC components, for both the main and auxiliary converters, are explained in details. Finally, the operations of the DC component-based control and the proposed AC component-based control in the BCSAC-PS during steady and transient states, along with the coordinated operation between the two control methods, are verified through experiments using a 2 kW down-scaled model.

5.1 Circuit Configuration and Operating Principles

The circuit configuration used in this Chapter is the same as that described in Chapter 4.1.1. It consists of a CBC as the main converter, an auxiliary converter, and an inductor. The power devices are controlled using PWM signals, where triangular carrier waveforms are applied to the main and auxiliary converters and the main converter carrier, $\mathrm{tri_M}$, lags the auxiliary converter carrier, $\mathrm{tri_A}$, by 90°. The other operating conditions

used in this Chapter are the same as those used in Chapter 3 and Chapter 4, i.e., the DC-capacitor voltage is set to be half of the DC-source voltage at the high voltage side (i.e., $V_C = \frac{V_{dc1}}{2}$), and the relationship $f_{SM} = f_{SA}$ holds, where f_{SM} indicates the frequency of $\mathrm{tri_M}$, while f_{SA} indicates the frequency of $\mathrm{tri_A}$. Finally, the operating principle of used in this Chapter is the same as that explained in Chapter 4.1.2, where the normalized $(v_A)_{ac}$ when $0 \leq d_M < 0.5$ is given by:

$$(v_A)_{ac} = \begin{cases} 0.5V_{dc1} & (\mathrm{S_1}\text{: ON, } \mathrm{S_2}\text{: OFF}) \\ -d_M V_{dc1} + \frac{{d_M}^2 - 0.5 d_M}{d_M - 1} V_{dc1} & (\mathrm{S_1}\text{: OFF, } \mathrm{S_2}\text{: ON}) \end{cases}. \tag{5.1}$$

Meanwhile, when $0.5 \leq d_M \leq 1$, it is given by:

$$(v_A)_{ac} = \begin{cases} (1 - d_M) V_{dc1} + \frac{{d_M}^2 - 1.5 d_M + 0.5}{d_M} V_{dc1} & (\mathrm{S_1}\text{: ON, } \mathrm{S_2}\text{: OFF}) \\ -0.5V_{dc1} & (\mathrm{S_1}\text{: OFF, } \mathrm{S_2}\text{: ON}) \end{cases}. \tag{5.2}$$

5.2 Control Method

Based on the components used, the control methods of the BCSAC-PS in this Chapter can be divided into DC component-based control and AC component-based control. The DC component-based control methods are similar to the ones presented in Chapter 3.3 and Chapter 4.2, and it is employed when the DC inductor current is not zero. In the DC component-based control, the DC-capacitor voltage control is performed by the main converter, while the auxiliary converter is used to achieve the inductor current control. On the other hand, the AC component-based control is employed when DC inductor current is zero. Different than the DC component-based control, in the AC component-based control, the inductor current control is performed by the main converter, while the auxiliary converter is used to achieve the DC-capacitor voltage control. However, different from Chapter 3.3 and Chapter 4.2, the inductor current control in this Chapter uses the average value of the actual DC current, which would improve the control accuracy and stability because the effect of switching-ripple component can be eliminated.

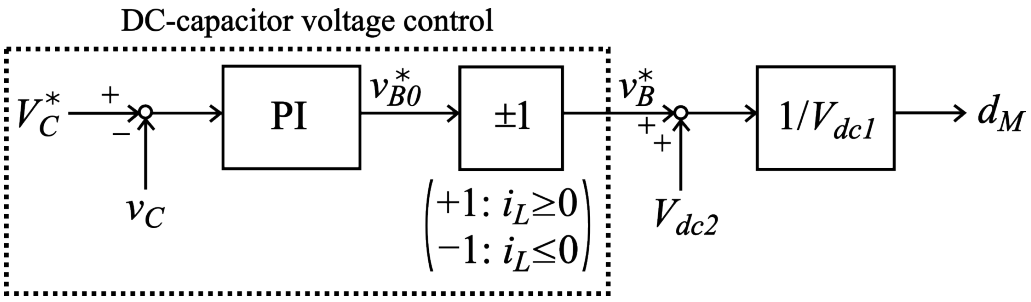

Figure 5.1: Block diagram of the main converter control using DC component-based control.

5.2.1 DC Component-Based Control

5.2.1.1 Main Converter Control

The block diagram of the main converter control using DC component-based control is shown in Fig. 5.1, where the objective is to regulate the DC-capacitor voltage. More specifically, the traditional PI control is applied to make the difference between the DC-capacitor voltage actual value, v_C, and its reference value, V_C^*, become zero, which generates the voltage reference v_{B0}^*. It should be noted that the polarity of v_{B0}^* is alternated based on that of the inductor current. For example, when $V_C^* > v_C$, the resulted v_B^* is as follows:

$$v_B^* = \begin{cases} v_{B0}^* & (i_L > 0) \\ -v_{B0}^* & (i_L < 0) \end{cases}. \tag{5.3}$$

Subsequently, V_{dc2} is added to v_B^* as a feedforward control, followed by the normalization by V_{dc1}. As a result, the duty ratio of S_1, d_M, with a maximum value of +1 and a minimum value of zero is produced, which can be expressed as:

$$d_M = \frac{v_B^* + V_{dc2}}{V_{dc1}}. \tag{5.4}$$

Finally, it is compared with $\mathrm{tri_M}$, which has the same maximum and minimum values. The detailed explanation on the principle of the DC-capacitor voltage control has been given in Chapter 3.3.1

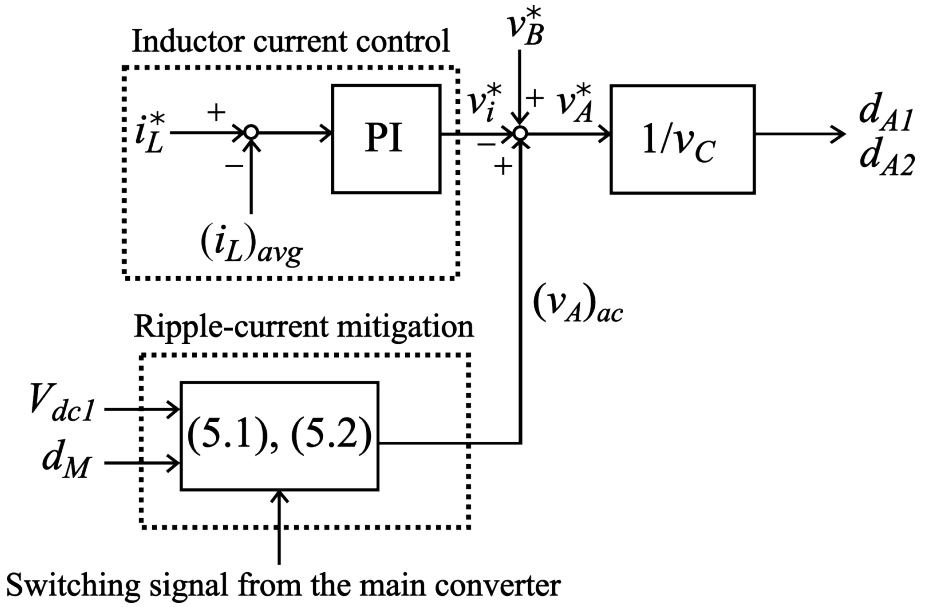

Figure 5.2: Block diagram of the auxiliary converter control using DC component-based control.

5.2.1.2 Auxiliary Converter Control

The block diagram of the auxiliary converter control using DC component-based control is shown in Fig. 5.2, where the objective is to regulate the DC inductor current and mitigate the ripple-current. In the DC inductor current control, the traditional PI control is used to make the difference between the its DC average value, $(i_L)_{avg}$, and its reference value, i_L^*, become zero. $(i_L)_{avg}$ is obtained by applying a moving-average filter with a frequency of f_{SM} to i_L, with the sampling frequency of $4f_{SM}$, where the sampling is done at the peaks and bottoms of $\mathrm{tri_M}$ and $\mathrm{tri_A}$. It should be noted that the time delay originating from the moving-average filter application of 5 kHz (= 200 µs) is much smaller than the response speed of the DC inductor current control (i.e., more than a few milliseconds). Thus, the effect of applying moving-average filter to the stability and dynamic response is negligible as long as f_{SM} is high enough. Subsequently, the voltage command v_i^* is generated. The difference between v_i^* and the voltage reference v_B^* produced in the main converter control has been explained in Chapter 3.3.2. Further, $(v_A)_{ac}$ coming from the ripple-current mitigation control that is obtained from (5.1) and (5.2), together with the voltage reference v_B^*, are added to v_i^* as a feedforward control. It produces the voltage reference of the auxiliary converter, v_A^*, which is followed by the normalization by v_C. As a result, the duty ratio of $\mathrm{S_3}$, d_{A1}, and that of $\mathrm{S_5}$, d_{A2}, with a maximum value of +1 and a minimum value of −1 are produced. Considering the application of unipolar PWM in

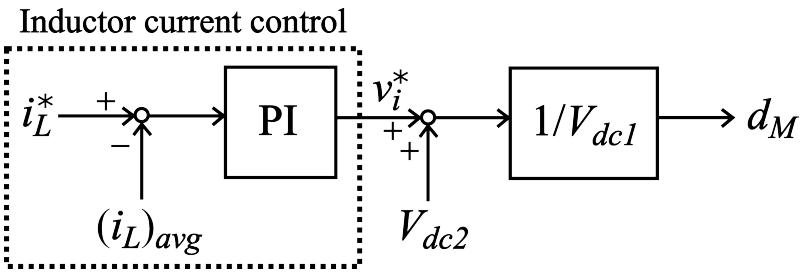

Figure 5.3: Block diagram of the main converter control using AC component-based control.

the auxiliary converter, the duty ratios d_{A1} and d_{A2} can be expressed as:

$$d_{A1} = \frac{-v_i^* + v_B^* + (v_A)_{ac}}{v_C} \tag{5.5}$$

$$d_{A2} = \frac{v_i^* - v_B^* - (v_A)_{ac}}{v_C}. \tag{5.6}$$

However, the d_{A1} and d_{A2} have to be further normalized to have a maximum value of $+1$ and a minimum value of zero. Finally, the newly obtained values of the d_{A1} and d_{A2} are compared with $\mathrm{tri_A}$, which has the same maximum and minimum values as them.

The traditional PI control is used in both converters, where the transfer functions in the Laplace domain for the DC-capacitor voltage and inductor current controls are given as:

$$\frac{v_C}{V_C^*} = \frac{sK_{vp-dc}i_L + K_{vi-dc}i_L}{(v_C)_{dc}Cs^2 + sK_{vp-dc}i_L + K_{vi-dc}i_L} \tag{5.7}$$

$$\frac{i_L}{i_L^*} = \frac{sK_{ip-dc} + K_{ii-dc}}{Ls^2 + sK_{ip-dc} + K_{ii-dc}}. \tag{5.8}$$

where C shows the capacitance value of the DC-capacitor and $(v_C)_{dc}$ shows the DC component of the DC-capacitor voltage. K_{vp-dc} and K_{vi-dc} show the proportional and integral gains of the DC-capacitor voltage control in the DC component-based control, while K_{ip-dc} and K_{ii-dc} show those of the inductor current control, and their values are appropriately set. It is evident from (5.7) that stable control of the DC-capacitor voltage cannot be achieved when $i_L = 0\,\mathrm{A}$.

5.2.2 AC Component-Based Control

5.2.2.1 Main Converter Control

The block diagram of the main converter control using AC component-based control is shown in Fig. 5.3, where the objective is to regulate the DC inductor current. The traditional PI control is applied to make the difference between the average (i.e., dc) inductor current value, $(i_L)_{avg}$, and its reference value, i_L^*, become zero, which generates the voltage command v_i^*. Subsequently, V_{dc2} is added to v_i^* as a feedforward control, followed by the normalization by V_{dc1}. As a result, the duty ratio of S_1, d_M, with a maximum value of $+1$ and a minimum value of zero is produced, which can be expressed as:

$$d_M = \frac{v_i^* + V_{dc2}}{V_{dc1}}. \tag{5.9}$$

Finally, it is compared with tri_M, which has the same maximum and minimum values.

5.2.2.2 Auxiliary Converter Control

The block diagram of the auxiliary converter control using AC component-based control is shown in Fig. 5.4a, where the AC inductor current with a frequency of f_{SM} is intentionally controlled to achieve the DC-capacitor voltage control in the chopper. In the current control, the traditional PI control is used to make the difference between the DC-capacitor voltage actual value, v_C, and its reference value, V_C^*, become zero, which generates the voltage reference v_{B0}^*. Its polarity (i.e., v_B^*) is changed based on the triangular carrier waveform of the auxiliary converter, tri_A. Subsequently, $(v_A)_{ac}$ coming from the ripple-current mitigation control that is obtained from (5.1) and (5.2) is added to v_B^* as a feedforward control to produce the voltage reference of the auxiliary converter, v_A^*, followed by the normalization by v_C. As a result, the duty ratio of S_3, d_{A1}, and that of S_5, d_{A2}, with a maximum value of $+1$ and a minimum value of -1 are produced. However, the d_{A1} and d_{A2} have to be further normalized to have a maximum value of $+1$ and a minimum value of zero. Finally, the newly obtained values of the d_{A1} and d_{A2} are compared with tri_A, which has the same maximum and minimum values as them.

Meanwhile, the transfer functions in the Laplace domain of the traditional PI control for the DC-capacitor voltage and inductor current controls using AC component-based

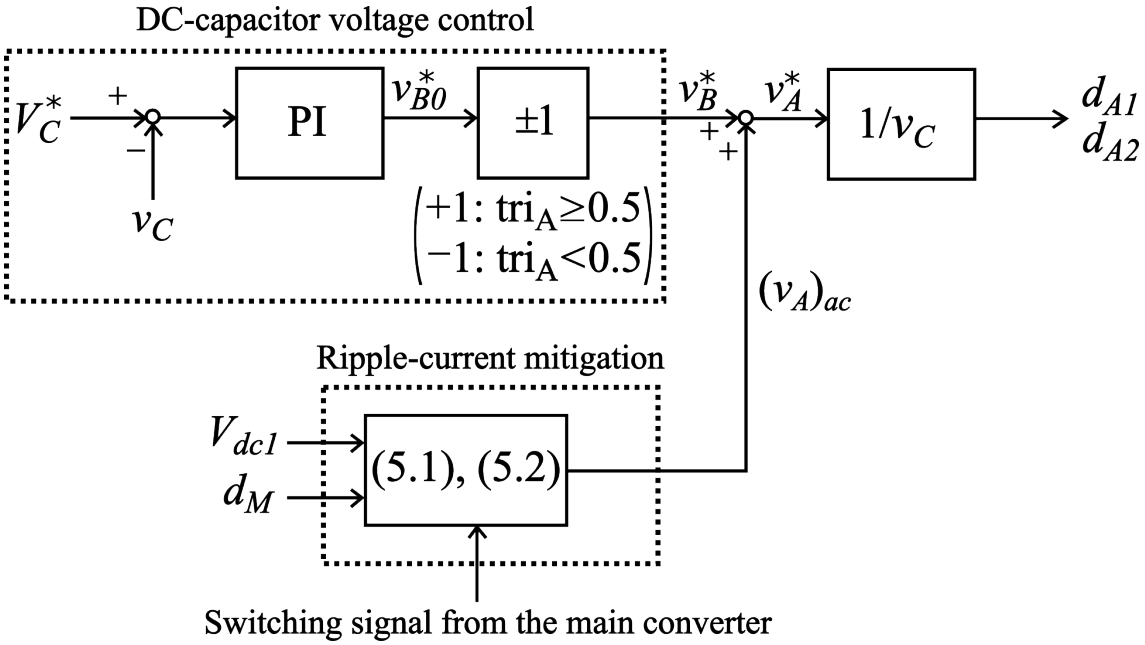

(a)

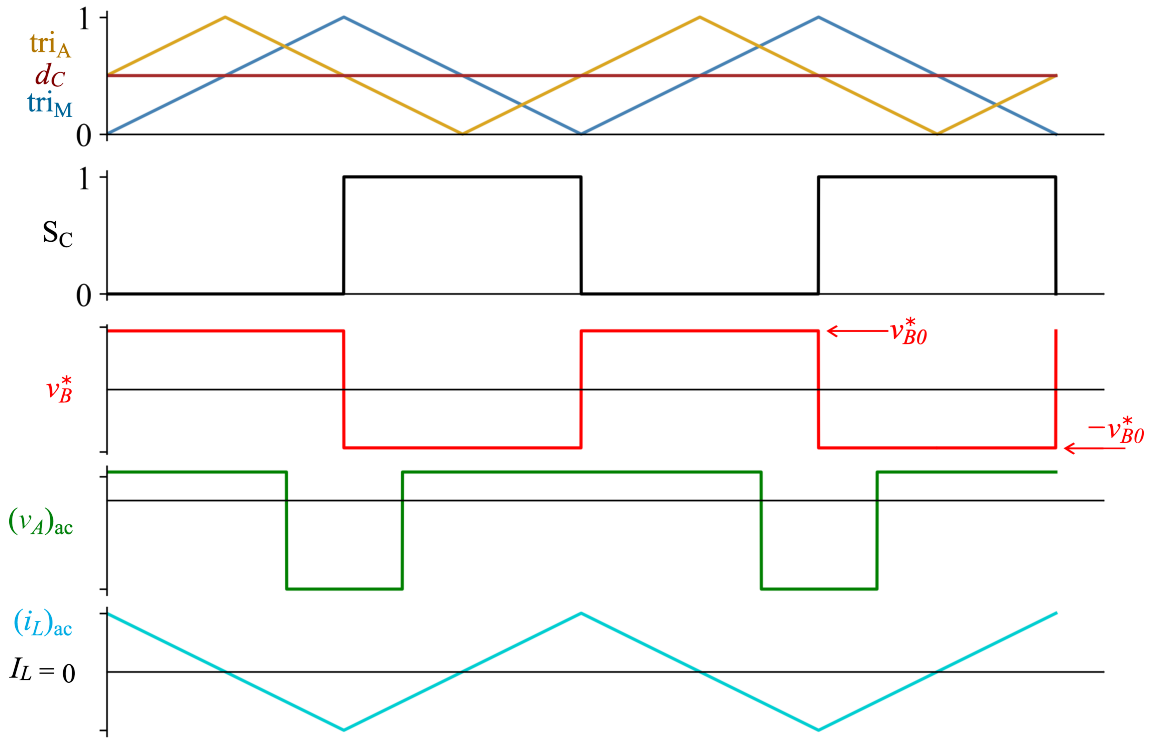

(b)

Figure 5.4: The auxiliary converter control using AC component-based control: (a) Block diagram, (b) Ideal waveforms when $V_C^* > v_C$ and only frequency component f_{SM} is assumed in $(i_L)_{ac}$.

control are given as:

$$\frac{i_L}{i_L^*} = \frac{sK_{ip-ac} + K_{ii-ac}}{Ls^2 + sK_{ip-ac} + K_{ii-ac}} \tag{5.10}$$

$$\frac{v_C}{V_C^*} = \frac{sK_{vp-ac}Y + K_{vi-ac}Y}{(v_C)_{dc}Cs^2 + sK_{vp-ac}Y + K_{vi-ac}Y}. \tag{5.11}$$

where C shows the capacitance value of the DC-capacitor, Y shows a constant produced from $(v_A)_{ac}$ and $(i_L)_{ac}$, and $(v_C)_{dc}$ shows the DC component of the DC-capacitor voltage. K_{vp-ac} and K_{vi-ac} show the proportional and integral gains of the DC-capacitor voltage control in the AC component-based control, while K_{ip-ac} and K_{ii-ac} show those of the inductor current control. It is evident from (5.11) that the DC-capacitor voltage control can be achieved regardless of the value of i_L. Thus, the supplementary application of AC component-based control can contribute to the stability improvement of the BCSAC-PSoperation when $i_L = 0\,\mathrm{A}$.

To give a clearer image on v_B^* polarity, the ideal waveforms when $V_C^* > v_C$ is shown in Fig. 5.4b, where $(i_L)_{ac}$ is the AC current included in i_L that contains only the f_{SM} frequency component produced by v_B^*. Let $\mathrm{S_C}$ given in Fig. 5.4b be the PWM signal produced from the comparison of $\mathrm{tri_A}$ with a duty ratio $d_C = 0.5$. Specifically, $\mathrm{S_C} = 1$ when $\mathrm{tri_A} < d_C$ and $\mathrm{S_C} = 0$ when $\mathrm{tri_A} \geq d_C$. Based on $\mathrm{S_C}$, v_B^* is given by:

$$v_B^* = \begin{cases} -v_{B0}^* & (\mathrm{S_C}\colon 1) \\ v_{B0}^* & (\mathrm{S_C}\colon 0) \end{cases}, \tag{5.12}$$

where v_{B0}^* is the output of the PI control. Subsequently, based on Fig. 5.4b and (5.12), v_A^* can be determined by:

$$v_A^* = \begin{cases} -v_B^* + (v_A)_{ac} & (\mathrm{tri_A} < d_C) \\ v_B^* + (v_A)_{ac} & (\mathrm{tri_A} \geq d_C) \end{cases}. \tag{5.13}$$

Consequently, the duty ratios d_{A1} and d_{A2} can be expressed as:

$$d_{A1} = \begin{cases} \frac{-v_B^* + (v_A)_{ac}}{v_C} & (\text{tri}_\text{A} < d_C) \\ \frac{v_B^* + (v_A)_{ac}}{v_C} & (\text{tri}_\text{A} \geq d_C) \end{cases} \tag{5.14}$$

$$d_{A2} = \begin{cases} \frac{v_B^* - (v_A)_{ac}}{v_C} & (\text{tri}_\text{A} < d_C) \\ \frac{-v_B^* - (v_A)_{ac}}{v_C} & (\text{tri}_\text{A} \geq d_C) \end{cases}. \tag{5.15}$$

To further explain the DC-capacitor voltage control, the relationship $V_C^* > v_C$ is assumed in the auxiliary converter. It should also be noted that $(i_L)_{ac}$, which is a triangular waveform with only the frequency component of f_{SM} produced by v_B^*, can be either in phase or out of phase with $(v_A)_{ac}$, depending on the relationship between V_C^* and v_C. Based on Fig. 5.4a, a positive v_{B0}^* is generated when the relationship $V_C^* > v_C$ holds. Consequently, $(i_L)_{ac}$ that is in phase with $(v_A)_{ac}$ is produced, as shown in Fig. 5.4b. As a result, a positive power $(v_A)_{ac}(i_L)_{ac}$ is formed, which flows into the capacitor and increases v_C.

5.3 Experimental Results

To verify the performance and operation of the DC component- and AC component-based controls in the BCSAC-PS, experiments are conducted using a down-scaled model in a controlled environment. This Chapter discusses the experimental results of the steady- and transient-state operations under the DC component- and AC component-based controls.

5.3.1 Experimental Configuration and Conditions

The 2 kW down-scaled model of the BCSAC-PS used to conduct the experiment is the same as the one shown in Fig. 3.11, with the same set ups used in Chapter 4.5. The following experiments are carried out using the down-scaled model with both the DC and AC component-based controls under the experimental parameters listed in Table 5.1:

DC Component-Based Control

1. Steady-state operation when $V_{dc1} = 150\,\text{V}$, $V_{dc2} = 65\,\text{V}$, $i_L^* = -10\,\text{A}$, and v_C is initially charged to 75 V.

2. Transient behavior during the initial charging of v_C from 0 V to 75 V, where $i_L^* = -20$ A.

3. Transient behavior during the step change of V_{dc1} from 150 V to 140 V, where $i_L^* = -20$ A.

AC Component-Based Control

1. Steady-state operation when $V_{dc1} = 150$ V, $V_{dc2} = 75$ V, $i_L^* = 0$ A, and v_C is initially charged to 75 V.

2. Transient behavior during the initial charging of v_C from 0 V to 75 V, where $i_L^* = 0$ A.

3. Transient behavior during the ramp change of v_C from 75 V to 85 V and then 85 V to 75 V, where $i_L^* = 0$ A.

Coordinated Control

1. Transient behavior during the ramp change of i_L from 0 A to -10 A and then -10 A to 0 A, where both AC and DC component-based controls are used.

Table 5.1: Parameters of the experiments

Parameter	Description	Value
$\boldsymbol{P}$	Rated power	2 kW
$\boldsymbol{V_{dc1}}$	DC-voltage source 1 (high-voltage side)	150 V
$\boldsymbol{L_{CBC}}$	Inductance of the CBC	0.4 mH
$\boldsymbol{L_{BCSAC-PS}}$	Inductance of the BCSAC-PS	0.334 mH
$\boldsymbol{C}$	Capacitance	0.4 mF
$\boldsymbol{V_C^*}$	DC-capacitor voltage	75 V
$\boldsymbol{f_{SM}}$	Switching frequency of the main converter	5 kHz
$\boldsymbol{f_{SA}}$	Switching frequency of the auxiliary converter	5 kHz

5.3.2 DC Component-Based Control

5.3.2.1 Operation under Steady-State

The steady-state experimental waveforms of the BCSAC-PS using DC component-based control under $V_{dc1} = 150$ V, $V_{dc2} = 65$ V, and $i_L^* = -10$ A are given in Fig. 5.5. Negative current implies that the current flows from the low-voltage side to the high-voltage side. The main converter voltage, v_M, is a rectangular wave with DC and AC components, which

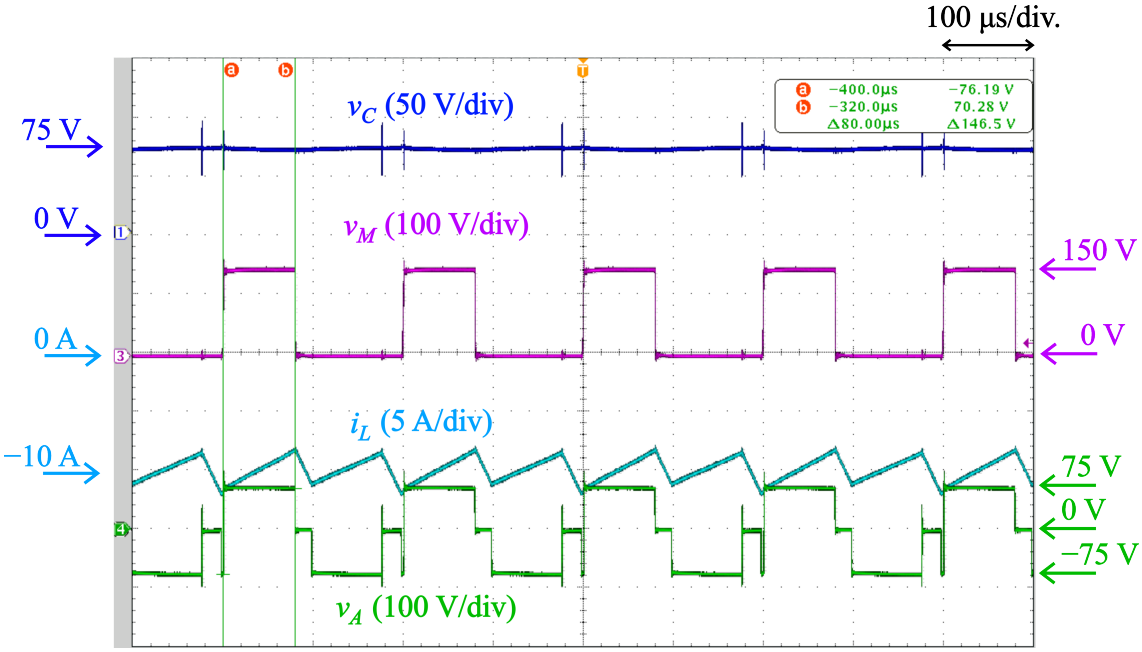

Figure 5.5: Experimental waveforms for the steady-state operation of the BCSAC-PS using DC component-based control under $V_{dc1} = 150\,\text{V}$, $V_{dc2} = 65\,\text{V}$, and $i_L^* = -10\,\text{A}$.

alternates between V_{dc1} ($= 150\,\text{V}$) and 0. Further, d_M is indicated to be 0.4, which is lower than the theoretical value of 0.43 obtained from (4.9). The small difference between the experimental and theoretical results is due to the existence of v_B^* in the main converter control shown in Fig. 5.1. Meanwhile, the auxiliary converter voltage, v_A, alternates between $-V_C$ ($= -75\,\text{V}$), 0, and V_C ($= 75\,\text{V}$).

From Fig. 5.5, the DC-capacitor voltage, v_C, can be regulated at $75\,\text{V}$ ($= \frac{V_{dc1}}{2}$) with no steady-state error. Similarly, the DC inductor current, $(i_L)_{avg}$, can be regulated to its reference value at $-10\,\text{A}$ with no steady-state error. Further, the ripple current of i_L is shown to be $4.1\,\text{A}$, which agrees well with the theoretical peak-to-peak ripple current for d_M in the range of $0 \leq d_M < 0.5$ obtained from (4.31) at $4.56\,\text{A}$. The small difference in the experimental and theoretical values for the ripple current is caused by the v_B^* in the main converter control.

5.3.2.2 Operation under Transient-State

The transient experimental waveforms during the initial charging procedure of the BCSAC-PS using DC component-based control under $V_{dc1} = 150\,\text{V}$ and $V_{dc2} = 85\,\text{V}$ are shown in Fig. 5.6. Since V_{dc1} is set as the high-voltage side, while V_{dc2} is the low-voltage side, V_{dc1} is used to charge the capacitor. To send the power from V_{dc1} to the capacitor, the full-bridge

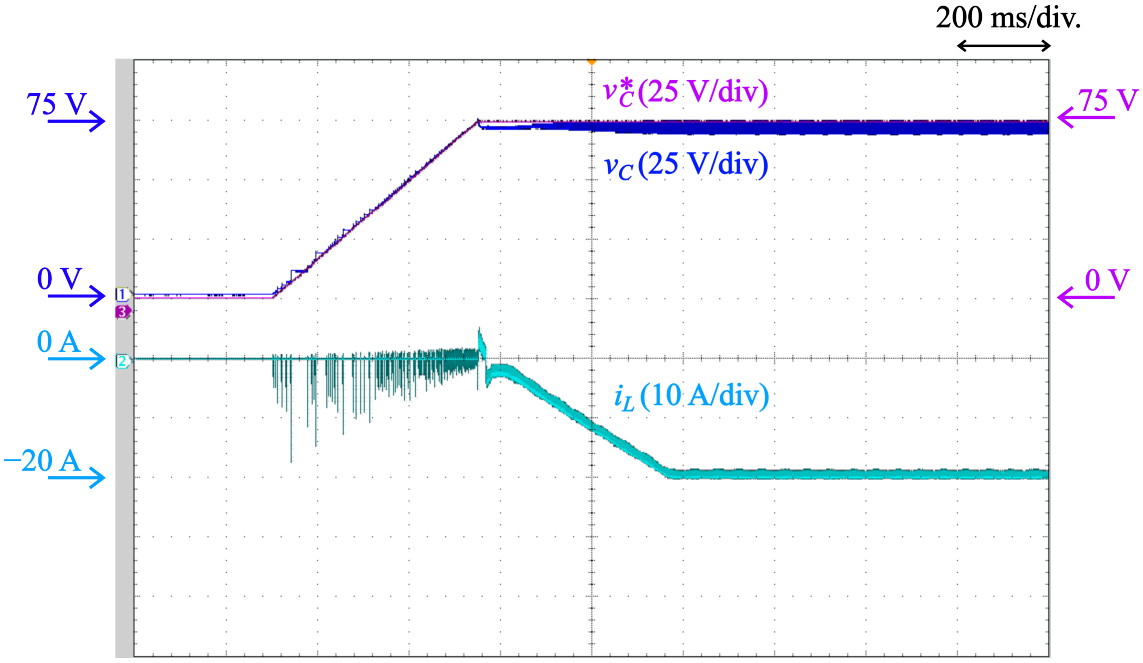

Figure 5.6: Experimental waveforms using DC component-based control during the initial charging procedure of the BCSAC-PS under $V_{dc1} = 150\,\text{V}$ and $V_{dc2} = 85\,\text{V}$.

auxiliary converter is operated in charging mode during the initial state of the operation, where S_3 and S_6 are ON, while S_4 and S_5 are OFF. Meanwhile, in the main converter, S_2 is always OFF, and S_1 is controlled to charge the capacitor voltage, v_C. Specifically, the duty ratio of S_1, d_M, is determined using the traditional PI control to apply feedback control to the v_C, where v_C is changed from zero to 75 V in 400 ms. After v_C reaches 75 V, the BCSAC-PS operates normally, and i_L drops from zero to its reference value at −20 A in approximately 400 ms. It can be seen from Fig. 5.6 that the initial charging procedure using DC component-based control can be completed with neither overvoltage nor overcurrent occuring in the process.

The transient experimental waveforms during a step change in the V_{dc1} of the BCSAC-PS using DC component-based control under $V_{dc2} = 10\,\text{V}$ and $i_L^* = -20\,\text{A}$ are shown in Fig. 5.7. It can be seen that V_{dc1} changes from 150 V to 140 V in approximately 40 ms with no overvoltage. There is a slight jump in the inductor current, i_L, at the initial part of the step change. This is because the decrease in V_{dc1} inversely affects the inductor voltage, v_L. The step change also produces higher d_M, which ultimately results in increased ripple current. Meanwhile, the DC-capacitor voltage, v_C, can be stably regulated with no error during the transient state (i.e., step change).

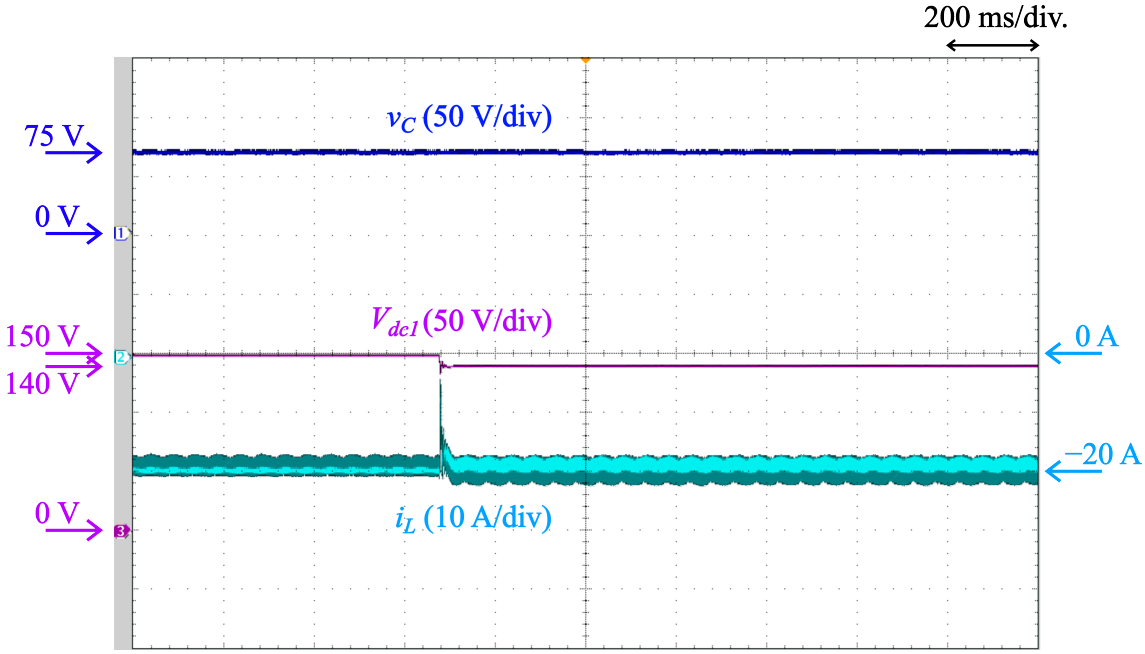

Figure 5.7: Experimental waveform during a step change in the V_{dc1} from 150 V to 140 V of the BCSAC-PS under $V_{dc2} = 10$ V and $i_L^* = -20$ A.

5.3.3 AC Component-Based Control

5.3.3.1 Operation under Steady-State

The steady-state experimental waveforms of the BCSAC-PS using AC component-based control under $V_{dc1} = 150$ V, $V_{dc2} = 75$ V, and $i_L^* = 0$ A are given in Fig. 5.8. The main converter voltage, v_M, is a rectangular wave with AC and AC components, which alternates between V_{dc1} (= 150 V) and 0. Further, d_M is indicated to be 0.48, which is lower than the theoretical value of 0.5 obtained from (4.9). The small difference between the experimental and theoretical results is due to the existence of v_i^* in the main converter control shown in Fig. 5.3. Meanwhile, the auxiliary converter voltage, v_A, alternates between $-V_C$ (= −75 V), 0, and V_C (= 75 V).

From Fig. 5.8, the DC-capacitor voltage, v_C, can be regulated at 75 V (= $\frac{V_{dc1}}{2}$) with no steady-state error. Similarly, the DC inductor current, $(i_L)_{avg}$, can be regulated to its reference value at 0 A with no steady-state error.

5.3.3.2 Operation under Transient-State

The transient experimental waveforms during the initial charging procedure of the BCSAC-PS using AC component-based control under $V_{dc1} = 150$ V and $V_{dc2} = 75$ V are shown in

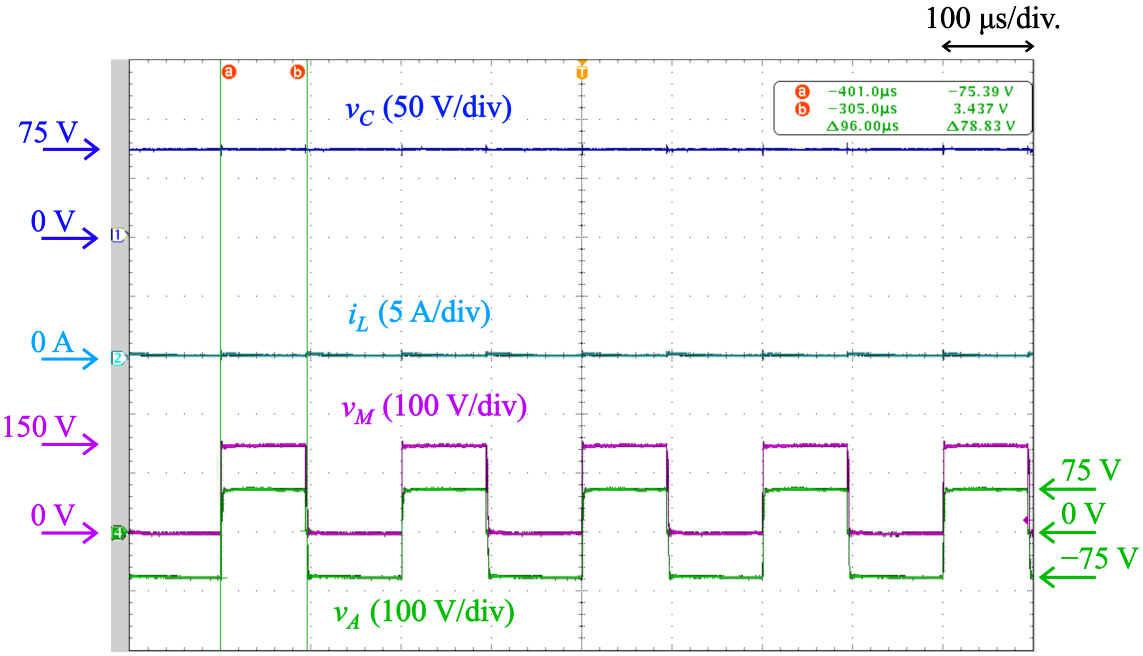

Figure 5.8: Experimental waveforms for the steady-state operation of the BCSAC-PS using AC component-based control under $V_{dc1} = 150\,\text{V}$, $V_{dc2} = 75\,\text{V}$, and $i_L^* = 0\,\text{A}$.

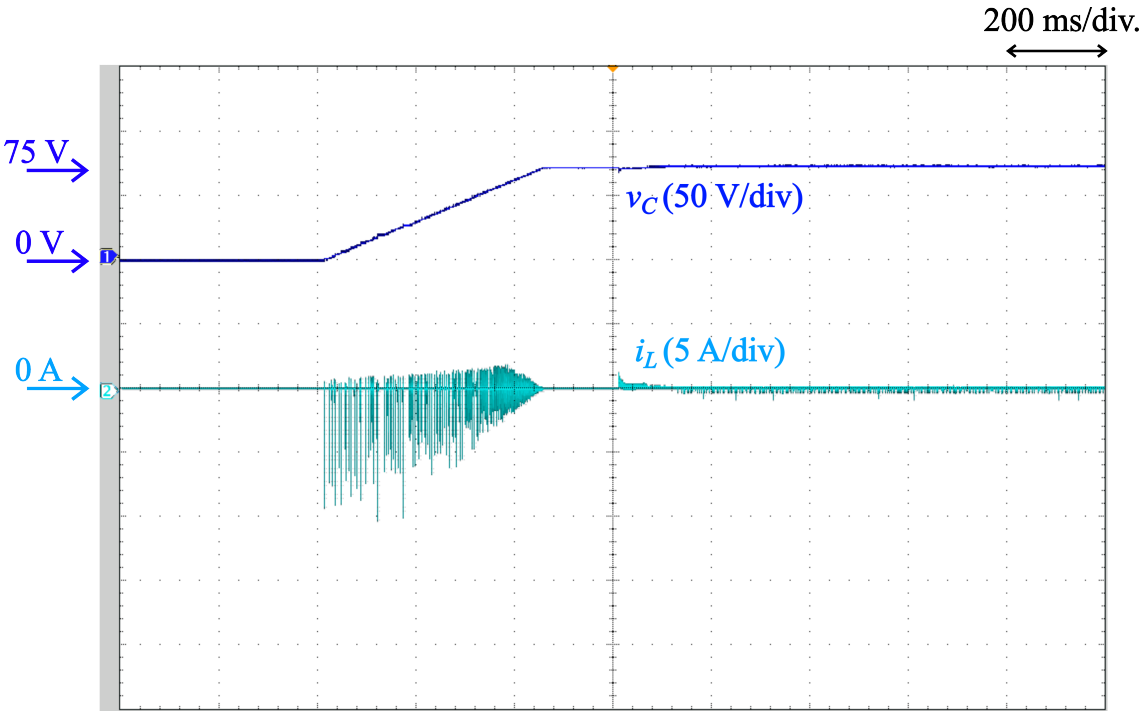

Figure 5.9: Experimental waveforms using AC component-based control during the initial charging procedure of the BCSAC-PS under $V_{dc1} = 150\,\text{V}$ and $V_{dc2} = 75\,\text{V}$.

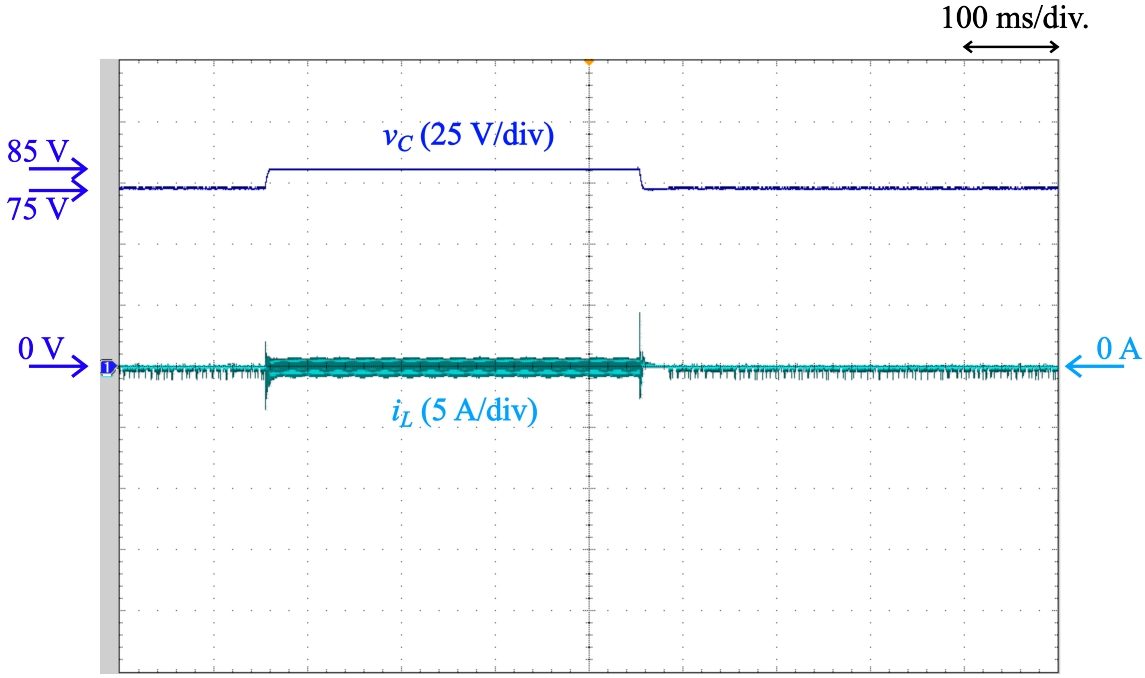

Figure 5.10: Experimental waveform during a ramp change in the v_C from 75 V to 85 V and then from 85 V to 75 V of the BCSAC-PS under $V_{dc1} = 150$ V, $V_{dc2} = 75$ V, and $i_L^* = 0$ A.

Fig. 5.9. Similarly, the full-bridge auxiliary converter is operated in charging mode during the initial state of the operation to send the power from V_{dc1} to the capacitor, where S_3 and S_6 are ON, while S_4 and S_5 are OFF. Meanwhile, in the main converter, S_2 is always OFF, and S_1 is controlled to charge the capacitor voltage, v_C. Specifically, the duty ratio of S_1, d_M, is determined using the traditional PI control to apply feedback control to the i_L, where v_C is changed from zero to 75 V in 450 ms to achieve the control of i_L at 0 A. It can be seen from Fig. 5.9 that the initial charging procedure using AC component-based control can be completed with neither overvoltage nor overcurrent occuring in the process.

The transient experimental waveforms during a ramp change in the v_C of the BCSAC-PS using AC component-based control under $V_{dc1} = 150$ V, $V_{dc2} = 75$ V, and $i_L^* = -20$ A are shown in Fig. 5.10. It can be seen that v_C is able to rise from 75 V to 85 V and drop from 85 V to 75 V with no overvoltage and undervoltage, meaning that the DC-capacitor voltage control based on the AC component-based control is valid. Additionally, the inductor current, i_L, can be stably regulated during the transient state (i.e., ramp change), with the observed increase in the ripple current. This is caused by the effect of the change in v_C on v_L.

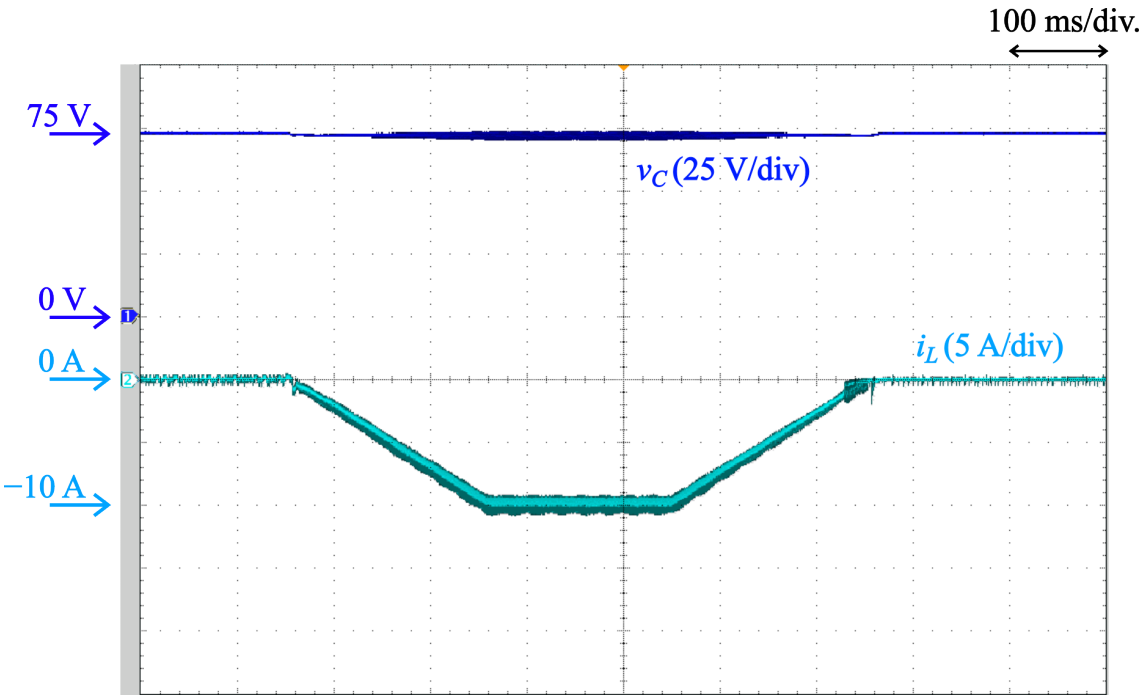

Figure 5.11: Experimental waveform of coordinated operation between the AC and DC component-based controls under $V_{dc1} = 150\,\text{V}$ and $V_{dc2} = 75\,\text{V}$, where there is a ramp change in the i_L from $0\,\text{A}$ to $-10\,\text{A}$ and then from $-10\,\text{A}$ to $0\,\text{A}$.

5.3.4 Coordinated Control

The transient experimental waveforms of the BCSAC-PS during a ramp change in the i_L under $V_{dc1} = 150$ V and $V_{dc2} = 75$ V using a coordination of both AC and AC component-based controls are shown in Fig. 5.11, where the AC component-based control is applied when $i_L = 0\,\text{A}$ and the DC component-based control is applied when $i_L \neq 0\,\text{A}$. It shows that i_L is able to decrease from $0\,\text{A}$ to $-10\,\text{A}$ in $200\,\text{ms}$, and increase from $-10\,\text{A}$ to $0\,\text{A}$ in $200\,\text{ms}$, with no overcurrent and undercurrent. Further, the DC-capacitor voltage can be stably regulated using the AC component-based control when $i_L = 0\,\text{A}$ and DC component-based control when $i_L = -10\,\text{A}$. This shows that the two control methods can operated in coordination.

5.4 Conclusion

This Chapter presents the supplementary application of AC component-based control in the BCSAC with phase shift (BCSAC-PS) to allow the achievement of the DC-capacitor voltage control when there is no power transfer between the voltage sources, which would improve the stability of the chopper operation. Experimental results using a $2\,\text{kW}$ down-

scaled model has verified the operations and controls of the BCSAC-PS during the steady and transient states. In the steady state, the inductor current and DC-capacitor voltage can be regulated to their respective reference values with no steady-state error, where the DC component-based control is used when the DC inductor current is not zero and AC component-based control is used when the DC inductor current is zero. In the transient state, the initial charging of v_C can be completed using both the DC component- and AC component-based controls without any overvoltage or overcurrent problem. Additionally, the DC component-based control can stably operate during a step change of V_{dc1}, while the AC component-based control can stably operate during a ramp change of v_C, without any overvoltage and undervoltage problem. Finally, the two control methods can be smoothly operated in coordination during a step change of i_L.

Chapter 6

Conclusion and Future Work

6.1 Conclusion

This dissertation has proposed a non-isolated bidirectional chopper topology for battery energy storage system (BESS) applications in electric railway systems. The proposed topology, the bidirectional chopper with a single full-bridge auxiliary converter (BCSAC), is composed of the conventional bidirectional chopper (CBC) as the main converter, a single-phase full-bridge converter equipped with a floating DC-capacitor as the auxiliary converter, and an inductor. It operates under the following conditions: 1) The switching frequencies of the main and auxiliary converters are the same, and 2) The DC-capacitor voltage is half of the DC-voltage-source voltage at the high-voltage side.

The BCSAC is able achieve a reduced switching-ripple current in the inductor, which consequently lowers its volume, while achieving high-efficiency performances. Theoretical analysis conducted on the switching-ripple current has shown that the BCSAC can reduce the switching-ripple current to $\frac{4}{9}$ of that the CBC. Additionally, based on the theoretical comparisons that have been made in this dissertation, the inductor volume can be reduced by 38.4 % and 10.5 % to those required by the CBC and three-level flying capacitor converter (TLFC). Overall, the BCSAC is smaller in volume than the BCAC and lighter than the CBC and TLFC. Even though the BCSAC produces slightly higher power losses than the CBC and TLFC, it is significantly lower than those produced by the bidirectional chopper with an auxiliary converter (BCAC) with three cells, meaning that high efficiency performances can be achieved. Further, experimental results using a 2 kW down-scaled model have validated the theoretical analysis results of the switching-ripple current, as

well as the operations and controls of the BCSAC in the steady state, under both positive and negative currents, and the transient state, during the initial charging procedure and under a step change in the DC-voltage-source voltage at the low-voltage side.

Phase shift application to the carrier waves of the BCSAC has been proposed to further reduce the produced switching-ripple current in the chopper. Theoretical analysis conducted on the switching-ripple current has shown that the BCSAC with phase shift (BCSAC-PS)can reduce the switching-ripple current to $\frac{1}{4}$ of that the CBC. Consequently, the BCSAC-PS enables the inductor volume to be reduced by 62.3 % compared to the CBC, which is also 38.8 % smaller than that of the BCSAC. Overall, the BCSAC-PS is smaller in volume and lighter than the CBC and BCSAC, and comparable to the TLFC with phase shift (TLFC-PS. Additionally, theoretical loss analysis has shown that the BCSAC-PS can achieve high efficiency performances that are better than the BCSAC, even though it still produces slightly higher losses than the CBC and TLFC-PS. Finally, experimental results using a 2 kW down-scaled model has verified the theoretical analysis results of the switching-ripple current.

Supplementary application of AC component-based control to the conventional DC component-based control has been proposed to improve the stability in the BCSAC-PS operation. It uses the AC component of the inductor current to achieve the DC-capacitor voltage control when there is no power transfer between the voltage sources (i.e., the DC inductor current is zero). The performances of the proposed control method under steady and transient states, along with its coordination with the conventional DC component-based control, have been validated through experiments using a 2 kW down-scaled model, where the AC component-based control is used when the DC inductor current is zero and the DC component-based control is used when the DC inductor current is not zero.

6.2 Future Research

Considering the limitation set in this research, there are several point of interests that can be addressed to form future research targets and improve the proposed chopper.

- **Reducing the produced power loss**. The total power loss produced by the BCSAC and BCSAC-PS in this dissertation is still comparatively higher than the conventional topologies like the CBC, TLFC, and TLFC-PS, albeit not significant.

Further power loss reduction is required to achieve performances with higher efficiency. It should be noted that according to the power loss analysis done in this dissertation, conduction loss is the main contributor to the power loss. Thus, measures to reduce conduction loss, especially in the auxiliary converter, need to be considered. For example, using a variation of capacitor voltage instead of a fixed value may be one potential solution. Additionally, other measures to reduce loss like applying soft switching techniques may be interesting to look into.

- **Conducting experiments using full-scale setups and cost analysis**. The experiments done in this dissertation are conducted using a 2 kW down-scaled model. which comes with several limitations that could affect the produced power loss. Thus, comparisons on power loss and efficiency in this dissertation are theoretically done based on parameters used in real applications. It is necessary to validate the theoretical comparison results by comparing it with the experimental results. Further, cost analysis should be conducted since it is a major consideration for real applications.

- **Fault-tolerant operation in the chopper**. It is necessary to consider the mitigation measures to when a fault occurs in the auxiliary converter, especially since only a single full-bridge cell is used in the BCSAC.

Appendix A

Comparison of Different Settings of the Capacitor Voltage

In the BCSAC, the DC-capacitor voltage in the auxiliary converter is set to be half of the DC- voltage source voltage at the high-voltage side (i.e., $V_C = \frac{V_{dc1}}{2}$). To verify the advantage of this setting, comparison with $V_C = \frac{V_{dc1}}{3}$ and $V_C = \frac{V_{dc1}}{4}$, with respect to the produced switching-ripple current, power loss, and efficiency is conducted.

A.1 Switching-Ripple Current

Theoretical analysis on the switching-ripple current for the BCSAC under $V_C = \frac{V_{dc1}}{3}$ and $V_C = \frac{V_{dc1}}{4}$ is similarly conducted as in Chapter 3.4 and Chapter 4.3, while the voltage compensation on v_A given in Chapter 3.2.2 should be modified depending on the value of V_C. Based on the analysis results, the switching-ripple current of the BCSAC under $V_C = \frac{V_{dc1}}{3}$ for d_M in the range of $0 \leq d_M < 0.5$ can be determined as:

$$I_{ripple} = \frac{V_{dc1}}{f_{SM} L} \left(\frac{2}{3} - d_M \right) d_M, \tag{A.1}$$

and that for d_M in the range of $0.5 \leq d_M \leq 1$ can be determined as:

$$I_{ripple} = \frac{V_{dc1}}{f_{SM} L} \left(d_M - \frac{1}{3} \right) (1 - d_M). \tag{A.2}$$

Based on (A.1) and (A.1), the $(I_{ripple})_{max}$ of the BCSAC under $V_C = \frac{V_{dc1}}{3}$ is obtained when $d_M = \frac{1}{3}$ and $d_M = \frac{2}{3}$, which is equivalent to:

$$(I_{ripple})_{max} = \frac{V_{dc1}}{9 f_{SM} L}. \tag{A.3}$$

Meanwhile, the switching-ripple current of the BCSAC under $V_C = \frac{V_{dc1}}{4}$ for d_M in the range of $0 \leq d_M < 0.5$ can be determined as:

$$I_{ripple} = \frac{V_{dc1}}{f_{SM} L} \left(\frac{3}{4} - d_M \right) d_M, \tag{A.4}$$

and that for d_M in the range of $0.5 \leq d_M \leq 1$ can be determined as:

$$I_{ripple} = \frac{V_{dc1}}{f_{SM} L} \left(d_M - \frac{1}{4} \right) (1 - d_M). \tag{A.5}$$

Based on (A.4) and (A.5), the $(I_{ripple})_{max}$ of the BCSAC under $V_C = \frac{V_{dc1}}{3}$ is obtained when $d_M = \frac{3}{8}$ and $d_M = \frac{5}{8}$, which is equivalent to:

$$(I_{ripple})_{max} = \frac{9 V_{dc1}}{64 f_{SM} L}. \tag{A.6}$$

Based on (A.3), the BCSAC under $V_C = \frac{V_{dc1}}{3}$ is able to reduce to reduce the switching-ripple current to $\frac{4}{9}$ of that produced by the CBC, which is comparable to that achieved by the BCSAC under $V_C = \frac{V_{dc1}}{2}$. Meanwhile, based on (A.6) the BCSAC under $V_C = \frac{V_{dc1}}{4}$ is able to reduce to reduce the switching-ripple current to $\frac{9}{16}$ of that produced by the CBC, which is higher than that achieved by the BCSAC under $V_C = \frac{V_{dc1}}{2}$. Fig. A.1 shows the theoretical results for the switching-ripple current of the BCSAC under $V_C = \frac{V_{dc1}}{2}$ (green line), BCSAC under $V_C = \frac{V_{dc1}}{3}$ (purple line), BCSAC under $V_C = \frac{V_{dc1}}{4}$ (orange line), and CBC (red line) under d_M in the range of $0 \leq d_M \leq 1$. It shows that there is a symmetry in the switching-ripple current of the BCSAC under $V_C = \frac{V_{dc1}}{3}$ and $V_C = \frac{V_{dc1}}{4}$, similar to that of the BCSAC under $V_C = \frac{V_{dc1}}{2}$. However, the advantage shown by the BCSAC under $V_C = \frac{V_{dc1}}{3}$ and $V_C = \frac{V_{dc1}}{4}$, particularly when the operating duty ratio is around $d_M = 0.5$, is not as apparent as that shown by the BCSAC under $V_C = \frac{V_{dc1}}{2}$. This is because there still remains the frequency component f_{SM} in the inductor current, due to further limitation applied on the $(v_A)_{ac}$. Additionally, even though the BCSAC under

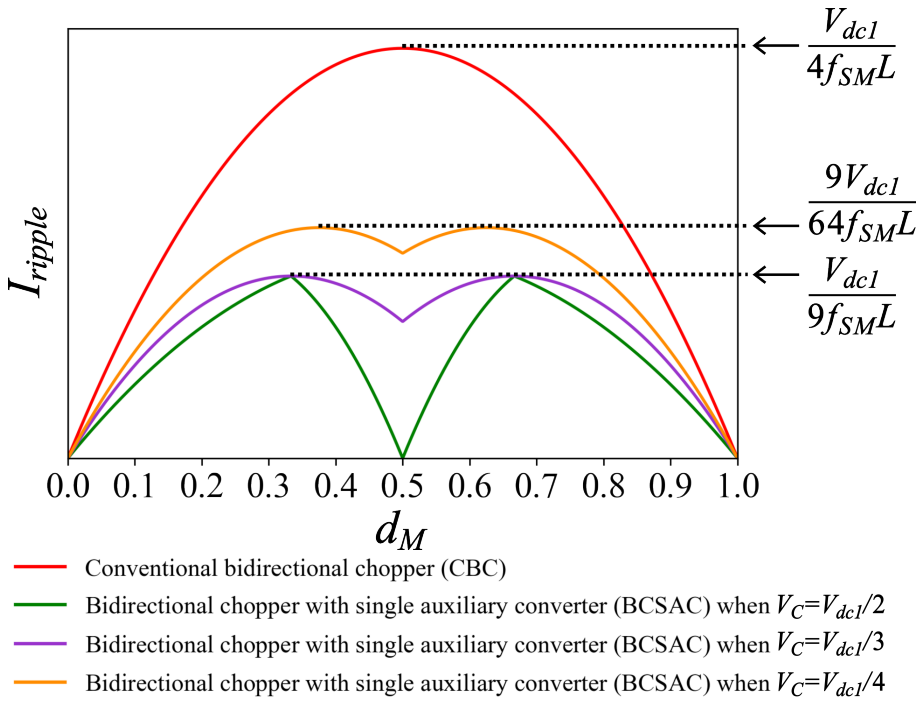

Figure A.1: Theoretical results for the switching-ripple current of the BCSAC under different settings of V_C and CBC.

$V_C = \frac{V_{dc1}}{3}$ produces the same maximum switching-ripple current as that under $V_C = \frac{V_{dc1}}{2}$, its overall performance is still worse.

A.2 Power Loss and Efficiency

The power loss breakdowns of the BCSAC under different settings and two different duty ratios (i.e., $d_M = 0.2$ and $d_M = 0.8$) are shown in Fig. A.2. From Figs A.2d, A.2c, A.2e, and A.2f, the average power losses produced by both the BCSAC under $V_C = \frac{V_{dc1}}{3}$ (11.5 kW) and $V_C = \frac{V_{dc1}}{4}$ for the maximum rating (11.65 kW) are slightly lower than that of the BCSAC (11.7 kW). The reduction comes from the lower switching losses of the auxiliary converter produced by the former two settings.

The efficiencies for all choppers are calculated based on the results of the power loss analysis and shown in Fig. A.3, where red line indicates the CBC, green line indicates the BCSAC, purple line indicates the BCSAC under $V_C = \frac{V_{dc1}}{3}$, and orange line indicates the BCSAC under $V_C = \frac{V_{dc1}}{4}$. From Fig. A.3a, both the BCSAC under $V_C = \frac{V_{dc1}}{3}$ and $V_C = \frac{V_{dc1}}{4}$ (97.1 %) have a slightly higher average efficiency than the BCSAC (97 %) under $d_M = 0.2$. However, based on Fig. A.3b, the difference between the efficiencies of the BCSAC under different settings of V_C becomes minimum.

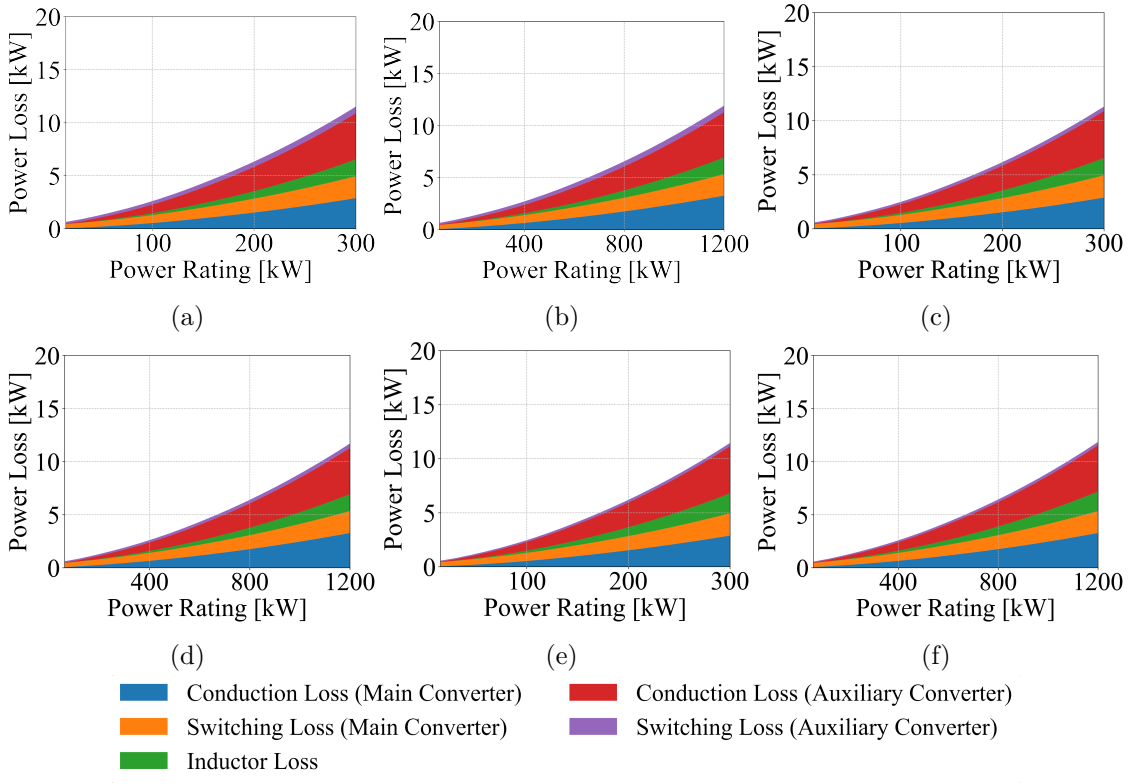

Figure A.2: Loss breakdown of (a) BCSAC under $V_C = \frac{V_{dc1}}{2}$ when $V_{dc2} = 0.3\,\text{kV}$, (b) BCSAC under $V_C = \frac{V_{dc1}}{2}$ when $V_{dc2} = 1.2\,\text{kV}$, (c) BCSAC under $V_C = \frac{V_{dc1}}{3}$ when $V_{dc2} = 0.3\,\text{kV}$, (d) BCSAC $V_C = \frac{V_{dc1}}{3}$ when $V_{dc2} = 1.2\,\text{kV}$, (e) BCSAC $V_C = \frac{V_{dc1}}{4}$ when $V_{dc2} = 0.3\,\text{kV}$, (f) BCSAC $V_C = \frac{V_{dc1}}{4}$ when $V_{dc2} = 1.2\,\text{kV}$.

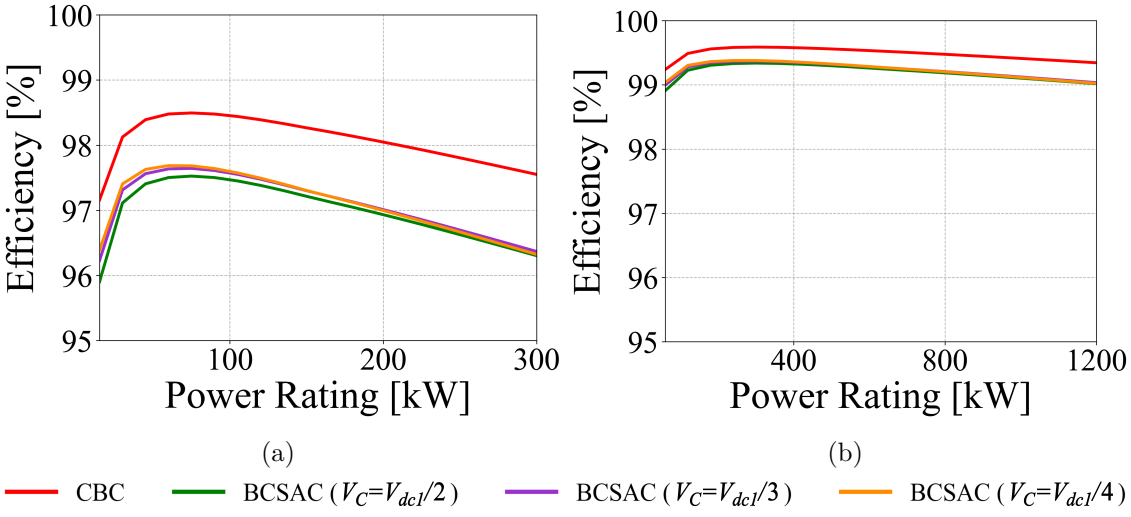

Figure A.3: Efficiency of the BCSAC under different settings of V_C and CBC when: (a) $V_{dc} = 0.3\,\text{kV}$ ($d_M = 0.2$), (b) $V_{dc} = 1.2\,\text{kV}$ ($d_M = 0.8$).

Appendix B

Volume Calculation

B.1 Design of Air-Core Inductors

In the inductor volume analysis conducted for the comparison given in Chapter 3 and Chapter 4, air-core inductors are used. The air-core inductor dimensions along with its rectangular cross-section winding dimensions are given in Fig. B.1, where the definitions of the parameters are summarized in Table B.1. The calculation processes for these parameters are similar to the ones described in [101], [104], which are simplified in the flowchart given in Fig. B.2. First, practical assumptions on the maximum current density, $J_{max} = 2 \times 10^6\,\mathrm{A/m^2}$, and the maximum current, $I_{max} = 1000\,\mathrm{A}$, are set. These assumptions should not be exceeded to avoid overheating. Then, a suitable d_i is set based on the value of d that is obtained from:

$$d = \sqrt{\frac{4I_{max}}{\pi J_{max}}}, \tag{B.1}$$

Table B.1: Definitions of the air-core inductor parameters

Parameter	**Description**
a	Distance between the axis of the winding and that of the inductor
b	Width of the winding cross-section
c	Height of the winding cross-section
d	Diameter of the wire without the insulation coating
d_i	Diameter of the wire with the insulation coating
n_t	Number of turns per layer
n_l	Number of layers
n	Number of turns

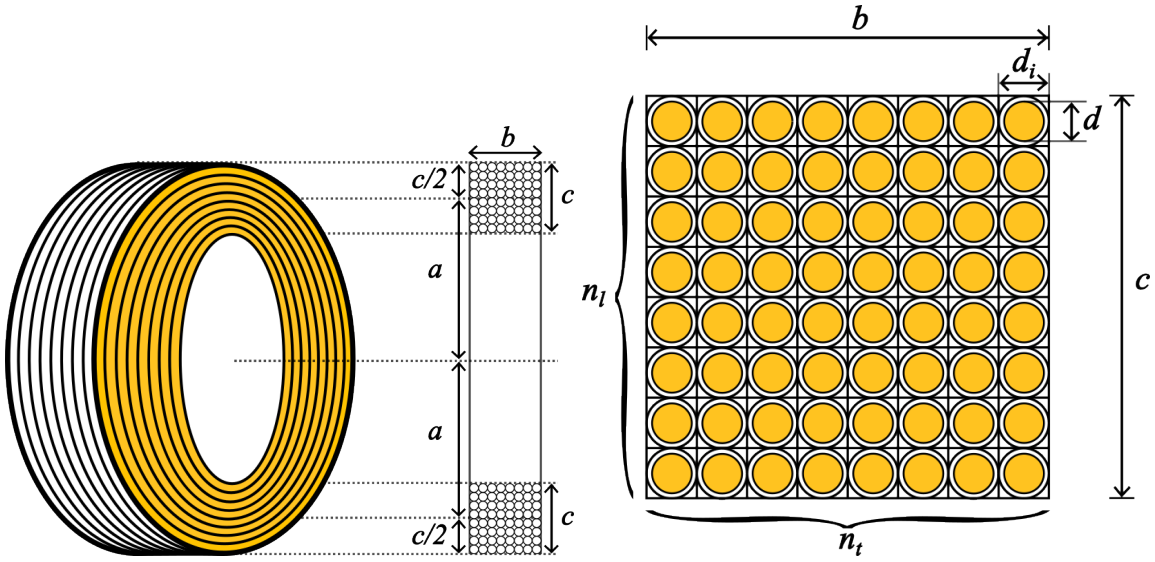

Figure B.1: Air-core inductor with rectangular cross section: (a) Inductor dimensions, (b) Winding dimensions.

where d_i should be appropriately larger than d. Further, the initial estimation of n (i.e., n_0) for a given inductance value, L, can be obtained by:

$$n_0 = \sqrt[5]{\left(\frac{L}{2.029\mu_0 d_i}\right)^2}, \tag{B.2}$$

if the Brooks geometry is assumed. Based on whether the value of $\sqrt{n_0}$ calculated from (B.2) is an integer or not, the values of n_t and n_l can be obtained to further calculate b and c:

$$b = n_t d_i \tag{B.3}$$

$$c = n_l d_i. \tag{B.4}$$

Meanwhile, a can be obtained from the minimum positive root solution of:

$$L = \frac{\mu_0 n^2 \pi a^3}{ab + 0.9a^2 + 0.32bc + 0.84ac} \tag{B.5}$$

where μ_0 is the vacuum permeability ($\mu_0 = 1.257 \times 10^{-6}\mathrm{NA}^{-2}$). Finally, based on (B.3), (B.4), and (B.5) the inductor volume, V_L, that is basically the volume of a cylinder, can be given as:

$$V_L = \pi b \left(a + \frac{c}{2}\right)^2. \tag{B.6}$$

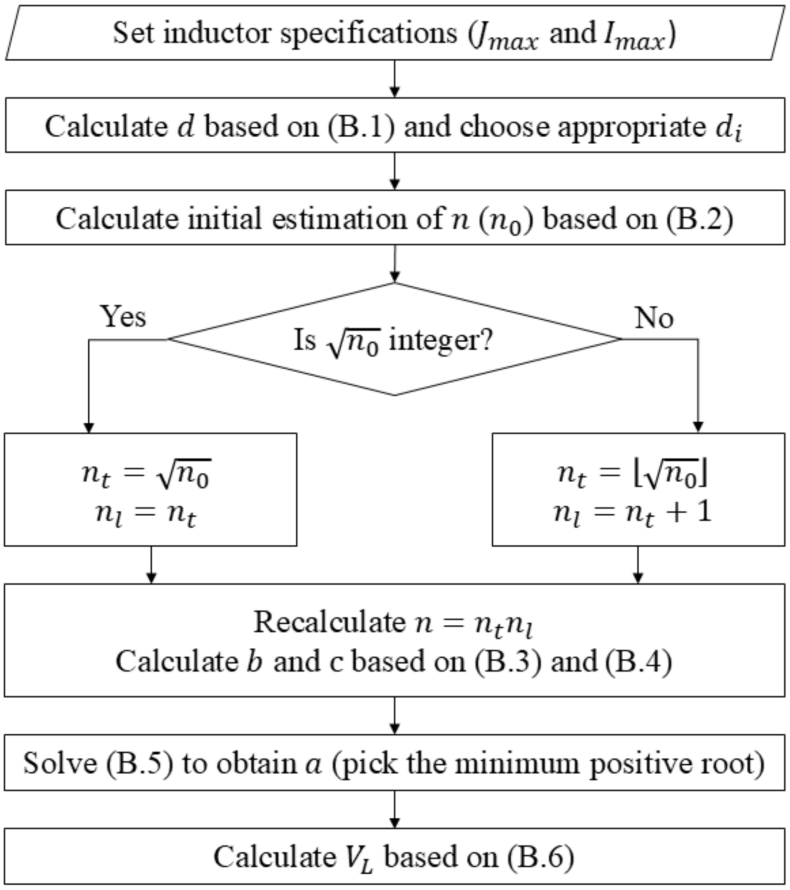

Figure B.2: Flowchart of the calculation process of the inductor volume analysis.

B.2 Cooling System Volume Calculation

In the chopper volume analysis conducted for the comparison given in Chapter 3 and Chapter 4, air-cooling system with heatsink is assumed. The cooling systems of the CBC, main converter of the BCSAC and BCSAC-PS, and TLFC and TLFC-PS are designed such that a pair of the 1MBI1000UG-330 IGBT modules is mounted on a single heatsink. Further, a single heatsink is used for the four CM1000DX-24T IGBT modules in the auxiliary converter of the BCSAC and BCSAC-PS, and a pair the same modules in the TLFC

Table B.2: Definitions of the parameters used in the cooling system volume analysis

1MBI1000UG-330		
$R_{th(j-c)Q}$	Junction-to-case thermal resistance (IGBT)	12 K/kW
$R_{th(j-c)D}$	Junction-to-case thermal resistance (FWD)	22.5 K/kW
$R_{th(c-h)}$	Case-to-heatsink thermal resistance per module	7.7 K/kW
CM1000DX-24T		
$R_{th(j-c)Q}$	Junction-to-case thermal resistance (IGBT)	28 K/kW
$R_{th(j-c)D}$	Junction-to-case thermal resistance (FWD)	49 K/kW
$R_{th(c-h)}$	Case-to-heatsink thermal resistance per module	7.1 K/kW

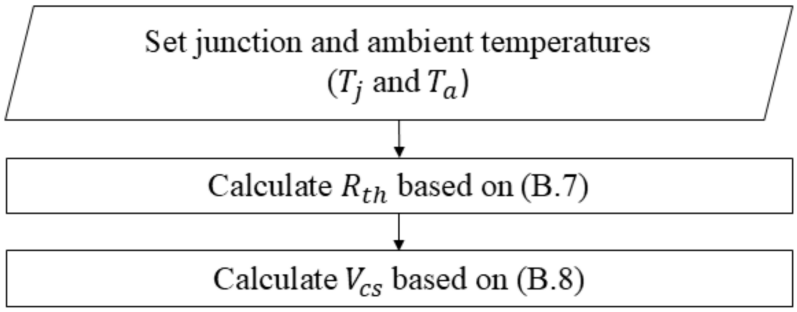

Figure B.3: Flowchart of the calculation process of the cooling system volume analysis.

and TLFC-PS. The thermal characteristics of the two IGBT modules are summarized in Table B.2. The calculation process of the cooling system (i.e., heatsink) volume is similar to the ones described in [101], [122], which are simplified in the flowchart given in Fig. B.3. First, practical assumptions on the junction temperature ($T_j = 125°C$) and ambient temperature ($T_a = 40°C$) are set, where T_j could be changed depending the type of power device used in the chopper. Then, the required thermal resistance of the heatsink, R_{th}, can be obtained from:

$$R_{th} = \frac{T_j - T_a}{P_{loss}}, \tag{B.7}$$

where P_{loss} is the total power loss produced by the power devices mounted in the heatsink (including the conduction loss of the IGBT and FWD, switching loss, and reverse recovery loss). Finally, the cooling system volume, V_{cs}, can be determined based on the set value of the cooling system performance index (CSPI) as:

$$V_{cs} = \text{CSPI}^{-1} \frac{1}{R_{th}}. \tag{B.8}$$

The CSPI value determines the indicates the cooling performance per unit volume of the system, where higher value reflects higher performances.

Appendix C

Power Loss Calculation

C.1 Power Loss Equation

The equations to the considered losses in the loss analysis can be commonly found in literature such as [127]–[131]. The IGBT conduction and switching losses can be determined by:

$$P_{IGBT-cond} = \int^{T_{IGBT-ON}} \left(v_{CE} i_L + R_{lead} {i_L}^2\right) dt \tag{C.1}$$

$$P_{IGBT-sw} = \frac{f_{SW}}{2} \int^{T_f+T_r} v_{IGBT} i_L \, dt \ . \tag{C.2}$$

Additionally, the FWD conduction and reverse recovery losses can be determined by:

$$P_{FWD-cond} = \int^{T_{FWD-ON}} \left(v_f i_L + R_{lead} {i_L}^2\right) dt \tag{C.3}$$

$$P_{FWD-rr} = \frac{f_{SW}}{2} \int^{T_{rr}} v_{FWD} i_{rr} \, dt \ , \tag{C.4}$$

where v_{CE} is the collector-emitter saturation voltage of the IGBT, v_f is the forward voltage of the FWD, v_{IGBT} is the IGBT voltage, v_{FWD} is the FWD voltage, i_{rr} is the reverse recovery current of the FWD, and R_{lead} is the internal lead resistance of the IGBT. $T_{IGBT-ON}$, T_f, and T_r are the ON period, fall time, and rise time of the IGBT, respectively, while T_{FWD-ON} and T_{rr} are the ON period and reverse recovery time of the FWD, respectively. Further, the inductor loss can be determined by:

$$P_L = R_{Ldc} I_L^2, \tag{C.5}$$

where R_{Ldc} is the inductor dc-resistance. Based on [101], [104], it is given by:

$$R_{Ldc} = \frac{2\pi n^2 a}{k_p \sigma b c}, \tag{C.6}$$

where k_p is the fraction of the volume occupied by the conductors to the total volume of the coil of the inductor. It can be estimated from the winding area packing factor, or the cross-sectional area of the conductor divided by the cross-sectional area of the inductor (i.e., $k_p = \frac{\pi}{4}\left(\frac{d}{d_i}\right)^2$). Meanwhile, σ is the electrical conductivity of the conductor material, which in this dissertation is assumed to be iron (i.e., $\sigma = 1.77\,\Omega^{-1}\mathrm{m}^{-1}$).

C.2 Characteristics of the IGBT Modules

The IGBT power modules 1MBI1000UG-330 (Si-IGBT, 1-in-1, 3.3 kV) from Fuji Electric and CM1000DX-24T (Si-IGBT, 1-in-1, 1.2 kV) from Mitsubishi Electric are used in the designs of the CBC, TLFC, TLFC-PS, BCAC, BCSAC, and BCSAC-PS made in the comparisons conducted in Chapter 3 and Chapter 4. Linear approximations of the module specifications based on their respective datasheets are used to estimate the power losses. Further, the specifications used in the approximations are the ones listed under the junction temperature of $T_j = 150°$ and the gate-emitter voltage of $V_{GE} = 15\,\mathrm{V}$.

The approximations of the characteristics shown in Fig. C.1 are used to calculate the conduction losses of the IGBTs, where Fig. C.1a shows the collector current versus the collector-emitter voltage of the 1MBI1000UG-330 module, while Fig. C.1b shows that of the CM1000DX-24T module. Similarly, the characteristics shown in Fig. C.2 are used to calculate the conduction losses of the FWDs, where Fig. C.2a shows the forward current versus the forward voltage of the 1MBI1000UG-330 module, while Fig. C.2b shows that of the CM1000DX-24T module.

The approximations of the characteristics shown in Fig. C.3 are used to calculate the switching losses of the IGBTs, where Fig. C.3a shows the rise and fall time versus the collector curent of the 1MBI1000UG-330 module, while Fig. C.3b shows that of the CM1000DX-24T module. Similarly, the characteristics shown in Fig. C.4 are used to calculate the reverse recovery losses of the FWDs, where Fig. C.4a shows the reverse recovery current and time versus the forward current of the 1MBI1000UG-330 module, while Fig. C.4b shows that of the CM1000DX-24T module.

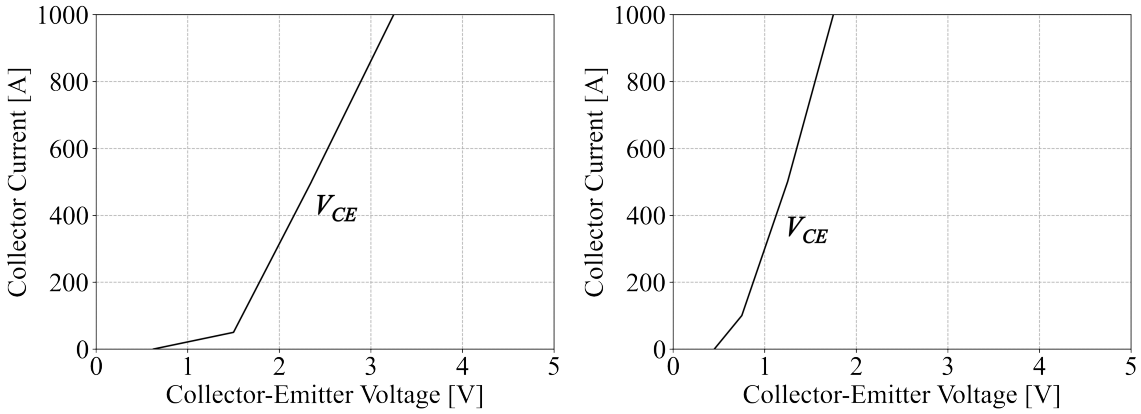

(a) (b)

Figure C.1: Approximation results of the collector current versus the collector-emitter voltage: (a) For the 1MBI1000UG-330 module, (b) For the CM1000DX-24T module.

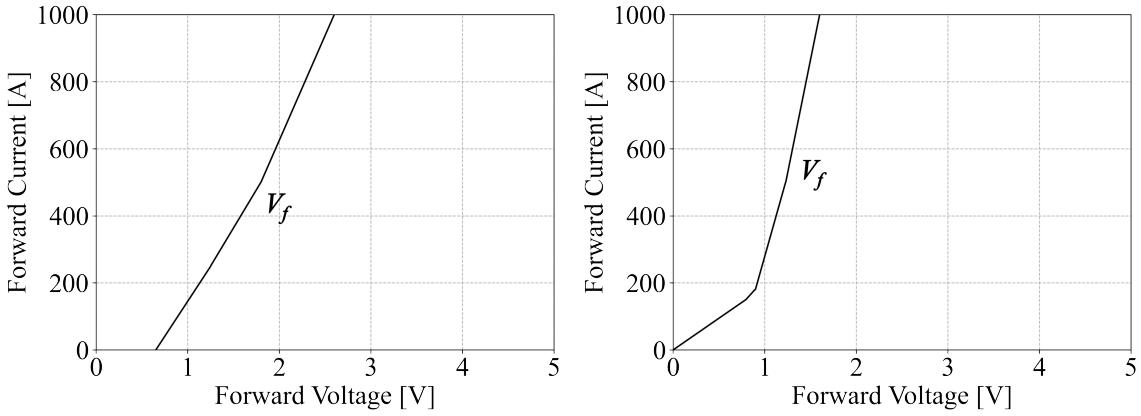

(a) (b)

Figure C.2: Approximation results of the forward current versus the forward voltage: (a) For the 1MBI1000UG-330 module, (b) For the CM1000DX-24T module.

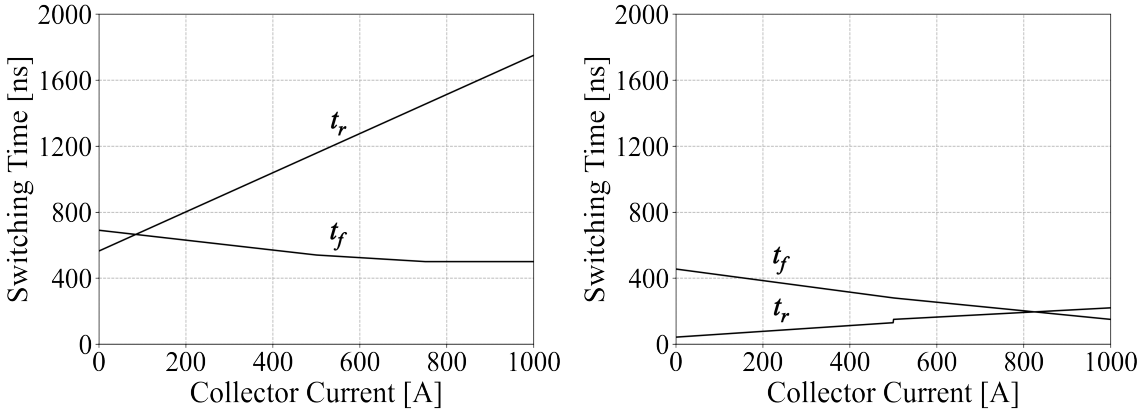

(a) (b)

Figure C.3: Approximation results of the rise and fall time versus the collector curent: (a) For the 1MBI1000UG-330 module, (b) For the CM1000DX-24T module.

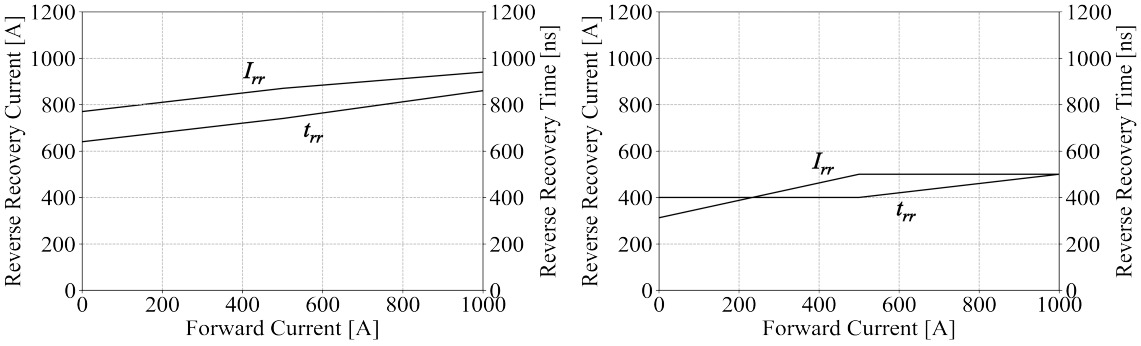

Figure C.4: Approximation results of the reverse recovery current and time versus the forward current: (a) For the 1MBI1000UG-330 module, (b) For the CM1000DX-24T module.

List of Publications

Journal Publications

1. G. A. M. Nasution, M. Matsumoto, and M. Hagiwara, "Bidirectional chopper with single-cell auxiliary full-bridge converter for onboard battery energy storage system," in IEEE Transactions on Power Electronics, vol. 39, no. 8, pp. 10021-10033, 2024. DOI: 10.1109/TPEL.2024.3392923.

2. G. A. M. Nasution and M. Hagiwara, "AC Component-Based Control and Phase Shift Applications on Bidirectional Chopper with Auxiliary Full-Bridge Converter," in IEEE Transactions on Power Electronics, vol. 40, no. 4, pp. 5440-5455, 2024. DOI: 10.1109/TPEL2024.3522332.

Conference Publications

1. G. A. M. Nasution, M. Matsumoto, and M. Hagiwara, "Switching-ripple current evaluation of bidirectional chopper with single auxiliary full-bridge converter," in 2023 IEEE Energy Conversion Congress and Exposition (ECCE), 2023, pp. 6357-6364. DOI: 10.1109/ECCE53617.2023.10362001.

2. G. A. M. Nasution and M. Hagiwara, "Evaluation of Phase Shift Application in Bidirectional Chopper with Single-Cell Auxiliary Full-Bridge Converter," in 2024 13th International Conference on Renewable Energy Research and Applications (ICRERA), 2024, pp. 400-407. DOI: 10.1109/ICRERA62673.2024.10815543.

Bibliography

[1] O. Chen, V. G. Tapia, and A. Rogé, "Co2 emissions in 2022," International Energy Agency (IEA), France, Tech. Rep., 2023. [Online]. Available: https://www.iea.org/reports/co2-emissions-in-2022.

[2] I. E. A. (IEA), *Global co2 emissions from transport by sub-sector in the net zero scenario, 2000-2030*, Accessed: 2024-9-2, 2023. [Online]. Available: https://www.iea.org/data-and-statistics/charts/global-co2-emissions-from-transport-by-sub-sector-in-the-net-zero-scenario-2000-2030-2.

[3] B. Zou, "Electrification of transport: Advantages and prospects," *Highlights in Science, Engineering and Technology*, vol. 43, pp. 175–184, Apr. 2023. DOI: 10.54097/hset.v43i.7418. [Online]. Available: https://drpress.org/ojs/index.php/HSET/article/view/7418.

[4] S. J. Dale, R. E. Hebner, and G. Sulligoi, "Electric ship technologies," *Proceedings of the IEEE*, vol. 103, no. 12, pp. 2225–2228, 2015. DOI: 10.1109/JPROC.2015.2497018.

[5] G. Rohith, K. B. Devika, P. P. Menon, and S. C. Subramanian, "Sustainable heavy goods vehicle electrification strategies for long-haul road freight transportation," *IEEE Access*, vol. 11, pp. 26 459–26 470, 2023. DOI: 10.1109/ACCESS.2023.3257431.

[6] G. Buticchi, P. Wheeler, and D. Boroyevich, "The more-electric aircraft and beyond," *Proceedings of the IEEE*, vol. 111, no. 4, pp. 356–370, 2023. DOI: 10.1109/JPROC.2022.3152995.

[7] A. Poullikkas, "Sustainable options for electric vehicle technologies," *Renewable and Sustainable Energy Reviews*, vol. 41, pp. 1277–1287, 2015, ISSN: 1364-0321.

DOI: https://doi.org/10.1016/j.rser.2014.09.016. [Online]. Available: https://www.sciencedirect.com/science/article/pii/S1364032114007898.

[8] G. Sulligoi, A. Vicenzutti, and R. Menis, "All-electric ship design: From electrical propulsion to integrated electrical and electronic power systems," *IEEE Transactions on Transportation Electrification*, vol. 2, no. 4, pp. 507–521, 2016. DOI: 10.1109/TTE.2016.2598078.

[9] B. Sarlioglu and C. T. Morris, "More electric aircraft: Review, challenges, and opportunities for commercial transport aircraft," *IEEE Transactions on Transportation Electrification*, vol. 1, no. 1, pp. 54–64, 2015. DOI: 10.1109/TTE.2015.2426499.

[10] M. Brenna, V. Bucci, M. C. Falvo, *et al.*, "A review on energy efficiency in three transportation sectors: Railways, electrical vehicles and marine," *Energies*, vol. 13, no. 9, 2020, ISSN: 1996-1073. DOI: 10.3390/en13092378. [Online]. Available: https://www.mdpi.com/1996-1073/13/9/2378.

[11] I. T. Vadium, R. Das, Y. Wang, G. Putrus, and R. Kotter, "Electric vehicle carbon footprint reduction via intelligent charging strategies," in *2019 8th International Conference on Modern Power Systems (MPS)*, 2019, pp. 1–6. DOI: 10.1109/MPS.2019.8759783.

[12] Z. Hu, R. T. Mehrjardi, and M. Ehsani, "On the lifetime emissions of conventional, hybrid, plug-in hybrid and electric vehicles," *IEEE Transactions on Industry Applications*, vol. 60, no. 2, pp. 3502–3511, 2024. DOI: 10.1109/TIA.2023.3330950.

[13] S. Jenu, S. Baumeister, J. Pippuri-Mäkeläinen, A. Manninen, and M. Paakkinen, "The emission reduction potential of electric transport modes in finland," *Environmental Research Letters*, vol. 16, no. 10, p. 104 010, Sep. 2021. DOI: 10.1088/1748-9326/ac2440. [Online]. Available: https://dx.doi.org/10.1088/1748-9326/ac2440.

[14] C. Schuss, T. Fabritius, B. Eichberger, and T. Rahkonen, "Impacts on the output power of photovoltaics on top of electric and hybrid electric vehicles," *IEEE Transactions on Instrumentation and Measurement*, vol. 69, no. 5, pp. 2449–2458, 2020. DOI: 10.1109/TIM.2019.2962850.

[15] B. G. Sherkhane and S. L. Chavan, "Analysis of electric vehicle charging management and renewable power generation based on transactive control," in *2023 IEEE 3rd International Conference on Smart Technologies for Power, Energy and Control (STPEC)*, 2023, pp. 1–4. DOI: 10.1109/STPEC59253.2023.10430558.

[16] H. Shukla, M. Raju, N. Patidar, and S. Nandanwar, "Optimal load frequency management of an interconnected power system considering geothermal power plant and electric vehicle," in *2023 3rd International Conference on Energy, Power and Electrical Engineering (EPEE)*, 2023, pp. 1296–1300. DOI: 10.1109/EPEE59859.2023.10351984.

[17] G. Kim and J. Hur, "Methodology for security analysis of grid- connected electric vehicle charging station with wind generating resources," *IEEE Access*, vol. 9, pp. 63 905–63 914, 2021. DOI: 10.1109/ACCESS.2021.3075072.

[18] B. Bilgin and A. Emadi, "Electric motors in electrified transportation: A step toward achieving a sustainable and highly efficient transportation system," *IEEE Power Electronics Magazine*, vol. 1, no. 2, pp. 10–17, 2014. DOI: 10.1109/MPEL.2014.2312275.

[19] J. P. D. S. Rodrigues, W. T. Nunes, M. Brunoro, and R. B. Nunes, "Comparison of well-to-wheel energy efficiency between combustion vehicles and electric vehicles," in *2022 International Conference on Electrical, Computer and Energy Technologies (ICECET)*, 2022, pp. 1–4. DOI: 10.1109/ICECET55527.2022.9872658.

[20] A. Albatayneh, M. N. Assaf, D. Alterman, and M. Jaradat, "Comparison of the overall energy efficiency for internal combustion engine vehicles and electric vehicles," *Environmental and Climate Technologies*, vol. 24, no. 1, pp. 669–680, 2020. DOI: doi:10.2478/rtuect-2020-0041. [Online]. Available: https://doi.org/10.2478/rtuect-2020-0041.

[21] V. Totev, "A model based comparison on the efficiency of electric vehicles to conventional vehicles," in *2023 18th Conference on Electrical Machines, Drives and Power Systems (ELMA)*, 2023, pp. 1–5. DOI: 10.1109/ELMA58392.2023.10202491.

[22] T.-T. Duong, P.-S. Huynh, and Q.-T. Ngo, "Research to evaluate the regenerative braking system effect on fuel consumption of hybrid vehicle," in *2021 International*

Conference on System Science and Engineering (ICSSE), 2021, pp. 252–256. DOI: 10.1109/ICSSE52999.2021.9538417.

[23] M. Gunjal, L. Mathew, and S. Reji, "Comparative study of electric vehicles: Regenerative braking system versus non-regenerative braking systems," in *2024 4th International Conference on Innovative Practices in Technology and Management (ICIPTM)*, 2024, pp. 1–6. DOI: 10.1109/ICIPTM59628.2024.10563728.

[24] H. Jain, S. Maitreya, and P. Paliwal, "Cooperative control of regenerative and anti-lock braking systems in electric vehicles using fuzzy logic," in *2021 4th International Conference on Recent Developments in Control, Automation & Power Engineering (RDCAPE)*, 2021, pp. 62–66. DOI: 10.1109/RDCAPE52977.2021.9633401.

[25] M. M. Rehman and W. G. Morsi, "Comparative economic analysis of conventional and plug-in battery electric vehicles in canada," in *2022 IEEE Electrical Power and Energy Conference (EPEC)*, 2022, pp. 218–223. DOI: 10.1109/EPEC56903.2022.10000170.

[26] H. Alnuman, D. Gladwin, and M. Foster, "Electrical modelling of a dc railway system with multiple trains," *Energies*, vol. 11, no. 11, 2018, ISSN: 1996-1073. [Online]. Available: https://www.mdpi.com/1996-1073/11/11/3211.

[27] M. Popescu and A. Bitoleanu, "A review of the energy efficiency improvement in dc railway systems," *Energies*, vol. 12, no. 6, 2019, ISSN: 1996-1073. DOI: 10.3390/en12061092. [Online]. Available: https://www.mdpi.com/1996-1073/12/6/1092.

[28] J. Pouget, B. Guo, L. Bossoney, J. Coppex, D. Roggo, and C. Ellert, "Energetic simulation of dc railway micro-grid interconnecting with pv solar panels, ev charger infrastructures and electrical railway network," in *2020 IEEE Vehicle Power and Propulsion Conference (VPPC)*, 2020, pp. 1–7. DOI: 10.1109/VPPC49601.2020.9330829.

[29] K. Tesaki and M. Hagiwara, "Efficiency and power density evaluations of bidirectional non-isolated dc-dc converter based on flying-capacitor converters," in *2021 23rd European Conference on Power Electronics and Applications (EPE'21 ECCE Europe)*, 2021, pp. 1–10. DOI: 10.23919/EPE21ECCEEurope50061.2021.9570460.

[30] U. Brachunova, V. Kozlovsky, and A. Saksonov, "Study of the influence of the rated voltage of the on-board network of a modern car," in *2022 International Ural Conference on Electrical Power Engineering (UralCon)*, 2022, pp. 175–179. DOI: 10.1109/UralCon54942.2022.9906752.

[31] S. Wolff, S. Kalt, M. Bstieler, and M. Lienkamp, "Influence of powertrain topology and electric machine design on efficiency of battery electric trucks—a simulative case-study," *Energies*, vol. 14, no. 2, 2021, ISSN: 1996-1073. DOI: 10.3390/en14020328. [Online]. Available: https://www.mdpi.com/1996-1073/14/2/328.

[32] A. Barzkar and M. Ghassemi, "Components of electrical power systems in more and all-electric aircraft: A review," *IEEE Transactions on Transportation Electrification*, vol. 8, no. 4, pp. 4037–4053, 2022. DOI: 10.1109/TTE.2022.3174362.

[33] S. Castellan, R. Menis, A. Tessarolo, F. Luise, and T. Mazzuca, "A review of power electronics equipment for all-electric ship mvdc power systems," *International Journal of Electrical Power & Energy Systems*, vol. 96, pp. 306–323, 2018, ISSN: 0142-0615. DOI: https://doi.org/10.1016/j.ijepes.2017.09.040. [Online]. Available: https://www.sciencedirect.com/science/article/pii/S0142061517300595.

[34] C. Wu, S. Lu, F. Xue, L. Jiang, and M. Chen, "Optimal sizing of onboard energy storage devices for electrified railway systems," *IEEE Transactions on Transportation Electrification*, vol. 6, no. 3, pp. 1301–1311, 2020. DOI: 10.1109/TTE.2020.2996362.

[35] J. Kamalakannan, K. R. Reddy, N. Kumar, S. S.M., K. Dewangan, and V. Kannan, "Design of hybrid energy storage and management system in hybrid electric vehicle using machine learning approach," in *2023 4th International Conference on Smart Electronics and Communication (ICOSEC)*, 2023, pp. 1313–1317. DOI: 10.1109/ICOSEC58147.2023.10276076.

[36] M. U. Mutarraf, Y. Terriche, K. A. K. Niazi, J. C. Vasquez, and J. M. Guerrero, "Energy storage systems for shipboard microgrids—a review," *Energies*, vol. 11, no. 12, 2018, ISSN: 1996-1073. DOI: 10.3390/en11123492. [Online]. Available: https://www.mdpi.com/1996-1073/11/12/3492.

[37] S. Mousavi G, F. Faraji, A. Majazi, and K. Al-Haddad, "A comprehensive review of flywheel energy storage system technology," *Renewable and Sustainable Energy Reviews*, vol. 67, pp. 477–490, 2017, ISSN: 1364-0321. DOI: https://doi.org/10.1016/j.rser.2016.09.060. [Online]. Available: https://www.sciencedirect.com/science/article/pii/S1364032116305597.

[38] W. Zhang and Z. Wang, "Dual-mode coordinated control of magnetic suspension flywheel battery based on vehicle driving conditions characteristics," *IEEE Transactions on Transportation Electrification*, vol. 10, no. 1, pp. 2124–2134, 2024. DOI: 10.1109/TTE.2023.3288730.

[39] A. G. Olabi, T. Wilberforce, M. A. Abdelkareem, and M. Ramadan, "Critical review of flywheel energy storage system," *Energies*, vol. 14, no. 8, 2021, ISSN: 1996-1073. DOI: 10.3390/en14082159. [Online]. Available: https://www.mdpi.com/1996-1073/14/8/2159.

[40] H. Fang, X. Zhang, and Y. Wei, "Supercapacitor energy storage system based coordinative low-voltage-ride-through control for wind energy conversion system," in *2021 24th International Conference on Electrical Machines and Systems (ICEMS)*, 2021, pp. 276–280. DOI: 10.23919/ICEMS52562.2021.9634199.

[41] F. Zhu, Z. Yang, H. Xia, and F. Lin, "Hierarchical control and full-range dynamic performance optimization of the supercapacitor energy storage system in urban railway," *IEEE Transactions on Industrial Electronics*, vol. 65, no. 8, pp. 6646–6656, 2018. DOI: 10.1109/TIE.2017.2772174.

[42] H. Yang, "A review of supercapacitor-based energy storage systems for microgrid applications," in *2018 IEEE Power & Energy Society General Meeting (PESGM)*, 2018, pp. 1–5. DOI: 10.1109/PESGM.2018.8585956.

[43] Y. Sun, Z. Li, M. Shahidehpour, and B. Ai, "Battery-based energy storage transportation for enhancing power system economics and security," *IEEE Transactions on Smart Grid*, vol. 6, no. 5, pp. 2395–2402, 2015. DOI: 10.1109/TSG.2015.2390211.

[44] S. Li, P. Zhao, C. Gu, J. Li, D. Huo, and S. Cheng, "Aging mitigation for battery energy storage system in electric vehicles," *IEEE Transactions on Smart Grid*, vol. 14, no. 3, pp. 2152–2163, 2023. DOI: 10.1109/TSG.2022.3210041.

[45] T. Iwase, J. Kawamura, K. Tokai, and M. Kageyama, "Development of battery system for railway vehicle," in *2015 International Conference on Electrical Systems for Aircraft, Railway, Ship Propulsion and Road Vehicles (ESARS)*, 2015, pp. 1–6. DOI: 10.1109/ESARS.2015.7101431.

[46] H. Hayashiya, S. Abe, Y. Iino, *et al.*, "Proposal of a novel control method of li-ion battery system for regenerative energy utilization in traction power supply system," in *2016 IEEE International Power Electronics and Motion Control Conference (PEMC)*, 2016, pp. 298–303. DOI: 10.1109/EPEPEMC.2016.7752014.

[47] *Battery Electric Rail Technology Review - A Technical and Operational Assessment. Current Status, Challenges and Perspectives*, vol. 2022 Joint Rail Conference, ASME/IEEE Joint Rail Conference, Apr. 2022, V001T05A002. DOI: 10.1115/JRC2022-78133. eprint: https://asmedigitalcollection.asme.org/JRC/proceedings-pdf/JRC2022/85758/V001T05A002/6892659/v001t05a002-jrc2022-78133.pdf. [Online]. Available: https://doi.org/10.1115/JRC2022-78133.

[48] K. Ogura, K. Nishimura, T. Matsumura, *et al.*, "Test results of a high capacity wayside energy storage system using ni-mh batteries for dc electric railway at new york city transit," in *2011 IEEE Green Technologies Conference (IEEE-Green)*, 2011, pp. 1–6. DOI: 10.1109/GREEN.2011.5754859.

[49] J. A. Aguado, A. J. Sánchez Racero, and S. de la Torre, "Optimal operation of electric railways with renewable energy and electric storage systems," *IEEE Transactions on Smart Grid*, vol. 9, no. 2, pp. 993–1001, 2018. DOI: 10.1109/TSG.2016.2574200.

[50] Z. Zhang, S. Yang, R. Yang, *et al.*, "Design and simulation of on-board hybrid energy storage systems in railway vehicle," in *2023 8th Asia Conference on Power and Electrical Engineering (ACPEE)*, 2023, pp. 729–733. DOI: 10.1109/ACPEE56931.2023.10135666.

[51] R. Liu, L. Xu, F. Liu, Z. Zheng, K. Wang, and Y. Li, "A novel architecture of urban rail transit based on hybrid energy storage systems using droop control," in *2018 IEEE International Conference on Electrical Systems for Aircraft, Railway, Ship Propulsion and Road Vehicles & International Transportation Electrification*

Conference (ESARS-ITEC), 2018, pp. 1–6. DOI: 10.1109/ESARS-ITEC.2018.8607728.

[52] X. Chen, W. Shen, T. T. Vo, Z. Cao, and A. Kapoor, "An overview of lithium-ion batteries for electric vehicles," in *2012 10th International Power & Energy Conference (IPEC)*, 2012, pp. 230–235. DOI: 10.1109/ASSCC.2012.6523269.

[53] Z. Liu, J. Song, J. Kubal, *et al.*, "Comparing total cost of ownership of battery electric vehicles and internal combustion engine vehicles," *Energy Policy*, vol. 158, p. 112 564, 2021, ISSN: 0301-4215. DOI: https://doi.org/10.1016/j.enpol.2021.112564. [Online]. Available: https://www.sciencedirect.com/science/article/pii/S0301421521004341.

[54] C. Iclodean, B. Varga, N. Burnete, D. Cimerdean, and B. Jurchiş, "Comparison of different battery types for electric vehicles," *IOP Conference Series: Materials Science and Engineering*, vol. 252, no. 1, p. 012 058, Oct. 2017. DOI: 10.1088/1757-899X/252/1/012058. [Online]. Available: https://dx.doi.org/10.1088/1757-899X/252/1/012058.

[55] K. Beom-Jun, N. Seok-Jin, and I.-H. Cho, "Research on improving the reliability and reducing the weight of battery packs for railway vehicles," *Journal of Power Electronics*, vol. 24, no. 5, pp. 810–821, 2024. DOI: 10.1007/s43236-024-00817-1.

[56] O. Hegazy, J. V. Mierlo, and P. Lataire, "Analysis, modeling, and implementation of a multidevice interleaved dc/dc converter for fuel cell hybrid electric vehicles," *IEEE Transactions on Power Electronics*, vol. 27, no. 11, pp. 4445–4458, 2012. DOI: 10.1109/TPEL.2012.2183148.

[57] D. Han, J. Noppakunkajorn, and B. Sarlioglu, "Comprehensive efficiency, weight, and volume comparison of sic- and si-based bidirectional dc-dc converters for hybrid electric vehicles," *IEEE Transactions on Vehicular Technology*, vol. 63, no. 7, pp. 3001–3010, 2014. DOI: 10.1109/TVT.2014.2323193.

[58] Y. Pascal and G. Pillonnet, "Efficiency comparison of inductor-, capacitor-, and resonant-based converters fully integrated in cmos technology," *IEEE Journal on Emerging and Selected Topics in Circuits and Systems*, vol. 5, no. 3, pp. 421–429, 2015. DOI: 10.1109/JETCAS.2015.2462016.

[59] D. McLean, "Dielectric materials and capacitor miniaturization," *IEEE Transactions on Parts, Materials and Packaging*, vol. 3, no. 4, pp. 163–169, 1967. DOI: 10.1109/TPMP.1967.1135735.

[60] D. J. Perreault, J. Hu, J. M. Rivas, *et al.*, "Opportunities and challenges in very high frequency power conversion," in *2009 Twenty-Fourth Annual IEEE Applied Power Electronics Conference and Exposition*, 2009, pp. 1–14. DOI: 10.1109/APEC.2009.4802625.

[61] C. Collins and M. Duffy, "Limits and opportunities for distributed inductors in high-current, high-frequency applications," *IEEE Transactions on Power Electronics*, vol. 25, no. 11, pp. 2710–2721, 2010. DOI: 10.1109/TPEL.2010.2047117.

[62] M. Duffy, C. Collins, F. F. Rhen, P. McCloskey, and S. Roy, "High current inductor design for mhz switching," in *2008 IEEE Power Electronics Specialists Conference*, 2008, pp. 2672–2677. DOI: 10.1109/PESC.2008.4592346.

[63] K. Yasui, S. Hayakawa, T. Ishigaki, *et al.*, "A 3.3 kv 1000 a high power density sic power module with sintered copper die attach technology," in *PCIM Europe 2019; International Exhibition and Conference for Power Electronics, Intelligent Motion, Renewable Energy and Energy Management*, 2019, pp. 1–6.

[64] N. Soltau, E. Wiesner, E. Stumpf, S. Idaka, and K. Hatori, "Electric-energy savings using 3.3 kv full-sic power-modules in traction applications," in *2020 Fifteenth International Conference on Ecological Vehicles and Renewable Energies (EVER)*, 2020, pp. 1–5. DOI: 10.1109/EVER48776.2020.9242996.

[65] Y. Yamamoto, T. Takiguchi, T. Sato, and H. Koizumi, "Two-phase interleaved bidirectional converter input-parallel output-series connection," in *2015 9th International Conference on Power Electronics and ECCE Asia (ICPE-ECCE Asia)*, 2015, pp. 301–308. DOI: 10.1109/ICPE.2015.7167801.

[66] B. Le-Huy Nguyen, H. Cha, T. Vu, and T.-T. Nguyen, "Integrated multiport bidirectional dc-dc converter for hev/fcv applications," in *IECON 2021 - 47th Annual Conference of the IEEE Industrial Electronics Society*, 2021, pp. 1–6. DOI: 10.1109/IECON48115.2021.9589188.

[67] J. Radeen, A. Ajith, A. C, A. R.B, and M. A. A, "Design and simulation of bidirectional dc-dc converter in solar pv system for battery charging application," in *2023 IEEE International Conference on Power Electronics, Smart Grid, and Renewable Energy (PESGRE)*, 2023, pp. 1–6. DOI: 10.1109/PESGRE58662.2023.10405100.

[68] Q. Tian, G. Zeng, W. Xu, Z. Huang, and D. Ma, "Design of a bi-directional dc-dc converter for high-efficiency emergency self-traction of high-speed railway trains," in *2022 4th International Conference on Smart Power & Internet Energy Systems (SPIES)*, 2022, pp. 281–286. DOI: 10.1109/SPIES55999.2022.10082705.

[69] D. Atkar, P. Chatuvedi, H. M. Suryawanshi, *et al.*, "Bidirectional soft switched lclc based solid state transformer for smart grid infrastructure," in *2020 IEEE First International Conference on Smart Technologies for Power, Energy and Control (STPEC)*, 2020, pp. 1–6. DOI: 10.1109/STPEC49749.2020.9297673.

[70] A. Diab-Marzouk and O. Trescases, "Sic-based bidirectional ćuk converter with differential power processing and mppt for a solar powered aircraft," *IEEE Transactions on Transportation Electrification*, vol. 1, no. 4, pp. 369–381, 2015. DOI: 10.1109/TTE.2015.2505302.

[71] G. Lithesh, B. Krishna, and V. Karthikeyan, "Review and comparative study of bi-directional dc-dc converters," in *2021 IEEE International Power and Renewable Energy Conference (IPRECON)*, 2021, pp. 1–6. DOI: 10.1109/IPRECON52453.2021.9640712.

[72] R. K. Kanaparthi, J. P. Singh, and M. S. Ballal, "A review on multi-port bidirectional isolated and non-isolated dc-dc converters for renewable applications," in *2022 IEEE International Conference on Power Electronics, Drives and Energy Systems (PEDES)*, 2022, pp. 1–6. DOI: 10.1109/PEDES56012.2022.10080049.

[73] E. Stolyarov, M. Lashkevich, E. Kulik, Y. Ali, G. Demidova, and A. Anuchin, "A control strategy for bidirectional buck converter with combining continuous and active discontinuous conducting modes," in *2024 IEEE 25th International Conference of Young Professionals in Electron Devices and Materials (EDM)*, 2024, pp. 1090–1095. DOI: 10.1109/EDM61683.2024.10615126.

[74] D. Lei, W. Xueping, L. Zhen, and L. Xiaozhong, "A new soft switching bidirectional buck or boost dc-dc converter," in *2008 International Conference on Electrical Machines and Systems*, 2008, pp. 1163–1167.

[75] R. Naderi, A. K. Sadigh, and K. M. Smedley, "Dual flying capacitor active-neutral-point-clamped multilevel converter," *IEEE Transactions on Power Electronics*, vol. 31, no. 9, pp. 6476–6484, 2016. DOI: 10.1109/TPEL.2015.2501401.

[76] R. Teichmann and S. Bernet, "A comparison of three-level converters versus two-level converters for low-voltage drives, traction, and utility applications," *IEEE Transactions on Industry Applications*, vol. 41, no. 3, pp. 855–865, 2005. DOI: 10.1109/TIA.2005.847285.

[77] B. K. Bose, "Multi-level converters," *Electronics*, vol. 4, no. 3, pp. 582–585, 2015, ISSN: 2079-9292. DOI: 10.3390/electronics4030582. [Online]. Available: https://www.mdpi.com/2079-9292/4/3/582.

[78] R. Girish Ganesan and M. Prabhakar, "Multi-level dc-dc converter for high gain applications," *International Journal of Power Electronics and Drive Systems*, vol. 3, no. 4, pp. 365–373, 2013.

[79] Y. Liu, H. Pengfei, G. Jie, and J. Daozhuo, "A review of module multi-level converters," in *2011 Seventh International Conference on Natural Computation*, vol. 4, 2011, pp. 1934–1940. DOI: 10.1109/ICNC.2011.6022414.

[80] S. K. Sahu, S. Prasoon, S. Gaurav, and C. Kumar, "Operation and control of modular multilevel dc-dc converter for ev charging application," in *2023 11th National Power Electronics Conference (NPEC)*, 2023, pp. 1–6. DOI: 10.1109/NPEC57805.2023.10384926.

[81] S. Sarkar and A. Das, "A dc-dc modular multilevel converter topology with single arm for mvdc railway application," in *2023 IEEE 32nd International Symposium on Industrial Electronics (ISIE)*, 2023, pp. 1–6. DOI: 10.1109/ISIE51358.2023.10227946.

[82] R. Hariri, F. Sebaaly, and H. Y. Kanaan, "A review on modular multilevel converters in electric vehicles," in *IECON 2020 The 46th Annual Conference of the IEEE Industrial Electronics Society*, 2020, pp. 4987–1993. DOI: 10.1109/IECON43393.2020.9255037.

[83] L. J. Kere, M. L. Doumbia, S. Kelouwani, and K. Agbossou, "Cascaded h-bridge multilevel converter for electric vehicle speed control," in *2015 IEEE Vehicle Power and Propulsion Conference (VPPC)*, 2015, pp. 1–6. DOI: 10.1109/VPPC.2015.7352907.

[84] D. Ronanki and S. S. Williamson, "Modular multilevel converters for transportation electrification: Challenges and opportunities," *IEEE Transactions on Transportation Electrification*, vol. 4, no. 2, pp. 399–407, 2018. DOI: 10.1109/TTE.2018.2792330.

[85] J.-i. Itoh, R. Ishibashi, H. N. Le, N. Takaoka, K. Kusaka, and K. Tanabe, "Control method of flying capacitor converter operated in discontinuous current mode and critical current mode," in *2018 IEEE Energy Conversion Congress and Exposition (ECCE)*, 2018, pp. 155–161. DOI: 10.1109/ECCE.2018.8557726.

[86] T. Shioi, M. Miyashita, S. Nagai, *et al.*, "Battery management system with flying capacitor converter operated in discontinuous current mode," in *2019 20th International Symposium on Power Electronics (Ee)*, 2019, pp. 1–6. DOI: 10.1109/PEE.2019.8923458.

[87] Z. Chen, S. Liu, Q. Sun, *et al.*, "A wide conversion ratio three-level dc-dc converter with loop-free self-balancing technique of flying capacitor," in *2023 IEEE International Symposium on Circuits and Systems (ISCAS)*, 2023, pp. 1–5. DOI: 10.1109/ISCAS46773.2023.10182217.

[88] J. Wei, B. Hu, and Y. Xian, "Research on three-level bi-directional dc-dc converter and its control strategy used for energy storage system of electric wheeled tramcar," in *2021 IEEE 16th Conference on Industrial Electronics and Applications (ICIEA)*, 2021, pp. 2048–2052. DOI: 10.1109/ICIEA51954.2021.9516341.

[89] P. Kala and S. Arora, "A comprehensive study of classical and hybrid multilevel inverter topologies for renewable energy applications," *Renewable and Sustainable Energy Reviews*, vol. 76, pp. 905–931, 2017, ISSN: 1364-0321. DOI: https://doi.org/10.1016/j.rser.2017.02.008. [Online]. Available: https://www.sciencedirect.com/science/article/pii/S1364032117302125.

[90] S. Mersche, M. Bayer, K. Rickert, and M. Hiller, "Analysis of balancing algorithms for quasi- two/three-level single phase operation of a flying capacitor converter," in

2022 24th European Conference on Power Electronics and Applications (EPE'22 ECCE Europe), 2022, pp. 1–10.

[91] D. Zhang, C. Chen, Y. Ou, T. Zheng, and W. Tang, "Model predictive control of three-level bidirectional dc-dc converter based on super capacitor energy storage system," in *2020 International Conference on Electrical Engineering (ICEE)*, 2020, pp. 1–5. DOI: 10.1109/ICEE49691.2020.9249868.

[92] V. Jayan, A. Ghias, and A. Merabet, "Modeling and control of three-level bidirectional flying capacitor dc- dc converter in dc microgrid," in *IECON 2019 - 45th Annual Conference of the IEEE Industrial Electronics Society*, vol. 1, 2019, pp. 4113–4118. DOI: 10.1109/IECON.2019.8926699.

[93] T. H. Shahsavar, N. V. Kurdkandi, O. Husev, *et al.*, "A new flying capacitor-based buck-boost converter for dual-purpose applications," *IEEE Journal of Emerging and Selected Topics in Industrial Electronics*, vol. 4, no. 2, pp. 447–459, 2023. DOI: 10.1109/JESTIE.2023.3238322.

[94] D. H. Zhou, J. Celikovic, Y. Elasser, D. Maksimovic, and M. Chen, "Balancing limits of flying capacitor voltages in coupled inductor fcml converters," in *2022 IEEE 23rd Workshop on Control and Modeling for Power Electronics (COMPEL)*, 2022, pp. 1–8. DOI: 10.1109/COMPEL53829.2022.9830009.

[95] Z. Chen, S. Liu, Y. Chen, X. Fan, and Y. Ma, "A current-injection-based flying capacitor balancing circuit for three-level dc-dc converter," in *2022 IEEE International Symposium on Circuits and Systems (ISCAS)*, 2022, pp. 2630–2634. DOI: 10.1109/ISCAS48785.2022.9938016.

[96] H. Ohnishi and M. Hagiwara, "Experimental verification of a bidirectional chopper for battery energy storage systems capable of reduction in size and weight of an inductor," in *2017 IEEE Energy Conversion Congress and Exposition (ECCE)*, 2017, pp. 197–204. DOI: 10.1109/ECCE.2017.8095781.

[97] H. J. Ahmad, H. Ohnishi, and M. Hagiwara, "Start-up and transient operation of a bidirectional chopper with an auxiliary converter," in *2018 International Power Electronics Conference (IPEC-Niigata 2018 -ECCE Asia)*, 2018, pp. 3273–3279. DOI: 10.23919/IPEC.2018.8507570.

[98] M. Hagiwara and H. J. Ahmad, "High switching frequency operation of bidirectional chopper with auxiliary converter for dc electric railways," in *2021 IEEE International Future Energy Electronics Conference (IFEEC)*, 2021, pp. 1–6. DOI: 10.1109/IFEEC53238.2021.9661786.

[99] H. J. Ahmad and M. Hagiwara, "Interleaved bidirectional chopper with auxiliary converters for battery energy storage systems," in *2020 IEEE Applied Power Electronics Conference and Exposition (APEC)*, 2020, pp. 2090–2097. DOI: 10.1109/APEC39645.2020.9124220.

[100] H. J. Ahmad and M. Hagiwara, "Modified phase-shifted pwm for interleaved bidirectional chopper with auxiliary converters," in *2021 IEEE 12th Energy Conversion Congress & Exposition - Asia (ECCE-Asia)*, 2021, pp. 755–761. DOI: 10.1109/ECCE-Asia49820.2021.9479010.

[101] H. J. Ahmad and M. Hagiwara, "A compact high-power noninverting bidirectional buck-boost chopper for onboard battery energy storage systems," *IEEE Transactions on Power Electronics*, vol. 37, no. 2, pp. 1722–1735, 2022. DOI: 10.1109/TPEL.2021.3106240.

[102] H. J. Ahmad and M. Hagiwara, "Interleaved bidirectional chopper with auxiliary converters for dc electric railways," *IEEE Transactions on Power Electronics*, vol. 36, no. 5, pp. 5336–5347, 2021. DOI: 10.1109/TPEL.2020.3031668.

[103] N. Hassanpour, A. Chub, A. Blinov, and D. Vinnikov, "Comparison of full power and partial power buck-boost dc-dc converters for residential battery energy storage applications," in *2022 IEEE 16th International Conference on Compatibility, Power Electronics, and Power Engineering (CPE-POWERENG)*, 2022, pp. 1–6. DOI: 10.1109/CPE-POWERENG54966.2022.9880862.

[104] R. Barrera-Cardenas, T. Isobe, and M. Molinas, "Optimal design of air-core inductor for medium/high power dc-dc converters," in *2016 IEEE 17th Workshop on Control and Modeling for Power Electronics (COMPEL)*, 2016, pp. 1–8. DOI: 10.1109/COMPEL.2016.7556774.

[105] C. Rindfleisch and B. Wicht, "Efficiency impact of air-cored inductors in multi-mhz power converters," in *2016 18th European Conference on Power Electronics*

and Applications (EPE'16 ECCE Europe), 2016, pp. 1–8. DOI: 10.1109/EPE.2016.7695433.

[106] R. T. Naayagi and A. J. Forsyth, "Design of high frequency air-core inductor for dab converter," in *2012 IEEE International Conference on Power Electronics, Drives and Energy Systems (PEDES)*, 2012, pp. 1–4. DOI: 10.1109/PEDES.2012.6484367.

[107] S. R. Meher, D. Gautam, and R. Singh, "Wireless power transfer using ef2 inverter with fixed coil capacitor and air core inductor," in *2020 IEEE Applied Power Electronics Conference and Exposition (APEC)*, 2020, pp. 3588–3593. DOI: 10.1109/APEC39645.2020.9124566.

[108] C. Shetty, Y. Kandeel, L. Ye, *et al.*, "Analytical expressions for inductances of 3-d air-core inductors for integrated power supply," *IEEE Journal of Emerging and Selected Topics in Power Electronics*, vol. 10, no. 2, pp. 1363–1383, 2022. DOI: 10.1109/JESTPE.2021.3077203.

[109] G. Abad, *Power Electronics and Electric Drives for Traction Applications*. John Wiley & Sons, Incorporated, 2016, ISBN: 9781118954454. [Online]. Available: https://books.google.co.jp/books?id=_loanQAACAAJ.

[110] G. M. Buiatti, J. A. MartÍn-Ramos, A. M. R. Amaral, P. Dworakowski, and A. J. M. Cardoso, "Condition monitoring of metallized polypropylene film capacitors in railway power trains," *IEEE Transactions on Instrumentation and Measurement*, vol. 58, no. 10, pp. 3796–3805, 2009. DOI: 10.1109/TIM.2009.2019719.

[111] B. Yao, X. Ge, D. Xie, *et al.*, "Electrothermal stress analysis and lifetime evaluation of dc-link capacitor banks in the railway traction drive system," *IEEE Journal of Emerging and Selected Topics in Power Electronics*, vol. 9, no. 4, pp. 4269–4284, 2021. DOI: 10.1109/JESTPE.2020.3000130.

[112] X. Wu, K. Li, R. Tian, *et al.*, "A capacitance estimation method for dc-link capacitors in railways based on precharging model and low sampling frequency," *IEEE Transactions on Power Electronics*, vol. 39, no. 1, pp. 1527–1537, 2024. DOI: 10.1109/TPEL.2023.3322699.

[113] H. Jang, H. Kim, D.-W. Nam, W.-H. Kim, J. Lee, and C. Jin, "Investigation and analysis of novel skewing in a 140 kw traction motor of railway cars that accommodate limited inverter switching frequency and totally enclosed cooling system,"

IEEE Access, vol. 9, pp. 121 405–121 413, 2021. DOI: 10.1109/ACCESS.2021.3109267.

[114] S. Nategh, D. Lindberg, R. Brammer, A. Boglietti, and O. Aglen, "Review and trends in traction motor design: Electromagnetic and cooling system layouts," in *2018 XIII International Conference on Electrical Machines (ICEM)*, 2018, pp. 2600–2606. DOI: 10.1109/ICELMACH.2018.8506817.

[115] H. Hayashiya and K. Kondo, "Recent trends in power electronics applications as solutions in electric railways," *IEEJ Transactions on Electrical and Electronic Engineering*, vol. 15, no. 5, pp. 632–645, 2020. DOI: https://doi.org/10.1002/tee.23121. eprint: https://onlinelibrary.wiley.com/doi/pdf/10.1002/tee.23121. [Online]. Available: https://onlinelibrary.wiley.com/doi/abs/10.1002/tee.23121.

[116] A. Hillers, M. Stojadinovic, and J. Biela, "Systematic comparison of modular multilevel converter topologies for battery energy storage systems based on split batteries," in *2015 17th European Conference on Power Electronics and Applications (EPE'15 ECCE-Europe)*, 2015, pp. 1–9. DOI: 10.1109/EPE.2015.7309385.

[117] U. Drofenik and J. W. Kolar, "Analyzing the theoretical limits of forced air-cooling by employing advanced composite materials with thermal conductivities $>$ 400w/mk," in *4th International Conference on Integrated Power Systems*, 2006, pp. 1–6.

[118] J.-i. Itoh, T. Araki, and K. Orikawa, "Experimental verification of an emc filter used for pwm inverter with wide band-gap devices," in *2014 International Power Electronics Conference (IPEC-Hiroshima 2014 - ECCE ASIA)*, 2014, pp. 1925–1932. DOI: 10.1109/IPEC.2014.6869848.

[119] 2013. [Online]. Available: https://felib.fujielectric.co.jp/download/b9ca89b2-8198-4480-9ebd-b8f5dd0a17ed/?lang=ja.

[120] 2020. [Online]. Available: https://www.mitsubishielectric.com/semiconductors/content/product/powermodule/igbt/t_series/cm1000dx-24t_e.pdf.

[121] 2024. [Online]. Available: https://www.electronicon.com/fileadmin/inhalte/PDF-Dateien/Kataloge_und_Broschueren/200.003-020030_PK16.pdf.

[122] U. DROFENIK and J. W. KOLAR, "Thermal power density barriers of converter systems," in *5th International Conference on Integrated Power Electronics Systems*, 2008, pp. 1–5.

[123] H. Hayashiya and K. Kondo, "Recent trends in power electronics applications as solutions in electric railways," *IEEJ Transactions on Electrical and Electronic Engineering*, vol. 15, no. 5, pp. 632–645, 2020. DOI: https://doi.org/10.1002/tee.23121. eprint: https://onlinelibrary.wiley.com/doi/pdf/10.1002/tee.23121. [Online]. Available: https://onlinelibrary.wiley.com/doi/abs/10.1002/tee.23121.

[124] C. F. Strowitzki, "Parametric measurements of switching losses of insulated gate bipolar transistor in pulsed power applications," *IEEE Transactions on Plasma Science*, vol. 41, no. 10, pp. 2614–2618, 2013. DOI: 10.1109/TPS.2013.2251678.

[125] Y. Shen, J. Jiang, Y. Xiong, Y. Deng, X. He, and Z. Zeng, "Parasitic inductance effects on the switching loss measurement of power semiconductor devices," in *2006 IEEE International Symposium on Industrial Electronics*, vol. 2, 2006, pp. 847–852. DOI: 10.1109/ISIE.2006.295745.

[126] T.-H. Ho and Y.-M. Chen, "On the switching loss of the sic mosfet parasitic capacitors," in *2023 IEEE Workshop on Wide Bandgap Power Devices and Applications in Asia (WiPDA Asia)*, 2023, pp. 1–4. DOI: 10.1109/WiPDAAsia58218.2023.10261918.

[127] T. Zhao, J. Wang, A. Q. Huang, and A. Agarwal, "Comparisons of sic mosfet and si igbt based motor drive systems," in *2007 IEEE Industry Applications Annual Meeting*, 2007, pp. 331–335. DOI: 10.1109/07IAS.2007.51.

[128] M. Alam, K. Kumar, and V. Dutta, "Comparative efficiency analysis for silicon, silicon carbide mosfets and igbt device for dc-dc boost converter," *SN Applied Sciences*, vol. 1, no. 1700, 2019. DOI: 10.1007/s42452-019-1778-4.

[129] J. Qi, X. Yang, X. Li, *et al.*, "Temperature dependence of dynamic performance characterization of 1.2-kv sic power mosfets compared with si igbts for wide temperature applications," *IEEE Transactions on Power Electronics*, vol. 34, no. 9, pp. 9105–9117, 2019. DOI: 10.1109/TPEL.2018.2884966.

[130] A. Kahwa, H. Obara, and Y. Fujimoto, "Estimation and analysis of power loss in a reduced switches count h-bridge multilevel inverter," in *2019 IEEE International Conference on Mechatronics (ICM)*, vol. 1, 2019, pp. 25–30. DOI: 10.1109/ICMECH.2019.8722859.

[131] T. Ibuchi and T. Funaki, "Validation of the air-core inductor copper loss model for high-frequency power conversion applications," in *2013 International Symposium on Electromagnetic Compatibility*, 2013, pp. 561–566.